IMPROVED TRANSIENT NETWORK MODEL FOR WICKED HEAT PIPES

IMPROVED TRANSIENT NETWORK MODEL FOR WICKED HEAT PIPES

By

SAMEH MOSSAAD ISKANDER SAAD

A Thesis.

Submitted to the School of Graduate Studies

in Partial Fulfillment of the requirements

for the Degree of

Master of Applied Science

McMaster University

Hamilton, Ontario, Canada

MASTER OF APPLIED SCIENCE (2006)   MCMASTER UNIVERSITY

(Mechanical Engineering)   Hamilton, Ontario, Canada

TITLE: Improved Transient Network Model for Wicked Heat Pipes

AUTHOR: Sameh Mossaad Iskander Saad
            B.Sc. (Mechanical Power Engineering), 2002
            Ain Shams University, Cairo, Egypt.

SUPERVISORS: Dr. Chan Y. Ching
                  Dr. Daniel Ewing

NUMBER OF PAGES: 133 pages (i-xvi, 1-117)

ABSTRACT

An existing transient network model for wicked heat pipes was extended to incorporate the effects of axial heat transfer along the wall and wick, heat transfer in the surrounding media, and non-condensable gases in the vapour region. The thermal resistance of the different components was broken down into a larger number of smaller resistances in both axial and radial directions to account for the axial conduction and to handle non-uniform boundary conditions. Two sets of experiments were performed on copper-water wicked heat pipes to evaluate the effect of non-condensable gases, axial conduction, surrounding media and non-uniform boundary conditions. In the first set of experiments, the heat pipes were electrically heated at one end and cooled on the other end using a water jacket. This set of experiments was used to investigate the effect of non-condensable gases, axial conduction and surrounding media on the steady state and transient performance. The effect of the surrounding media was investigated by heating the heat pipe through two different sized aluminum blocks mounted around the heat pipe evaporator section. In the second set of experiments, the effect of using a finned condenser on the steady state performance of the heat pipes were tested in a wind tunnel. The condenser section of the heat pipes in this case was mounted in the test section of the wind tunnel and cooled at different air velocities. Three fin densities were tested along with a heat pipe with no fins. The model predictions of the steady and transient response of the vapour and wall temperature of the heat pipes were in good agreement with the experimental results.

The presence of non-condensable gases inside the heat pipe increased the overall thermal resistance of the heat pipe. While the non-condensable gases did not notably affect the transient response during the heat-up phase, it significantly slows down the cool-down phase. The axial conduction through the pipe wall and the wick structure decreases the overall thermal resistance of the heat pipe. The axial conduction did not have a great influence on the time response during the heat-up phase, but was very important in the cool-down phase, especially with the presence of non-condensable

gases. The wick structure was found to be the most dominant component in the transient performance of the heat pipe. The evaporator block was the dominant capacitance in the overall conjugate system, and significantly affects the transient response. The experimental results from the finned condenser study showed that the internal resistance increased slightly with the fin density. There was some non-uniformity in the condenser surface temperature at the locations of the fins. However, this non-uniformity did not propagate to other parts of the heat pipe.

†

"I can do all things through Christ who strengthens me."

(Philippians 4:13)

To my Lord, God and Savior JESUS CHRIST.
To my Father, Mother, Brother and Sister.
To my beloved homeland, Egypt.

ACKNOWLEDGMENTS

NOMENCLATURE

A Cross-sectional area, $[m^2]$.

C Compressibility coefficient, $[-]$.

F_v Vapour frictional coefficient, $[s/m^4]$.

GCI Grid convergence index, $[-]$.

L Length, $[m]$.

Ma Mach number, $[-]$.

N Screen mesh number, $[-]$.

Nu Nusselt number, $[-]$.

P Pressure, $[N/m^2]$.

Pr Prandtl number, $[-]$.

Q Total heat transfer rate, $[W]$.

R Thermal resistance, $[K/W]$.

Re Reynolds number, $[-]$.

S Lateral surface area, $[m^2]$.

T Temperature, $[K]$.

c_p Specific heat capacity, $[J/kg.K]$.

d Screen mesh wire diameter, $[m]$.

d_h Hydraulic diameter, $[m]$.

f_v Frictional drag coefficient, $[-]$.

h Heat transfer coefficient, $[W/m^2.K]$.

h_{fg} Latent heat of vaporization, $[J/kg]$.

k Thermal conductivity, $[W/m.K]$.

$m^{\cdot}$ Mass flow rate, $[kg/s]$.

q Specific heat transfer rate, $[W/m^2]$.

r Radius, $[m]$.

s Fin spacing, $[m]$.

t Thickness, $[m]$.

v Velocity, $[m/s]$.

w Screen mesh wire separation, $[m]$.

Greek letters

α Empirical constant for wick effective thermal conductivity, $[-]$.

ϵ Screen mesh porosity, $[-]$.

η_f Fin efficiency, $[-]$.

μ Dynamic viscosity, $[Pa.s]$.

ρ Density, $[kg/m^3]$.

Subscripts

a Adiabatic.

amb Ambient.

c Condenser.

e Evaporator.

eff Effective.

f Fluid.

g Gas.

i Inside.

o Outside.

s Solid.

sat Saturated.

v Vapour.

vis Viscous.

w Wall.

CONTENTS

LIST OF TABLES

LIST OF FIGURES

CHAPTER 1
INTRODUCTION

In recent years, it has become increasingly important to develop methods for the efficient transport of thermal energy due to increased thermal constraints in many applications. Moreover, the advent of the space age stimulated research for heat transfer devices which are passive and light weight with relatively long life expectancies. Such a device, although not for space application, was first proposed by Gaugler (1944) of the General Motors Corporation. However, the technology of that period presented no clear need for such a device and it lay dormant for two decades. The idea was resurrected in connection with the space program, as a suggestion by Trefethen (1962). However, it was Grover et al. (1964) of the Los Alamos Scientific Laboratory that provided the impetus for this technology. Grover built prototypes and coined the term *"heat pipe"* for these devices. Grover went on to state, *"Within certain limitations on the manner of use, a heat pipe may be regarded as a synergistic engineering structure which is equivalent to a material having a thermal conductivity greatly exceeding that of any known metal"*. Heat pipes have since been used extensively for thermal management in space applications. More recently, heat pipes have been adapted for thermal management in many other applications including machining systems, casting and moulding applications, and electronic systems.

A heat pipe is essentially a closed container, usually in the form of a cylinder, containing a working fluid which transfers thermal energy from the hot end (evaporator) to the cold end (condenser) by evaporation and condensation of the working fluid. The condensate is returned back to the evaporator typically by capillary action using a wick attached to the inner wall. The phase change of the working fluid allows a significant amount of heat to be transported for a relatively small temperature difference between the evaporator and condenser. Thus, heat pipes are capable of providing the low thermal resistances typical of two-phase flow heat transfer devices

1

without an external pump.

Heat pipes are currently being increasingly used in a number of engineering applications. For example, increased power requirements in modern electronic systems and subsequent increases in heat dissipation densities have resulted in greater demands on cooling systems. Heat pipes are currently used to transport heat away from components such as the Central Processing Units (CPU) and Graphics Processing Units (GPU) to heat sinks where thermal energy may be dissipated into the environment. Heat pipes are also used in solar thermal water heating applications in combination with evacuated tube solar collector arrays. In these applications, distilled water is commonly used as the heat transfer fluid inside a sealed length of copper tubing that is located within an evacuated glass tube and orientated towards the Sun. In solar thermal water heating applications, an evacuated tube collector can deliver up to 40% more efficiency compared to more traditional "flat plate" solar water heaters. Other applications of heat pipes include cooling of engine oils, cooling of drills and semi-automatic welding equipment, cooling of soldering iron bits, and cooling of gas turbine blades. Heat pipes are also currently used in thermal control of thermoelectric generators, thermal control of electric storage heaters, and isothermalisation of bio-reactors. Heat pipes have also been used in domestic warm air heaters and in the thermal control in electric batteries.

One particular area of application that is of interest in this study is the die casting and injection molding industry. In these processes, metal alloys or plastics are introduced in molten form into a die or mold and rapidly cooled to produce a component. The production rate of small plastic components can be several per second, while alloy castings such as covers for car gearboxes may be produced at upwards of one per minute. The controlled removal of heat during the solidification process is critical for product quality. Nearly all dies are water-cooled and there are difficulties in routing water-cooling channels to inaccessible parts of the die. A more important aspect of die cooling is the need to minimize thermal shock, thus ensuring a reasonable life for the components. In some processes it may be necessary or desirable to heat parts of the die to ensure a continuous flow of the molten material to the more

inaccessible regions remote to the injection point. A heat pipe in its simple tubular form has properties that make it attractive in these two areas of application in dies and molds. Firstly, the heat pipe may be used to even out temperature gradients in the die by inserting it into the main body of the die, without connecting it to the water-cooling circuits. Secondly, and probably the most important application, assisting the heat transfer between the die face and the water-cooling path in areas where hot spots occur. In these applications, the transient response of the heat pipe and the conjugate heat transfer in the surrounding medium is important to properly design the overall thermal management system.

The objective of this investigation was to expand an existing transient network model for wicked heat pipes proposed by Zuo and Faghri (1998) to incorporate the effects of axial heat transfer in the wall and wick, heat transfer in the surrounding media, and non-condensable gases in the vapour region. The improved model was developed to predict the steady and transient heat pipe performance for different unsteady and non-uniform boundary conditions. Experiments were performed to validate the model results and to examine the change in the heat pipe transient performance with the wick thickness and the surrounding media. Finally, the effect of fins on the condenser end of the heat pipe was investigated both experimentally and numerically.

This thesis contains six chapters including this introductory chapter. The different types of heat pipes are reviewed in chapter two along with a review of previous research on the modeling and testing of wicked heat pipes. Chapter three presents the development of the transient network model for wicked heat pipes. Chapter four presents the experimental facilities used and details the procedure used to test the heat pipes. The results and discussion are presented in chapter five and the conclusions and recommendations generated by this investigation are presented in chapter six.

CHAPTER 2
LITERATURE REVIEW

In this chapter, different types of heat pipes are introduced with a focus on the operation of wicked heat pipes and a summary of wick structures, working fluids and operating temperature ranges. A summary of the previous models developed for the steady and transient performance of heat pipes is presented as well as a summary of the models for non-condensable gases present in a heat pipe. The chapter is concluded by a survey of previous efforts to study heat pipes with a finned condenser.

2.1 Heat Pipes

Heat pipes are passive two-phase heat transport devices that transport heat by evaporation and condensation of a working fluid within a sealed container. Heat pipes have been built with diameters varying from the millimeter range up to almost one meter and with length-to-diameter ratios varying from about 0.1 up to 450. The working fluid is evaporated at the hot end (evaporator) and condensed at the colder end (condenser). Typically, heat pipes when in operation also have an adiabatic (insulated) section separating the evaporator and the condenser sections. The liquid condensate is driven back to the evaporator in a number of ways, most commonly by capillary forces in a porous wick along the wall. Heat pipes have also been developed that use gravitational forces, rotationally-induced forces, and electrostatic forces.

Heat pipes have been designed in a variety of sizes and configurations, the most common being the wicked heat pipe where the condensate is returned back to the evaporator by capillary action using a wick along the inner wall as shown in figure 2.1(a). Another typical heat pipe configuration is the flat-plate heat pipe, which is capillary-driven with small aspect ratios as illustrated in figure 2.1(b). Additional wick material can be placed between the evaporator and condenser wicks to improve

(a) *Capillary-driven wicked heat pipe*

(b) *Flat-plate heat pipe*

(c) *Two-phase closed thermosyphon*

(d) *Rotating heat pipe*
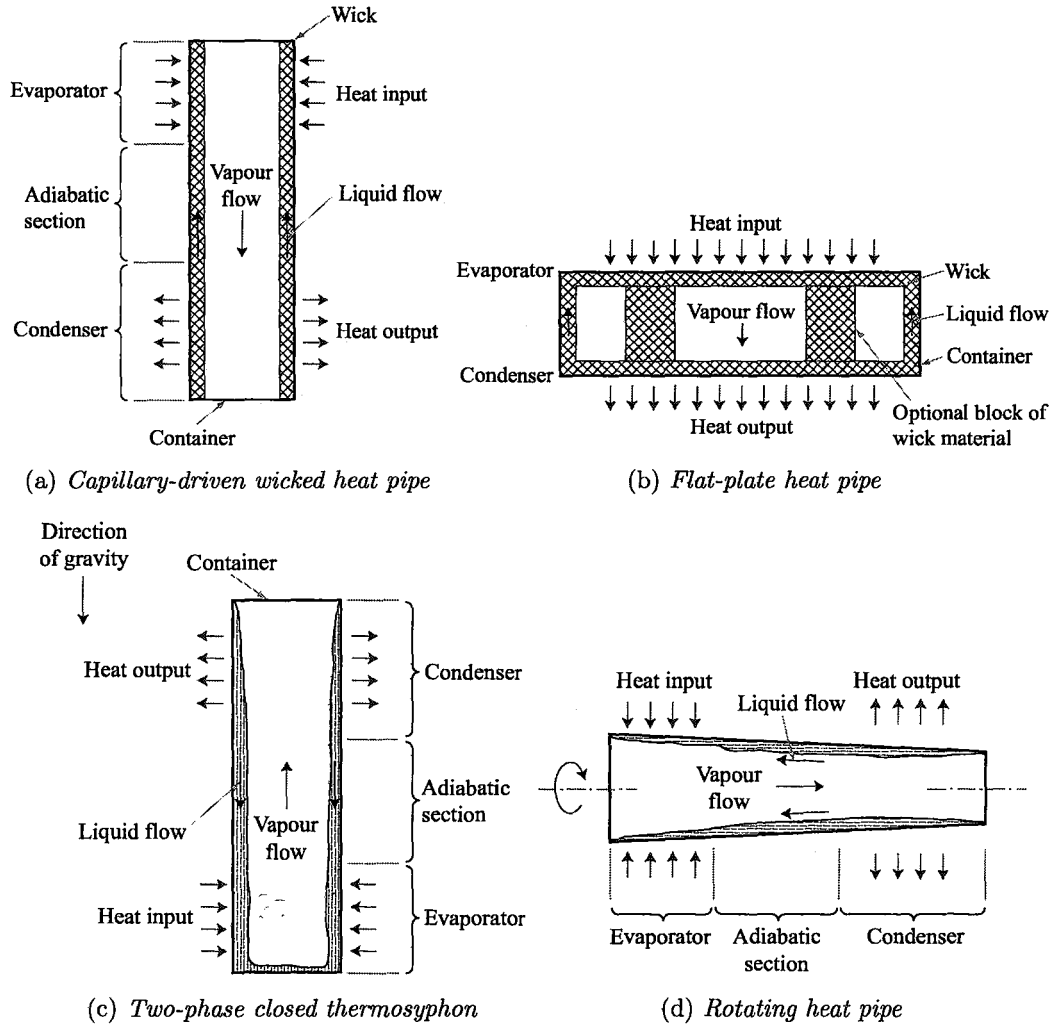
Figure 2.1: Different types of heat pipes.

liquid return to the evaporator. Alternatively, if the condenser is above the evaporator, the wick need only cover the evaporator to provide efficient distribution of liquid; the liquid condenses on the upper plate and drips back to the evaporator. Provided that the condenser is higher than the evaporator, gravitational forces alone can return the liquid to the evaporator. In this case the wick can be dispensed with and the device, illustrated in figure 2.1(c), is called a two-phase closed thermosyphon. Another type of heat pipe is the rotating heat pipe illustrated in figure 2.1(d). In this device the liquid is driven back to the evaporator along the tapered inner wall of the container by the centrifugal forces and no wick is needed.

The conventional wicked heat pipe, illustrated in figure 2.2, consists of a sealed tube lined with a wick structure along its inner wall. The container is evacuated and typically filled with just enough liquid to fully saturate the wick. Operating on a closed two-phase cycle, the working fluid remains at saturation conditions as long as the operating temperature is between the freezing point and the critical state. Heat added at the hot region evaporates the working fluid, and the high temperature and corresponding high pressure in this region results in a flow of the vapour to the cooler end where the vapour is condensed, giving up its latent heat of vaporization. The evaporating meniscus of the liquid-vapour interface in the evaporator (figure 2.2) results in a capillary pressure in the wick structure that draws the liquid back to the evaporator to complete the thermodynamic cycle (Chi, 1976).

Each heat pipe application has a particular operational temperature range. Therefore, a proper working fluid should be specified that is suitable for the intended temperature range. The useful range extends from the point where the saturation pressure is greater than 0.1 atm and less than 20 atm. The working fluids can be classified into four main categories as shown in table 2.1. In order to ensure that a heat pipe has a lifetime of (typically) several years, the working fluid, the container material, any brazing material used and the material of any wick present must be compatible. Performance can be degraded and failure can occur if any of the parts are not compatible. For instance, the different parts can react chemically or set up a galvanic cell within the heat pipe. Also, the container material may be soluble in the

6
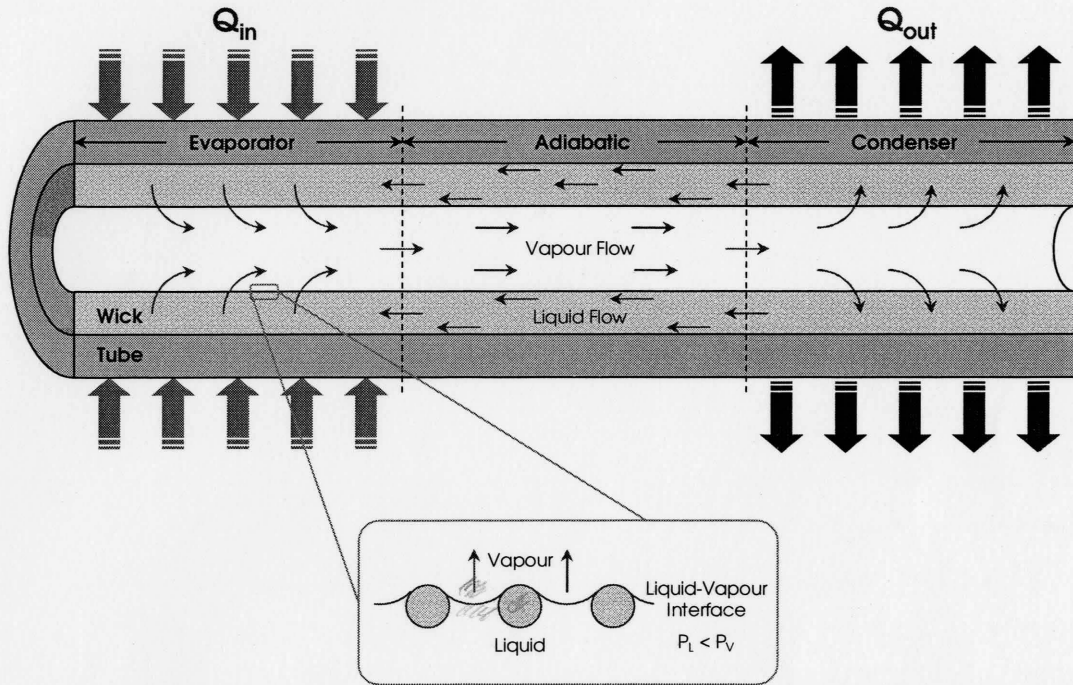
Figure 2.2: A typical wicked heat pipe operation.
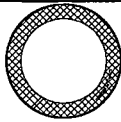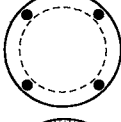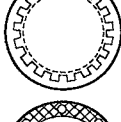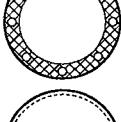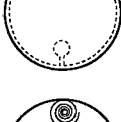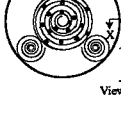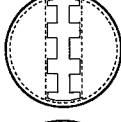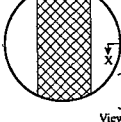
Table 2.1: Typical working fluids and temperature ranges.

Category	Temp. Range (K)	Typical Working Fluids
Cryogenic	4 - 200 K	Helium, argon, oxygen and krypton
Low Temperature	200 - 550 K	Ammonia, acetone, the Freon compounds and water
Medium Temperature	550 - 750 K	Mercury and sulphur
High Temperature	more than 750 K	Sodium, lithium, silver and sodium-potassium compound

working fluid or may catalyze the decomposition of the working fluid at the expected operating temperature.

The wick structure within the wicked heat pipe is present to return condensate to the evaporator section. While small pores are needed at the liquid-vapour interface to develop high capillary pressures, large pores are preferred within the wick to facilitate the liquid movement. Consequently, many types of wick structures have been developed to optimize the performance of the capillary heat pipe. A summary of typical wick designs and their relative performance is presented in table 2.2. There are three important properties of wicks in heat pipe design: capillary radius, effective thermal conductivity, and permeability. The capillary radius should be small if a large capillary pressure difference is required, such as in cases where a high heat transport capability is needed. A large value for the effective thermal conductivity gives a small temperature drop across the wick, which is a favorable condition in heat pipe design. The permeability is a measure of the wick resistance to axial liquid flow, and it should be large in order to have a small liquid pressure drop and higher heat transport capability. These three parameters are sometimes hard to find in one wick design, and hence there is significant ongoing research to develop optimal wick structures for different applications.

Table 2.2: Typical wick designs, *adapted from Faghri (1995)*.

Wick Type	Shape	Capillary Pumping	Thermal Conductivity	Permeability
Homogeneous: Multiple wire mesh screens, packed spherical particles, felted metal fibres, woven or felted ceramic fibres		High	Low-average	Low-average
Longitudinal Groove: Longitudinal grooves may have other than rectangular cross sections		Low	High	Average-high
Annular: Wire mesh screen spaced from wall		Low	Low	High
Composite: Two or more layers of homogeneous material, the material closest to the wall has the largest pore size		High	Low-average	Average
Screen-covered Groove: Longitudinal grooves may have other than rectangular cross sections		High	High	Average-high
Integral Artery: Homogeneous material with built-in arteries		High	High	Average-high
Pedestal Artery - Screen: Wire mesh screen formed into artery and wall lining		Low	High	High
Spiral Artery - Circumferential Groove: Spiral wire mesh screen with spacers and wire mesh scrolls for liquid transfer between artery and grooves in evaporator and condenser	View X X	High	High	Average-high
Central Artery - Screen: Central insert with screen-covered arteries and screen wall lining		High	High	High
Slab - Circumferential Groove: Slab of homogeneous material with circumferential grooves in evaporator and condenser	View X X	High	High	High

9

2.2 Modeling of Wicked Heat Pipes

A number of models have been developed that provided temperature, pressure, and velocity distributions in transient and steady-state operation of heat pipes. These include a lumped analysis, one-dimensional, two-dimensional, and three-dimensional models. While a few of these models considered both the vapour flow along with the heat transport processes in the heat pipe, other models have considered only one of them.

Faghri and Harley (1994) proposed a lumped model for the transient performance by neglecting the small temperature differences within the heat pipe. Relatively simple, geometry-independent equations giving the average temperature of the heat pipe, T, as a function of the time, t, were obtained. Since the heat pipe is assumed to be isothermal, this lumped model cannot predict the transient behaviour when the surface temperature is specified at either the evaporator or the condenser. In these cases, the changes are assumed rapid enough for the average temperature to change instantaneously to its new value. Four different cases were considered: Case A for a sudden change in heat flux with a constant specified-temperature heat sink, case B for a constant specified heat flux with a sudden change in the heat sink temperature, case C and D for a sudden change in either the evaporator or condenser

Table 2.3: Average temperatures after a sudden change in heat input or in temperature using the lumped analysis (Faghri and Harley, 1994).

Case	Equation for average temperature	Time constant
A	$T(t) = T_{\infty,c} + Q_{e2}R_c\left(1 + \dfrac{Q_{e1}}{Q_{e2}}e^{-t/\tau} - e^{-t/\tau}\right)$	$\tau = C_t R_c$
B	$T(t) = T_{\infty,c1} + Q_e R_c + (T_{\infty,c2} - T_{\infty,c1})\left(1 - e^{-t/\tau}\right)$	$\tau = C_t R_c$
C	$T(t) = \dfrac{T_{\infty,c1}R_e - T_{\infty,e1}R_c}{R_e + R_c} + \dfrac{R_c\left(T_{\infty,e2} - T_{\infty,e1}\right)}{R_e + R_c}\left(1 - e^{-t/\tau}\right)$	$\tau = \dfrac{C_t R_e R_c}{R_e + R_c}$
D	$T(t) = \dfrac{T_{\infty,c1}R_e - T_{\infty,e1}R_c}{R_e + R_c} + \dfrac{R_e\left(T_{\infty,c2} - T_{\infty,c1}\right)}{R_e + R_c}\left(1 - e^{-t/\tau}\right)$	$\tau = \dfrac{C_t R_e R_c}{R_e + R_c}$

temperatures. The governing equations for the transient response for the above cases are summarized in table 2.3. The total thermal capacity of the heat pipe, C_t, was evaluated as the sum of the heat capacities of the solid and liquid components of the device since the mass of vapour is small. The thermal resistances between the heat source and the evaporator external surface and between the condenser external surface and the heat sink, R_e and R_c, were assumed constant as

$$R_e = 1/\left(h_e S_e\right) \tag{2.1}$$

$$R_c = 1/\left(h_c S_c\right) \tag{2.2}$$

The transient, compressible one-dimensional vapour flow in a cylindrical heat pipe was analyzed by Jang et al. (1991). The numerical results were compared to previous simulations and experimental results for the steady state by Bowman and Hitchcock (1988). The experimental data for this case was obtained by simulating the vapour flow in a porous pipe with blowing and suction sections. In addition, the numerical results from this model were also compared to vapour flow measurements in a cylindrical high temperature heat pipe at steady state by Ivanovskii et al. (1982). The one dimensional compressible model predicted the experimental data well for the cylindrical heat pipe and the simulated heat pipe at steady state.

Bowman et al. (1992) presented a one-dimensional model for the vapour flow which was treated as a saturated vapour and not as an ideal gas. This model was improved by Bowman and Beran (1994), who used a more accurate closure relationship between the vapour density and vapour temperature in solving the mass conservation equation. However, this model did not include the thermal effects of the wall and the wick on the heat pipe operation. Issacci et al. (1991) used a two-dimensional, transient, compressible viscous flow model to analyze the vapour dynamics during heat pipe start-up, while Bowman and Hitchcock (1988) studied transient two-dimensional compressible air flow in a porous pipe and compared their simulation results and experimental data with fairly good agreement. However, the transient time periods determined by this study did not include the conjugate effect of the heat pipe wall

and wick.

Cao and Faghri (1990) proposed a methodology to simulate the transient two-dimensional operation of a high-temperature heat pipe, by coupling the vapour flow with heat conduction in the wall and wick. Conservation equations were solved using an effective thermal conductivity for the screen wick. The saturation temperature was obtained from the saturation pressure at the liquid-vapour interface using the Clausius-Clapeyron equation; the equation of state for an ideal gas was applied in the vapour core. It was found that it was very important to treat the entire heat pipe as a single conjugate system rather than to analyze the vapour flow alone as the the wick and wall play crucial roles in the transient response of the heat pipe. This methodology was extended by Faghri et al. (1991) to model high-temperature heat pipes with multiple heat sources and sinks.

Zuo and Faghri (1997) developed a heat pipe model with a quasi-steady, one-dimensional vapour flow and transient, two-dimensional heat conduction in the wall and wick. The vapour and wall transients had vastly different time scales where the vapour flow had a faster time constant than the pipe wall and the wick structure. The results showed little difference to a fully transient model by Tournier and El-Genk (1994). Furthermore, it was found that the vapour flow thermal resistance was considerably smaller than the other resistances, and could be neglected from the thermal network without causing significant errors. Thus, for moderate temperature copper-water heat pipes, the thermal resistance of the heat pipe is determined primarily by the thermal resistance of the wick structure.

A two-dimensional vapour, wall and wick transient model was developed by Tournier and El-Genk (1994). Liquid compressibility, energy, and momentum discontinuities at the liquid-vapour interface and the radius of curvature of the liquid meniscus at the interface were incorporated into the model, in addition to the effects of liquid pooling in the condenser. The vapour in the core was assumed to be saturated, obviating the need for the consideration of the vapour energy equation. At the liquid-vapour interface, conservation of mass was enforced along with a no-slip condition and an enthalpy jump due to evaporation/condensation. The model results were

compared to experimental data on copper-water heat pipes with a double-layered copper screen wick by El-Genk and Huang (1993). In the model verification, the measured evaporator surface temperature was used as the boundary condition and the predictions of the transient values of the vapour and wall temperatures as well as the effective power output were in reasonable agreement with the experimental data.

A general three-dimensional heat pipe model which included the pipe wall, wick and vapour flow as a conjugate heat transfer problem was developed by Schmalhofer and Faghri (1993a). The model was employed to determine the steady state operating characteristics of circumferentially-heated and block-heated heat pipes. The numerical results were in good agreement with the experimental data by Schmalhofer and Faghri (1993b). The numerical vapour velocity profiles showed the symmetric nature of the circumferentially-heated heat pipe about the centerline. In the same regions of the block-heated heat pipe, the vapour flow was found to move radially away from the heated section and the maximum velocity was near the liquid-vapour interface opposite the heater section. The vapour and wall temperatures at steady state were not significantly different for both circumferentially-heated and block-heated heat pipes, except for the wall temperatures in the region around the evaporator.

The two and three-dimensional models discussed above result in a set of non-linear partial differential equations that are solved numerically and require a considerable amount of computational time. A simpler network model to predict the performance of the heat pipe at steady-state was presented by Dunn and Reay (1978) as will be discussed in detail in the next chapter. The model was later extended for transient analysis by Zuo and Faghri (1998). In this approach, the governing equations for the transient response were simplified to a set of linear first-order ordinary differential equations making them quicker to solve. The results from this model were in good agreement with the more detailed two dimensional numerical model presented by Cao and Faghri (1990) with a computational time that was approximately 5% of that for the two-dimensional numerical model.

2.3 Non-Condensable Gases

Non-condensable gases have been introduced in the vapour core of heat pipes to control their performance. However, in many cases non-condensable gases are generated inside the heat pipe, which can significantly deteriorate the heat pipe performance. Non-condensable gases within the heat pipe can be produced by chemical reaction between the working fluid and the heat pipe wick or wall, by breakdown of the working fluid or by outgassing from the liquid or the solid. Under normal operating conditions, the non-condensable gases tend to accumulate at the closed end of the condenser as shown in figure 2.3, decreasing the thermal conductance. A small quantity of non-condensable gas is often acceptable if the vapour pressure of the working fluid is high enough at the operating temperature so that the gases occupy only a relatively small region at the closed end of the condenser.

There has been a considerable amount of research on the effect of non-condensable gases on the performance of heat pipes. Marcus and Fleischman (1970) derived a steady state expression for the location of the vapour-gas interface based entirely on the partial pressures of the vapour and gas by assuming a sharp flat-front interface between the gas and the vapour. This model neglects any mass diffusion and assumes steady-state conditions, constant properties, and no axial heat conduction through the wick or pipe wall. The typical vapour temperature variation during start-up using this model is shown in figure 2.4. As the temperature increases, the vapour pressure compresses the non-condensable gases, increasing the active portion of the condenser.

Sun and Tien (1975) included a simple wall conduction model while still neglecting the mass diffusion between the vapour and the non-condensable gases. Their predictions agreed well with steady-state experimental results. Edwards and Marcus (1972) as well as Shukla (1981) included the effect of axial heat conduction through the walls as well as the diffusion between the working fluid and gas. The diffusion at the vapour-gas interface in the condenser section was modelled using Fick's first law of diffusion, assuming a quasi-steady process at constant temperature and pressure. Although the vapour gas interface in this case is not as sharp as the flat-front model, they found that the axial wall heat conduction was of much greater importance
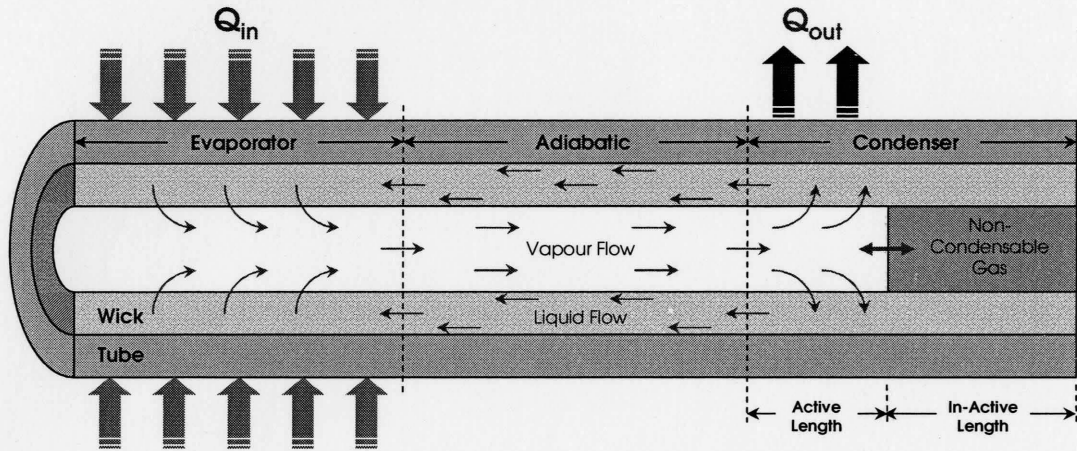
Figure 2.3: A typical wicked heat pipe operation including the effect of non-condensable gases.
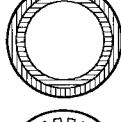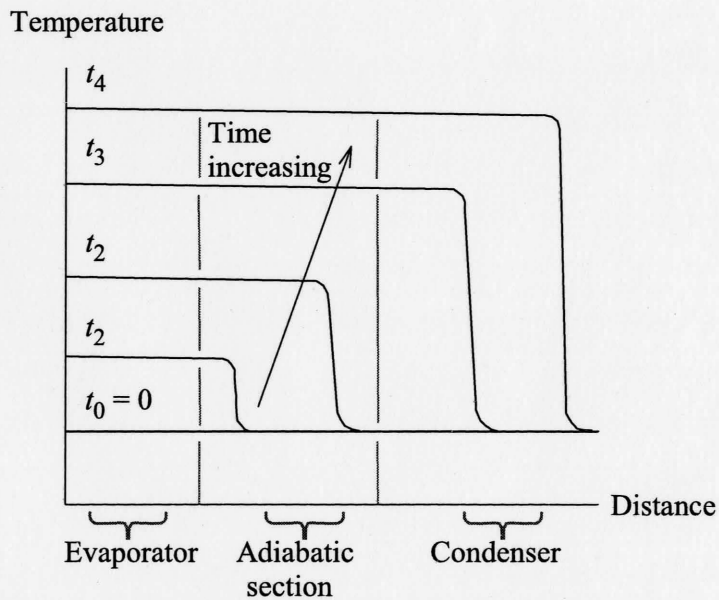

Figure 2.4: Heat pipe start up with non-condensable gas present, axial vapour temperature profile at various times, *adapted from Chi (1976)*.

than axial mass diffusion in the vapour in predicting the position of the vapour-gas interface.

Rice and Azad (1976) and Kimura et al. (1981) developed a transient model for the condenser section only that used a lumped approach to satisfy energy conservation requirements, and thus solved the temperature profiles through a fin-type relationship with a length that depended on the location of the vapour-gas interface and with an evaporative heat source. Bobco (1987) developed an analytical solution for a variable conductance heat pipe, where the heat pipe was modeled in terms of the linear one-dimensional fin equation and a closed-form solution for the temperature distribution was found in terms of the location of the flat-front of the non-condensable gases. The model was based on two simplifying assumptions; the internal convection process associated with condensation is replaced by a specific local heat flux, and the distribution of non-condensable gases throughout the length of the heat pipe was calculated in terms of mean temperatures in the different regions. The main disadvantage was that the analytical model postulates the use of two parameters that should be determined empirically; the location at which the condensation starts in the adiabatic section, and a condensation heat flux distribution parameter.

Based on the flat-front assumption, a transient lumped gas-loaded heat pipe model was developed by Faghri and Harley (1994). This model lumps the overall total thermal conductances of the evaporator, adiabatic and active condenser sections, and determines the transient response of the lumped system. The quasi-steady position of the vapour-gas interface was estimated based on the predicted lumped transient temperature of the active condenser section. The results from this model was in good agreement with the experimental data of a high-temperature gas-loaded sodium heat pipe studied by Ponnappan (1989). Ponnappan and Chang (1994) and Chung and Edwards (1996) experimentally studied the start-up performance of a high-temperature gas-loaded liquid metal heat pipe using argon gas. The motion of the gas front during the transient period was found to have a significant effect on the external axial temperature profile, and it was suggested that the influence of this varying profile on axial conduction should be included in heat pipe transient models.

2.4 Finned Condenser Heat Pipes

In practical applications, the condenser heat transfer surface area and the heat pipe operating temperature are often subject to many design constraints, such as the operating environment and the maximum allowable temperature of the heat pipe. As a result, the heat transport capacity of a heat pipe may be limited by the heat dissipation capacity of the condenser (Faghri and Buchko, 1990). When the heat transfer coefficient is low, such as the case when a heat pipe dissipates heat to the ambient by natural convection, the heat transfer capacity of the heat pipe can be limited by the condenser heat transfer limit. Faghri et al. (1987) showed that a much better performance could be obtained by having fins along the condenser section of a copper-water heat pipe compared to a conventional cooling jacket.

Finned heat pipes have found a wide range of applications, especially in the thermal control of electronic equipment and devices because of their high effective conductivity. Using the heat-pipe heat sinks, heat can be removed from many components such as power transistors or individual chips, which are often mounted on the evaporator portion of the pipe and attached mechanically. A series of fins attached to the condenser end of the heat pipe usually provides the mechanism for heat rejection to a coolant, either through free or forced convection (Eldridge and Petersen, 1983). Polasek et al. (1988) presented a finned heat pipe design for cooling of high power semi-conductor devices. The heat pipes were constructed of copper with a sintered-powder wick and equipped with rectangular fins. They compared the external thermal resistances for a single and double finned condenser heat pipe configurations, where the heat was conveyed through a metal block perpendicular to the longitudinal axis of the evaporator section of the heat pipes. The fins on the condenser section reduced the overall thermal resistance between the metal block surface and the ambient.

Heat pipes with a flat-plate evaporator end and square fins stacked around the condenser end were studied by Wang et al. (1994). Several wick structures, working fluids and orientations were examined. A heat sink consisting of multiple heat pipe supports for a parallel plate array was also studied by North and Avedisian (1993) to characterize the performance of such heat sinks. In another study by Howard and

Peterson (1995), heat transfer from a plate fin-array using multiple heat pipe supports was compared to an unfinned array of the same number of heat pipes attached to a base plate. Significant enhancements in heat transfer and reduced overall thermal resistance were realized for the finned heat pipes array compared to the unfinned sink.

A study comparing the heat transfer from a fin structure on a solid rod support to that on a heat pipe was reported by Zhao and Avedisian (1997). The heat transfer from the array of parallel plate fins in forced air flow was significantly increased by using the heat pipe. The heat pipe has a much lower resistance than the solid rod and consequently the finned heat pipe configuration would have a lower resistance. The effect of the length of the heat pipe or the solid rod on the heat transfer rate was also examined. The heat transport rate was proportional to the heat pipe length, while it was nearly independent of the length for the solid copper rod. This result is due to the fact that the end temperature of the solid copper support rod was already close to the ambient temperature for the shortest solid rod examined and therefore further increase in the rod length would not enhance the heat transfer. However, for the heat pipe case, the end temperature was much higher than the ambient temperature as a reflection of its nearly isothermal operation, and consequently any increase in the length would greatly increase the heat transfer rate.

CHAPTER 3
TRANSIENT WICKED HEAT PIPE MODEL

In this chapter the transient network model proposed by Zuo and Faghri (1998) is expanded to incorporate the effects of axial heat transfer along the wall and wick, heat transfer in the surrounding media, and non-condensable gases in the vapour region. The thermal resistance of the different components was broken down into a larger number of smaller resistances in both axial and radial directions to account for the axial conduction and to handle non-uniform boundary conditions. The model details are presented first including the modeling of the non-condensable gases followed by the methodology to estimate the wick structure properties. The chapter is concluded by a discussion of the spatial and temporal convergence of the numerical scheme.

3.1 Network Model for Wicked Heat Pipes

Most steady-state models used to predict the heat transport of a wicked heat pipe use a thermal resistance network, where each component of the heat pipe is modeled by an associated thermal resistance as illustrated in figure 3.1 (e.g. Asselman and Green, 1973; Dunn and Reay, 1978; Peterson, 1994; Faghri, 1995). A summary of the definitions and formula for the different resistances is presented in table 3.1. Here, h is the external heat transfer coefficient, S is the surface area, r_i and r_o are the inside and outside radius of the container wall, r_v is the radius of the vapour core, k_w is the thermal conductivity of the wall, k_i is the effective thermal conductivity of the wick structure, L_e, L_c and L_a are the lengths of the evaporator, condenser and adiabatic sections, T_v and P_v are the nominal temperature and pressure of the vapour, h_{fg} is the latent heat of vaporization, ρ_v is the density of the vapour, Q is the heat flux, and $(P_{v,e} - P_{v,c})$ is the vapour pressure drop from evaporator to condenser.
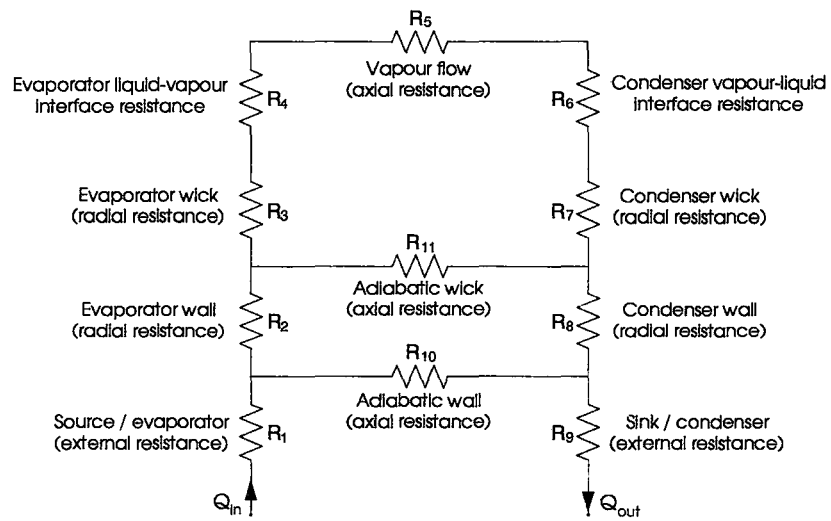
Figure 3.1: Equivalent thermal resistance network for a wicked heat pipe.

Table 3.1: Summary of thermal resistance definitions and corresponding formula.

Resistance	Definition	Formula
R_1	the thermal resistance between the heat source and the evaporator external surface	$R_1 = \dfrac{1}{h_e S_e}$
R_2	the thermal resistance across the thickness of the container wall in the evaporator	$R_2 = \dfrac{\ln(r_o/r_i)}{2\pi L_e k_w}$
R_3	the thermal resistance across the wick thickness in the evaporator	$R_3 = \dfrac{\ln(r_i/r_v)}{2\pi L_e k_i}$
R_4	the thermal resistance that occur at the vapour-liquid interfaces in the evaporator	$R_4 = \dfrac{R_v T_v^2 \sqrt{2\pi R_v T_v}}{P_v(2\pi r_v L_e)(h_{fg})^2}$
R_5	the effective thermal resistance of the vapour	$R_5 = \dfrac{T_v(P_{v,e} - P_{v,c})}{\rho_v h_{fg} Q}$
R_6	the thermal resistance that occur at the vapour-liquid interfaces in the condenser	$R_6 = \dfrac{R_v T_v^2 \sqrt{2\pi R_v T_v}}{P_v(2\pi r_v L_c)(h_{fg})^2}$
R_7	the thermal resistance across the wick thickness in the condenser	$R_7 = \dfrac{\ln(r_i/r_v)}{2\pi L_c k_i}$
R_8	the thermal resistance across the thickness of the container wall in the condenser	$R_8 = \dfrac{\ln(r_o/r_i)}{2\pi L_c k_w}$
R_9	the thermal resistance between the condenser external surface and the heat sink	$R_9 = \dfrac{1}{h_c S_c}$
R_{10}	the axial thermal resistance of the container wall	$R_{10} = \dfrac{L_e + L_a + L_c}{\pi(r_o^2 - r_i^2)k_w}$
R_{11}	the axial thermal resistance of the wick structure	$R_{11} = \dfrac{L_e + L_a + L_c}{\pi(r_i^2 - r_v^2)k_i}$

Table 3.2: Comparative values for the heat pipe resistances, *adapted from Asselman and Green (1973)*.

Resistance	Description	$^\circ C/W$
R_1	external source	10^{+2} - 10^{-1}
R_2	evaporator wall	10^{-1}
R_3	evaporator wick	10^{+1}
R_4	evap. l/v interface	10^{-5}
R_5	axial vapour core	10^{-8}
R_6	cond. v/l interface	10^{-5}
R_7	condenser wick	10^{+1}
R_8	condenser wall	10^{-1}
R_9	external sink	10^{+2} - 10^{-1}
R_{10}	axial pipe wall	10^{+2}
R_{11}	axial wick layers	10^{+4}

The thermal resistances across the wick in the evaporator and the condenser, R_3 and R_7, are usually the most dominant and estimated assuming conduction heat transfer across the wick. The wick is assumed fully saturated with evaporation and condensation only at the interface of the wick and negligible convection and radiation within the wick. In order to sustain a finite evaporation or condensation rate, a temperature difference must exist at the interfaces between the liquid and the vapour (Dunn and Reay, 1978). This temperature difference gives rise to a thermal resistance, but is often small enough to be neglected. The vapour-liquid interface resistances, R_4 and R_6, can be calculated using the kinetic theory as proposed by Dunn and Reay (1978) as shown in table 3.1.

There is an overall pressure loss in the vapour flow between the evaporator and the condenser with a corresponding temperature difference. The effective thermal resistance of the vapour, R_5, although usually negligible, can be estimated as

$$R_5 = \frac{T_v(P_{v,e} - P_{v,c})}{\rho_v h_{fg} Q} \tag{3.1}$$

where the pressure drop can be estimated as (Dunn and Reay, 1978)

$$(P_{v,e} - P_{v,c}) = F_v Q \left(\frac{L_e}{6} + L_a + \frac{L_c}{6} \right) \tag{3.2}$$

where F_v is the vapour frictional coefficient defined as

$$F_v = \frac{C f_v Re_v \mu_v}{2r_v^2 (\pi r_v^2) \rho_v h_{fg}} \tag{3.3}$$

Here, μ_v is the viscosity of the vapour, C is a coefficient that accounts for the compressibility of the flow depending on the vapour Mach number, Ma_v, and f_v is the frictional drag coefficient depending on the vapour Reynolds number, Re_v. The vapour non-dimensional groups, namely, the vapour Reynolds number and the Mach number, are defined as follows

$$Re_v = \frac{2r_v Q}{(\pi r_v^2) \mu_v h_{fg}} \tag{3.4}$$

$$Ma_v = \frac{Q}{(\pi r_v^2)\rho_v h_{fg}\sqrt{\gamma_v R_v T_v}} \qquad (3.5)$$

The order of magnitude of these resistances for a typical application as estimated by Asselman and Green (1973) are compared in table 3.2. In comparing these values, it is apparent that several simplifications can be made. First, the liquid-vapour interface resistances and the axial vapour core resistance can be assumed to be negligible. Second, because of the comparative magnitudes of the resistance of the vapour core and the axial resistances of the pipe wall and wick structure, the axial resistances of both the pipe wall and the wick structure may be treated as open circuits and neglected except for the transient case where the capacitance of the adiabatic section should be considered.

Zuo and Faghri (1998) extended the steady-state network model described above for the transient response of a heat pipe. The heat transfer processes illustrated in figure 3.2(a) were represented using a network of thermal conductors as shown in figure 3.2(b) (Zuo and Faghri, 1998). The one-dimensional heat conduction for an element with a cross-sectional area of A_i and a thickness of λ_i can be written as (figure 3.2(c))

$$\rho_i A_i \lambda_i c_{p,i}\frac{dT_i}{dt} = Q_{i,1} - Q_{i,2} \qquad (3.6)$$

where

$$Q_{i,1} = k_i A_i \frac{T_{i,1} - T_i}{\lambda_i/2}; \qquad Q_{i,2} = k_i A_i \frac{T_i - T_{i,2}}{\lambda_i/2} \qquad (3.7)$$

Here, $T_{i,1}$ and $T_{i,2}$ are the two end temperatures and T_i is the temperature at the middle of the heat conductor. Eliminating $Q_{i,1}$ and $Q_{i,2}$ from equations 3.6 and 3.7 gives

$$\frac{dT_i}{dt} = \frac{2\alpha_i}{\lambda_i^2}\left(T_{i,1} + T_{i,2} - 2T_i\right) \qquad (3.8)$$

The above governing equation was written for each heat conductor considered in figure 3.2(b). With the conditions that at any vertex the net heat flow is zero, and the heat conductors with a common vertex have the same temperature at the corresponding ends; the governing equations of the heat pipe system shown in figure 3.2(b) are,

(a)

(b)

(c)
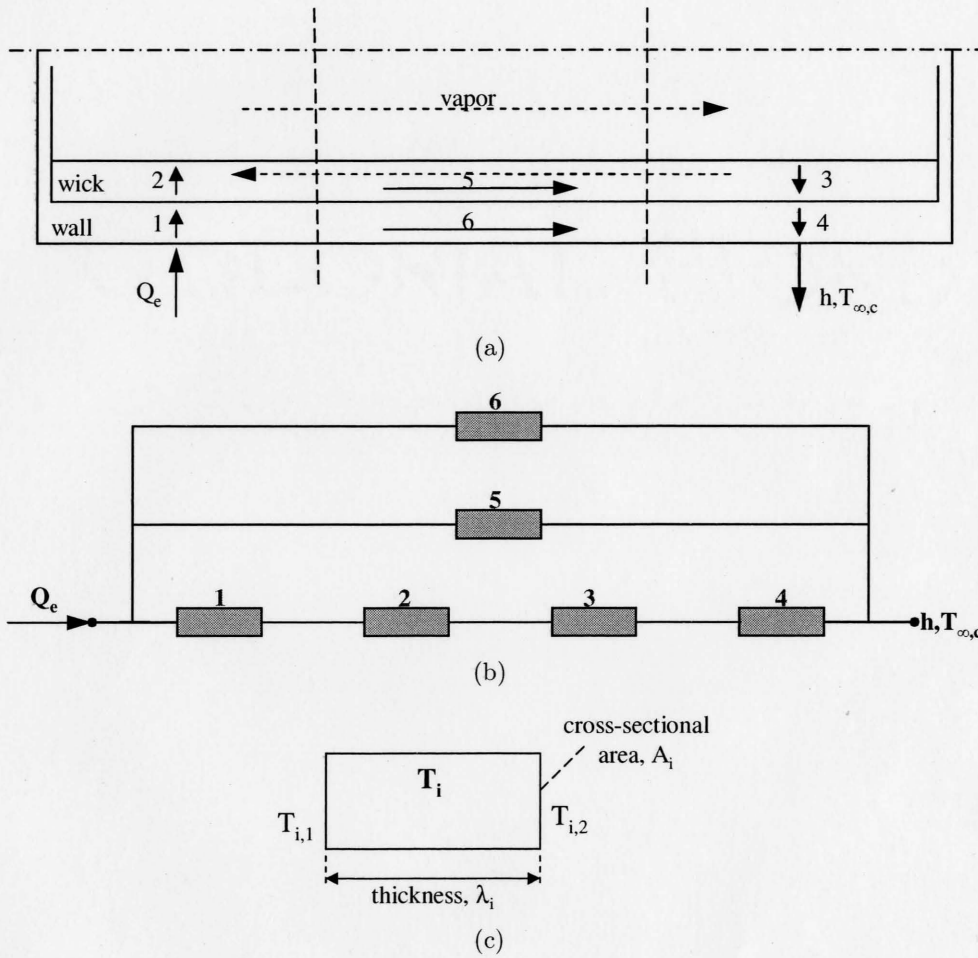
Figure 3.2: A network system of the heat pipe operation, (Zuo and Faghri, 1998): (a) a sketch of the heat pipe heat transfer processes, (b) a network analogy of the heat pipe heat transfer processes and (c) a one-dimensional heat conductor.

$$\frac{dT_1}{dt} = \frac{2\alpha_1}{\lambda_1^2}\left[(\eta_{12}+\zeta_1-2)T_1 + \eta_{21}T_2 + \zeta_5 T_5 + \zeta_6 T_6 + \frac{\zeta_1 Q_e/2}{k_1 A_1/\lambda_1}\right] \qquad (3.9)$$

$$\frac{dT_2}{dt} = \frac{2\alpha_2}{\lambda_2^2}\left[\eta_{12}T_1 + (\eta_{21}+\eta_{23}-2)T_2 + \eta_{32}T_3\right] \qquad (3.10)$$

$$\frac{dT_3}{dt} = \frac{2\alpha_3}{\lambda_3^2}\left[\eta_{23}T_2 + (\eta_{32}+\eta_{34}-2)T_3 + \eta_{43}T_4\right] \qquad (3.11)$$

$$\frac{dT_4}{dt} = \frac{2\alpha_4}{\lambda_4^2}\left[\eta_{34}T_3 + (\eta_{43}+\xi_4-2)T_4 + \xi_5 T_5 + \xi_6 T_6 + \frac{\xi_4 h_c S_c T_{\infty,c}/2}{k_4 A_4/\lambda_4}\right] \qquad (3.12)$$

$$\frac{dT_5}{dt} = \frac{2\alpha_5}{\lambda_5^2}\left[\zeta_1 T_1 + \xi_4 T_4 + (\zeta_5+\xi_5-2)T_5 + (\zeta_6+\xi_6)T_6\right.$$
$$\left. + \frac{\zeta_5 Q_e/2}{k_5 A_5/\lambda_5} + \frac{\xi_5 h_c S_c T_{\infty,c}/2}{k_5 A_5/\lambda_5}\right] \qquad (3.13)$$

$$\frac{dT_6}{dt} = \frac{2\alpha_6}{\lambda_6^2}\left[\zeta_1 T_1 + \xi_4 T_4 + (\zeta_5+\xi_5)T_5 + (\zeta_6+\xi_6-2)T_6\right.$$
$$\left. + \frac{\zeta_6 Q_e/2}{k_6 A_6/\lambda_6} + \frac{\xi_6 h_c S_c T_{\infty,c}/2}{k_6 A_6/\lambda_6}\right] \qquad (3.14)$$

where,

$$\eta_{ij} = \frac{k_i A_i/\lambda_i}{k_i A_i/\lambda_i + k_j A_j/\lambda_j} \qquad (3.15)$$

$$\zeta_i = \frac{k_i A_i/\lambda_i}{k_1 A_1/\lambda_1 + k_5 A_5/\lambda_5 + k_6 A_6/\lambda_6} \qquad (3.16)$$

$$\xi_i = \frac{k_i A_i/\lambda_i}{k_4 A_4/\lambda_4 + k_5 A_5/\lambda_5 + k_6 A_6/\lambda_6 + h_c S_c/2} \qquad (3.17)$$

In this approach, the governing equations for the transient response were simplified by Zuo and Faghri (1998) to a set of linear first-order ordinary differential equations making them quicker to solve. The results from this model were in good agreement with the more detailed two dimensional model by Cao and Faghri (1990) with a computational time that was approximately 5% of that for the two-dimensional model. However, this model did not include the effect of the surrounding media nor can it account for non-uniform boundary conditions at the evaporator or the condenser. The effect of non-condensable gases were also not included in this model.

3.2   Improved Network Model

The above system was expanded in this investigation to incorporate the effects of heat transfer in the wall and wick, heat transfer in the surrounding media, and non-condensable gases in the vapour region. The thermal resistance of the different components was broken down into a larger number of smaller resistances in both axial and radial directions to account for the axial conduction and to handle non-uniform boundary conditions. Thus, the model is a hybrid between the network model and a full two-dimensional model. A schematic of the expanded network model is shown in figure 3.3. The wall and the wick were divided into annular layers in the radial direction where every layer contained a large number of resistances in the axial direction. The same was considered for the surrounding media (an evaporator block in this case).

The nomenclature used in figure 3.3(c) is given in table 3.3. A typical two-dimensional element or conductor in this network is shown in figure 3.3(b) with a cross-sectional area of A_i, a thickness of L_i, and an internal and external radius of $r_{i,i}$ and $r_{i,o}$ respectively. The interface temperatures for this element are $T_{i,a}$, $T_{i,b}$, $T_{i,c}$ and $T_{i,d}$. The energy balance for each element is given by

$$\rho_i c_{p,i} V_i \frac{dT_i}{dt} = \sum Q = Q_{i,a} + Q_{i,b} + Q_{i,c} + Q_{i,d} \qquad (3.18)$$

where the volume of each conductor was evaluated to account for the variation in the radial direction, and is given by

$$V_i = L_i \pi (r_{i,o}^2 - r_{i,i}^2) \qquad (3.19)$$

and the heat transfer is

$$Q_{i,a} = \frac{T_{i,a} - T_i}{R_{z,i}/2}, \quad Q_{i,b} = \frac{T_{i,b} - T_i}{R_{z,i}/2}, \quad Q_{i,c} = \frac{T_{i,c} - T_i}{R_{r,i}/2}, \quad Q_{i,d} = \frac{T_{i,d} - T_i}{R_{r,i}/2} \qquad (3.20)$$

27

(a)

(b)

(c)
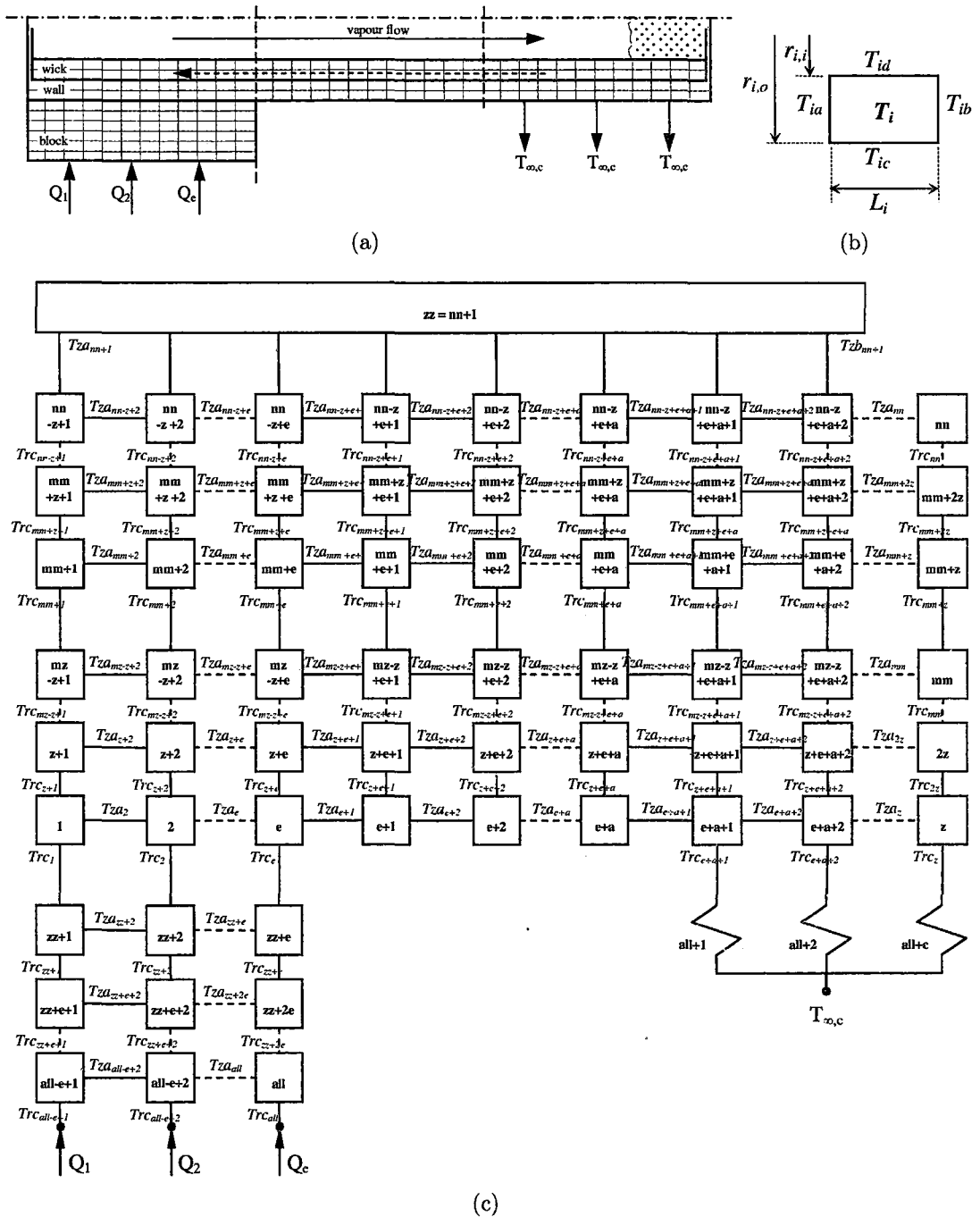
Figure 3.3: The new network system of the heat pipe operation: (a) a sketch of the heat pipe heat transfer processes, (b) a two-dimensional heat conductor and (c) a network analogy of the heat pipe heat transfer processes.

Table 3.3: Description for the numbers used in figure 3.3(c).

Symbol	Formula	Description
e	-	axial number of conductors in evaporator
a	-	axial number of conductors in adiabatic
c	-	axial number of conductors in condenser
z	$z = e + a + c$	total axial number of conductors in one layer
m	-	radial number of layers in the wall
n	-	radial number of layers in the wick
k	-	radial number of layers in the block
mm	$mm = (m)(z)$	total number of conductors for the wall
nn	$nn = mm + (n)(z)$	total number of conductors for wall and wick
zz	$zz = nn + 1$	total number for the wall, wick and vapour
all	$all = zz + (k)(e)$	total number of conductors for the system

The thermal resistances in the axial and radial directions are given by

$$R_{z,i} = \frac{L_i}{\pi(r_{i,o}^2 - r_{i,i}^2)k_i}, \quad R_{r,i} = \frac{ln(r_{i,o}/r_{i,i})}{2\pi L_i k_i} \tag{3.21}$$

Rearranging equations 3.18 and 3.20 results in

$$\frac{dT_i}{dt} = \frac{2}{\rho_i c_{p,i} V_i} \left[\frac{(T_{i,a} + T_{i,b} - 2T_i)}{R_{z,i}} + \frac{(T_{i,c} + T_{i,d} - 2T_i)}{R_{r,i}} \right] \tag{3.22}$$

The effect of heat convection due to the liquid flow in the wick structure relative to the conduction in the radial direction can be expressed by (Sun and Tien, 1972)

$$N \equiv \frac{q c_{p,i} \Delta L (T_w - T_s)/h_{fg}}{(T_w - T_s) k_i \Delta L/t_i} = \frac{q c_{p,i} t_i}{h_{fg} k_i} \tag{3.23}$$

where q is the input heat flux, $c_{p,i}$ is the specific heat capacity of the liquid flow, T_w is the pipe wall temperature, T_s is the saturated vapour temperature, h_{fg} is the latent heat, k_i is the wick structure thermal conductivity, and t_i is the thickness of the wick layers. The value of N is found to be less that 10^{-2} for copper-water heat pipes operating at low and medium temperature ranges. Therefore, the convection heat transfer due to the liquid flow in the wick structure can be neglected here, so equation 3.22 represents the governing equation of the components in the wick as well as the wall.

The governing equation for each conductor (equation 3.22) relative to the adjacent conductors can be formulated, resulting in a system of linear first-order ordinary differential equations. The axial and radial resistances were calculated using equation 3.21 for all the heat conductors in the wall, wick and the block, while equation 3.1 was used for the vapour heat conductor.

The non-condensable gases were incorporated in the model and were modeled following the approach of Sun and Tien (1975). In this approach, the active length of the condenser is estimated by

$$m_g = \frac{P_{g,i}}{R_g T_{g,i}} A_v (L_c - L_{c,a}) \tag{3.24}$$

30

where m_g is the mass of the non-condensable gas, $P_{g,i}$ is the partial pressure of gas in the inactive portion of the condenser, $T_{g,i}$ is the temperature of gas in the inactive portion of the condenser, A_v is the vapour core cross-sectional area, L_c is the total length of the condenser, and $L_{c,a}$ is the length of the active portion of the condenser. The non-condensable gas is treated as an ideal gas here with a gas constant R_g. Since the total pressure in the inactive part of the condenser is equal to the vapour pressure at the active part of the condenser $P_{v,a}$, the partial pressure of the gas in the inactive part of the condenser can be calculated as

$$P_{g,i} = P_{v,a} - P_{v,i} \qquad (3.25)$$

where $P_{v,i}$ is the partial pressure of the vapour in the inactive part of the condenser. Thus, the active length of the condenser is given by (Sun and Tien, 1975)

$$L_{c,a} = L_c - \frac{m_g R_g T_{g,i}}{(P_{v,a} - P_{v,i})A_v} \qquad (3.26)$$

The vapour pressure in the inactive part of the condenser $P_{v,i}$ is equal to the saturation vapour pressure at the temperature of the non-condensable gas in the condenser $T_{g,i}$. In the absence of heat transfer in the inactive length of the condenser, it is assumed that the gas is in thermal equilibrium with the sink, i.e., $T_{g,i} = T_{s,c}$. In this case, equation 3.26 can be written as

$$L_{c,a} = L_c - \frac{m_g R_g T_{s,c}}{(P_{v,a} - P_{v,s})A_v} \qquad (3.27)$$

where $P_{v,a}$ and $P_{v,s}$ are saturation vapour pressures at $T_{v,a}$ and $T_{s,c}$, respectively. The active condenser length is calculated at each time-step of the network model based on the results from the previous time-step.

The active length is compared to the actual length of each heat conductor in the grid layer of the wick structure at the interface with the vapour and then a new matrix of the corrected length is formulated for these conductors. Values of whole length, part of the length or zero are assigned to each conductor depending on whether

the conductor is fully active, partially active or fully inactive respectively. The new matrix of the corrected lengths is used only for the radial heat transfer, while the complete physical lengths are used for the axial heat transfer. It is important to note that the above assumes knowing the amount of non-condensable gases, m_g, a priori.

3.3 Solution Methodology

The expanded model consisting of a set of first-order linear ordinary differential equations, including the effect of non-condensable gases, was solved using the fourth-order Runge-Kutta method with adaptive time steps as discussed by Dormand and Prince (1980). It is based on an explicit Runge-Kutta formula, the Dormand-Prince pair. The system of equations was solved using a program that was coded in MATLAB®. A relative error tolerance for all components of the solution vector is specified, and the code determines the adaptive time step accordingly so that the estimated error in each integration step satisfies the specified criteria. As the relative error tolerance is decreased, improved results are obtained at the cost of increased computational time. The spatial and the temporal convergence analysis is discussed in detail in the following section. The source code is presented in Appendix A.

As the grid and time step are refined, the spatial and temporal discretization errors should asymptotically approach zero, excluding computer round-off error. Methods for examining the spatial and temporal convergence are presented in Roache (1998) that are based on use of Richardson's extrapolation. This method was used to evaluate the convergence of the solution, a summary of which is presented here.

The solution error is defined here as the difference between the discrete solution and the exact solution,

$$E = f(h) - f_{exact} = Ch^p + H.O.T. \tag{3.28}$$

where C is a constant, h is the length of each conductor as a measure of grid spacing, p is the order of convergence, and $H.O.T.$ represents the higher-order terms. A "second-order" solution would have $p = 2$.

Neglecting higher-order terms and taking the logarithm of both sides of the above equation results in,

$$\log(E) = \log(C) + p\log(h) \tag{3.29}$$

The order of convergence p can be obtained from the slope of the curve of $\log(E)$ versus $\log(h)$. A more direct evaluation of p can be obtained from three solutions using a constant grid refinement ratio r,

$$p = \ln\left(\frac{f_3 - f_2}{f_2 - f_1}\right) / \ln(r) \tag{3.30}$$

For the current study, the vapour temperature is used to verify the spatial and temporal convergence. The boundary conditions were set to a step heat input $Q_{in} = 100\,Watts$ at the evaporator end and a constant sink temperature $T_{c,\infty} = 20°C$ at the condenser end. The simulations used three grids, each with twice the number of conductors as the previous one. Table 3.4 shows the grid information normalized by the finest grid and the resulting vapour temperature at steady state. The change in the vapour temperature with the normalized grid spacing is shown in figure 3.4. As the grid spacing reduces, the vapour temperature approaches an asymptotic zero-grid spacing value. The order of convergence is determined to be $p = 2.3$ using equation 3.30.

Evaluating the accuracy of the code requires that the grid is sufficiently refined such that the solution is in the asymptotic range of convergence. The asymptotic range of convergence is obtained when the grid spacing is such that the various grid spacings h and errors E result in the constancy of C,

$$C = E/h^p \tag{3.31}$$

The value at zero grid spacing from a series of values at larger grid spacings can be estimated using Richardson extrapolation method. A simulation will result in a

Table 3.4: Spatial convergence results.

Grid Step	Physical Grid Spacing (mm)	Normalized Grid Spacing	Vapour Temperature (K)
1	2	1	307.455751038616
2	4	2	307.478374384686
3	8	4	307.589699716293
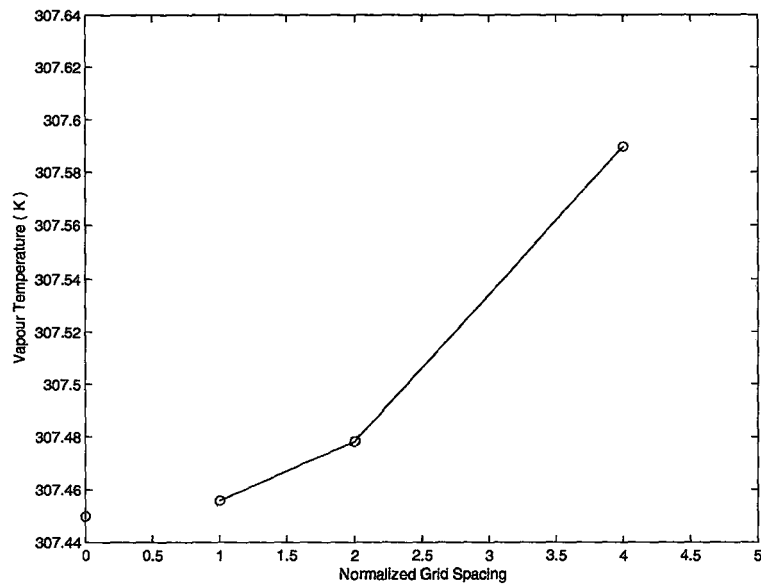
Figure 3.4: Spatial convergence results.

quantity, or the vapour temperature T_v in this study, that could be expressed by,

$$f = f_{h=0} + g_1 h + g_2 h^2 + g_3 h^3 + \ldots \tag{3.32}$$

where h is the grid spacing and the functions g_1, g_2, and g_3 are independent of the grid spacing. The $f_{h=0}$ is the vapour temperature value at zero grid spacing.

For a pth order solution, if the quantity f is computed on two grids of spacing h_1 and h_2 with h_1 being the finer spacing, then we can write two equation for the above expansion, neglecting the higher-order terms, and solve for $f_{h=0}$,

$$f_{h=0} \cong f_1 + \frac{f_1 - f_2}{r^p - 1} \tag{3.33}$$

where the grid refinement ratio r is,

$$r = h_2/h_1^{\cdot} \tag{3.34}$$

Using the two finest grids, an estimate of the vapour temperature at zero grid spacing, using equation 3.33 is obtained as, $T_v = 307.45K$; which is very close to the vapour temperature using the fine grid spacing as shown in figure 3.4.

A grid convergence index GCI was introduced by Roache (1997) to provide a consistent way in presenting the results of grid convergence studies and provide an error band on the grid convergence of the solution. The GCI is a measure of how far the computed value is away from the asymptotic numerical value. It indicates how much the solution would change with a further refinement of the grid.

The GCI on the fine and coarse grids are defined as,

$$GCI_{fine} = GCI_{12} = \frac{F_s \, |\varepsilon|}{(r^p - 1)} = \frac{F_s \, |(f_2 - f_1)/f_1|}{(r^p - 1)} \tag{3.35}$$

$$GCI_{coarse} = GCI_{23} = \frac{F_s \, |\varepsilon| \, r^p}{(r^p - 1)} = \frac{F_s \, |(f_3 - f_2)/f_2| \, r^p}{(r^p - 1)} \tag{3.36}$$

where ε is the relative error, and F_s is a factor of safety. The refinement may be spatial or temporal. The factor of safety is recommended to be $F_s = 3.0$ for comparing two

Table 3.5: Spatial convergence GCI values.

Grid Steps	Refinement Ratio (r)	GCI (%)
$1 \leftrightarrow 2$	2	0.00234589045688467
$2 \leftrightarrow 3$	2	0.0115428468036945

grid sizes and $F_s = 1.25$ for comparing three or more grid sizes.

To determine if the chosen grid size yields solution that is in the asymptotic range of convergence, two GCI values computed over three grids are compared,

$$GCI_{23} = r^p GCI_{12} \tag{3.37}$$

If the ratio between both sides of the above equation is approximately 1, this means that the solution is in the asymptotic range of convergence. The grid convergence index for the fine and coarse grid solutions of the current study using $F_s = 1.25$, GCI_{12} and GCI_{23} are summarized in table 3.5. The ratio,

$$\frac{GCI_{23}}{r^p GCI_{12}} = 0.999926422968396 \tag{3.38}$$

is approximately one, indicating that the solutions are well within the asymptotic range of convergence.

The same procedure was used to check the temporal convergence of the current model, for the same boundary conditions. A relative error tolerance for all components of the solution vector is specified, and the code determines the adaptive time step accordingly so that the estimated error in each integration step satisfies the specified criteria. As the relative error tolerance is decreased, improved results are obtained at the cost of increased computational time. The simulations used three relative tolerances, each twice the previous one. Table 3.6 shows the normalized relative tolerances and the resulting vapour temperature at steady state.

The change in the vapour temperature with the relative tolerance is shown in figure 3.5. As the relative tolerance reduces, the vapour temperature approaches an asymptotic zero-grid spacing value.

Table 3.6: Temporal convergence results.

Step	Actual Relative Tolerance	Normalized Relative Tolerance	Vapour Temperature (K)
1	1×10^{-4}	1	307.455751038616
2	2×10^{-4}	2	307.464486921574
3	4×10^{-4}	4	307.487251196944
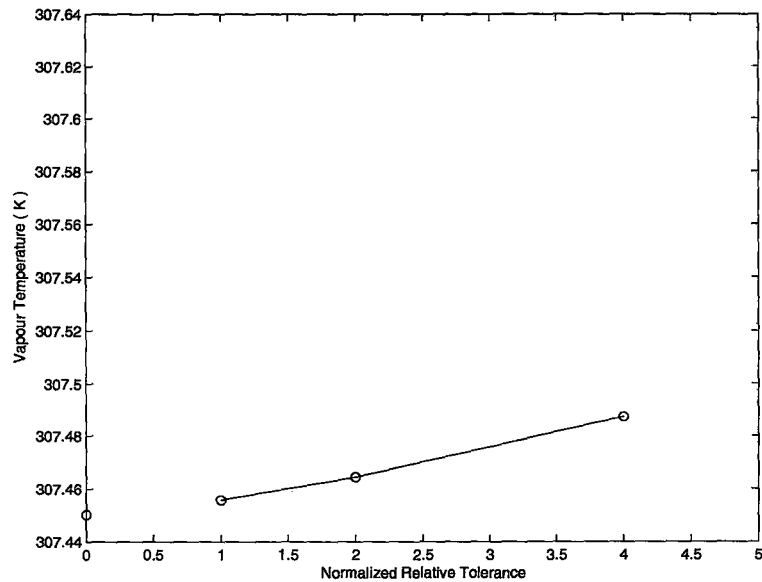
Figure 3.5: Temporal convergence results.

Table 3.7: Temporal convergence GCI values.

Steps	Refinement Ratio (r)	GCI (%)
$1 \leftrightarrow 2$	2	0.00221173504689425
$2 \leftrightarrow 3$	2	0.00576325431093416

The order of convergence in this case is determined to be $p = 1.4$. The value of the vapour temperature at zero grid spacing, using equation 3.33, is $T_v = 307.45K$.

The grid convergence index for the fine and coarse solutions can now be computed using equations 3.35 and 3.36, respectively. A factor of safety of $F_s = 1.25$ is used since three steps were used to estimate p. The values for GCI_{12} and GCI_{23} are summarized in table 3.7. The ratio between both sides

$$\frac{GCI_{23}}{r^p GCI_{12}} = 0.999971587343157 \tag{3.39}$$

is approximately one and indicates that the solutions are well within the asymptotic range of convergence.

3.4 Material Properties

All material properties (including the coolant fluid) were calculated as temperature dependent by interpolating through tables of the thermo-physical properties adapted from Incropera and DeWitt (1996) at every time step. The wick modeled here is a standard wire screen plain woven mesh, with a porosity calculated using the method of Marcus (1972),

$$\epsilon = 1 - \pi SNd/4 \tag{3.40}$$

where S is a crimping factor that takes into account the fact that the wires are not simply crossed with a value of approximately 1.05. The mesh number N, defined as the number of openings per unit length, is found from

$$N = 1/(d + w) \tag{3.41}$$

where d is the diameter of the wire and w is the width of the openings.

The effective thermal conductivity for heterogeneous fluid-saturated screen wicks depends on the geometric parameters and the thermal conductivities of the solid and fluid. The effective thermal conductivity was estimated using the method of Chang (1990) as

$$
k_{\textit{eff}} = \frac{k_f}{(1+A)^2}\left\{\alpha^2 A\left[\frac{\alpha A}{\alpha - \pi\beta(1 - k_f/k_s)/2}\right.\right.
$$
$$
\left.\left. + \frac{2[1 + A(1 - \alpha)]}{\alpha - \pi\beta(1 - k_f/k_s)/4}\right] + [1 + A(1 - \alpha)]^2\right\} \quad (3.42)
$$

where k_f and k_s are the thermal conductivities of the fluid and solid respectively, $A = d/w$, $B = d/t$ and t is the thickness of a layer of screen. The constant α is calculated from the empirical function

$$
\alpha = 1.11716 - 0.07024 \log_{10}(k_s/k_f) \quad (3.43)
$$

determined from experimental measurements of the effective conductivity, and thus accounts for the effect of contact resistance and compression of the wick. The effective heat capacity of the wick structure is related to the porosity of the screen mesh and the heat capacities of the solid and fluid by (Faghri, 1995)

$$
(\rho c_p)_{\textit{eff}} = \epsilon\, \rho_f\, c_{p,f} + (1 - \epsilon)\, \rho_s\, c_{p,s} \quad (3.44)
$$

where ϵ is the porosity of the screen mesh, ρ_f, ρ_s and $c_{p,f}$, $c_{p,s}$ are the density and the specific heat capacity of the fluid and solid materials, respectively.

3.5 Boundary Conditions

At the evaporator end of the heat pipe, the rate of heat transfer, Q_e is specified along the outside surface of the evaporator section or along the external surface of the block. At the condenser end of the heat pipe, two different boundary conditions were investigated in this study. In the first case, a water jacket was used as illustrated in

figure 3.6(a); and in the second case a finned configuration was used as illustrated in figure 3.6(b). For both cases, the external resistance at each node of the condenser is specified as

$$R_c = \frac{1}{2\pi r_{i,o} L_i h_c} \tag{3.45}$$

where $r_{i,o}$ is the outside radius of the node, L_i is the length of the node, and h_c is the heat transfer coefficient.

For the parallel flow heat exchanger configuration, the Nusselt number, Nu, for laminar flow ($Re < 2300$) in the annular passage was obtained from table 3.8 as suggested by Incropera and DeWitt (1996). Here, d_o is the heat pipe outside diameter, d_p is the inside diameter of the cooling jacket, and Nu is defined as

$$Nu \equiv \frac{h_c d_h}{k} \tag{3.46}$$

where k is the fluid thermal conductivity, and d_h is the hydraulic diameter defined as

$$d_h = d_p - d_o \tag{3.47}$$

For turbulent flow ($Re > 2300$), the Nusselt number was evaluated using the Dittus-Boelter equation,

$$Nu = 0.023 Re^{4/5} Pr^{0.4} \tag{3.48}$$

where Pr is the fluid Prandtl number, Re is the Reynolds number based on the hydraulic diameter.

For the finned configuration, the external resistance at each node is specified depending on whether a fin is present at the node. For the bare nodes, the external resistance is defined as

$$R_{c,b} = \frac{1}{2\pi r_{i,o} L_i h_b} \tag{3.49}$$

while for the finned nodes, the external resistance is defined as

$$R_{c,f} = \frac{1}{2\pi (r_{fc}^2 - r_o^2) h_f \eta_f} \tag{3.50}$$

(a)

(b)
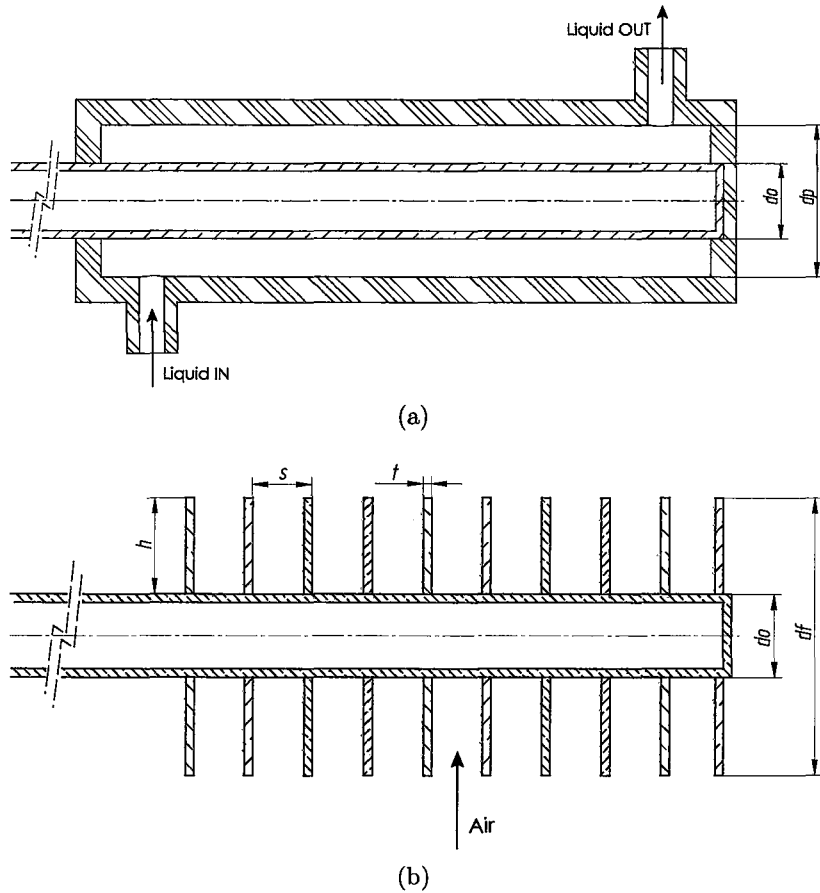
Figure 3.6: Condenser cooling schemes: (a) parallel pipe flow heat exchanger (Liquid/HP interface) and (b) finned configuration (Air/HP interface).

Table 3.8: Nusselt number for laminar flow in a circular tube annulus, *adapted from Incropera and DeWitt (1996)*.

d_o/d_p	Nu
0.00	–
0.05	17.46
0.10	11.56
0.25	7.37
0.50	5.74
1.00	4.86

41

where $r_{fc} = r_f + t/2$ is the corrected fin radius to account for the active convecting tip, r_f is the fin radius, r_o is the heat pipe outside radius, t is the fin thickness, and η_f is the fin efficiency defined for the circular fin as the heat transfer rate from the fin divided by the heat transfer rate if the fin were uniformly at the tube wall temperature and can be calculated using

$$\eta_f = \frac{(2r_o/m)}{(r_{fc}^2 - r_o^2)} \left(\frac{K_1(mr_o)I_1(mr_{fc}) - I_1(mr_o)K_1(mr_{fc})}{I_0(mr_o)K_1(mr_{fc}) + K_0(mr_o)I_1(mr_{fc})} \right) \tag{3.51}$$

where I_0 and K_0 are modified zero-order Bessel functions of the first and second kinds respectively, I_1 and K_1 are modified first-order Bessel functions of the first and second kinds respectively, and $m \equiv \sqrt{2h_f/kt}$.

The heat transfer coefficient for the finned nodes are calculated using the correlation given by Briggs and Young (1963)

$$Nu_f = 0.134Re^{0.681}Pr^{1/3} \left(\frac{s}{h} \right)^{0.2} \left(\frac{s}{t} \right)^{0.1134} \tag{3.52}$$

where Nu and Re are based on the outside heat pipe diameter, and s/h and s/t are the ratios of the fin pitch to fin height and fin pitch to fin thickness respectively. The heat transfer coefficient for the bare nodes are calculated using the correlation given by Churchill and Bernstein (1977) for a cross flow over a cylinder

$$Nu_b = 0.3 + \frac{0.62Re^{1/2}Pr^{1/3}}{\left[1 + (0.4/Pr)^{2/3}\right]^{1/4}} \left[1 + \left(\frac{Re}{282000}\right)^{5/8}\right]^{4/5} \tag{3.53}$$

where Nu and Re are based on the outside heat pipe diameter, and all the fluid properties are evaluated at the film temperature. The above correlation was modified by Hashizume et al. (2003) to incorporate the effect of fins as

$$Nu_{b,c} = Nu_b \left\{ exp \left[0.272 \left(1 - 5 \left(\frac{h}{s} \right) \right) Re^{-1/4} \right] \right\} \tag{3.54}$$

where h/s is the ratios of the fin height to fin pitch.

CHAPTER 4
EXPERIMENTAL FACILITY

Experiments were performed to investigate the effect of different boundary conditions, surrounding media and wick thickness on the steady and transient performance of copper-water heat pipes with wire screen mesh wicks. The data was also used to evaluate the improved network model developed here under the different boundary conditions. The experiments were performed for the case where the heat pipe was uniformly heated over a section on one end of the heat pipe and cooled with a water jacket on the other end of the heat pipe. Experiments were also performed with a finned condenser in a wind tunnel. In this chapter, the experimental facilities and the instrumentation including the heat pipes are presented. The experimental procedures for both the steady-state and transient tests are described in detail along with an uncertainty analysis.

4.1   Test Facility

A schematic of the experimental test facility using the water jacket condenser is shown in figure 4.1. The heat pipes used in this study had an outer diameter of 19.05 mm and length of 355.6 mm. Another set of heat pipes were also tested, which had the same outer diameter but a length of 300 mm. The heat pipes were heated at one end over a length of 101.6 mm and cooled at the other end over a length of 152.4 mm. The length between the heated and cooled sections was insulated using 8 layers of 3.175 mm FiberFrax® 970 ceramic insulation.

The evaporator section of the heat pipe was clamped between two halves of an aluminum evaporator block. The surface of the block was heated using a 1.8 m long OMEGALUX® 5 mm diameter rope heater. The maximum capacity of the heater was 200 $Watts$. The evaporator end of the heat pipe was coated with OMEGATHERM®
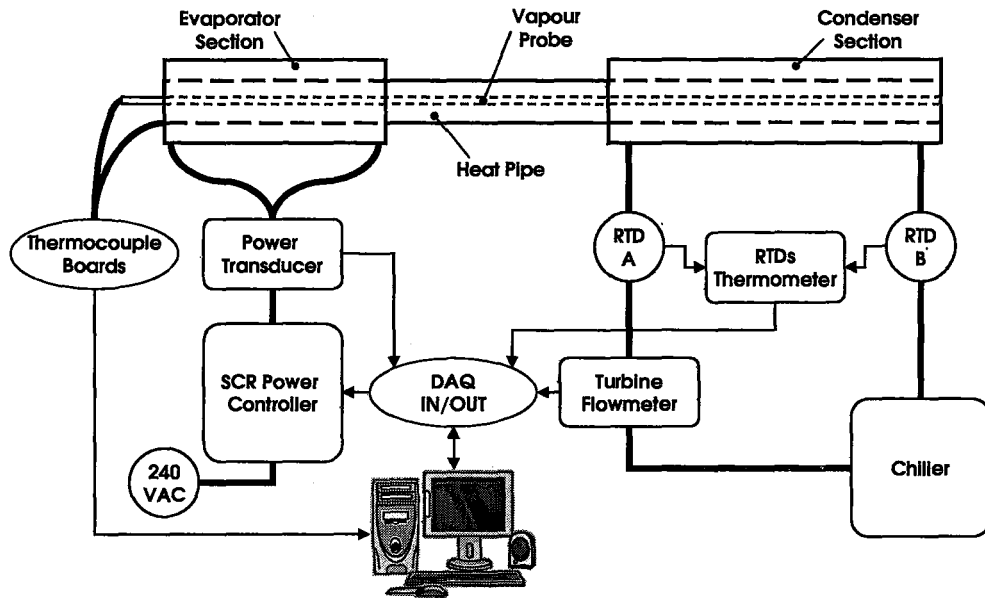
Figure 4.1: A Schematic diagram of the experimental test facility.
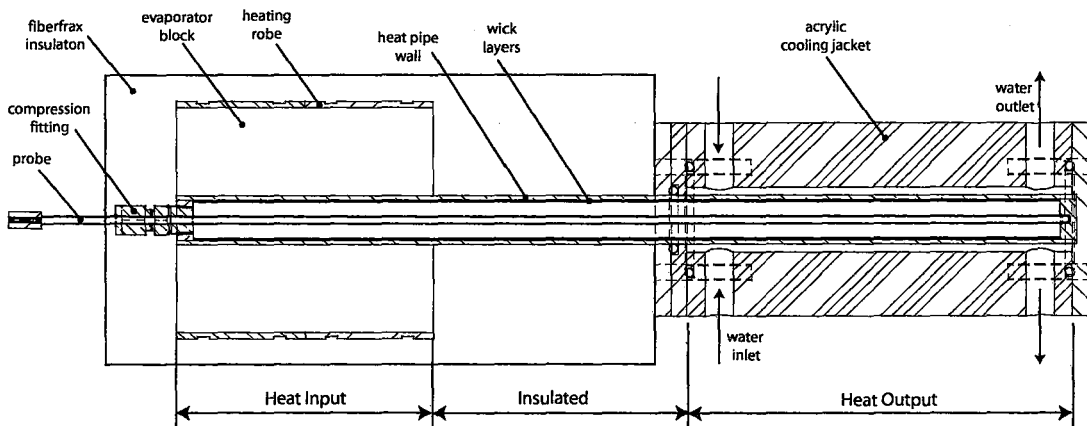
Figure 4.2: A cross-section of the heat pipe test section.

201 thermal conducting paste before clamping the evaporator block to minimize the contact resistance.

The effect of surrounding media on the transient performance of wicked heat pipes was examined here using two aluminum evaporator blocks beside the case where the heat was applied directly to the heat pipe wall. Both blocks had a length of 101.6 *mm* as shown in figure 4.3, with outer diameters of 88.9 *mm* and 38.1 *mm*.

The electrical power to the rope heater was supplied using a Watlow DIN-A-MITE® Style C solid-state SCR power controller. The model used is DC10-24S5-0000 with single-cycle variable time base that work with a linear voltage input of 0 to 10 *volts*. The input signal was computer controlled through an analog output using a data acquisition board with LabVIEW®. The electrical power used by the heater was measured by an Ohio Semitronics PC5-011D Watt transducer. The entire evaporator section was clamped between two halves of a wooden block lined with 25.4 *mm* of FiberFrax® 970 ceramic insulation to prevent heat loss to the ambient.

The condenser section of the heat pipe was cooled using an acrylic water jacket with an inner diameter of 25.4 *mm* and length of 152.4 *mm*. The cooling water entered and exited the water jacket through two 11.13 *mm* diameter ports positioned 12.7 *mm* from each end of the condenser section. Chilled water was supplied from a Lytron RC045 chiller that allowed the temperature of the cooling water to be controlled to ±0.1°C. The water flow rate was measured using an Exact-Flow dual-rotor turbine flow meter installed before the water jacket. The inlet and outlet temperatures of the cooling water were measured using two 4-wire platinum resistance thermometers with an Omega DP251 RTD precision thermometer. The plastic hose connecting the chiller to the water jacket was 12.7 *mm* and was insulated with foam insulation. All fittings used were plastic and wrapped in foam insulation to minimize heat transfer from the ambient.

The thermocouples from the heat pipes and the vapour probe were connected to a 16 channel PCI-DAS-TC thermocouple board. The output from the turbine flow meter, the RTD thermometer, and the power transducer were connected to a National Instruments BNC-2090 data acquisition board. An analog output channel
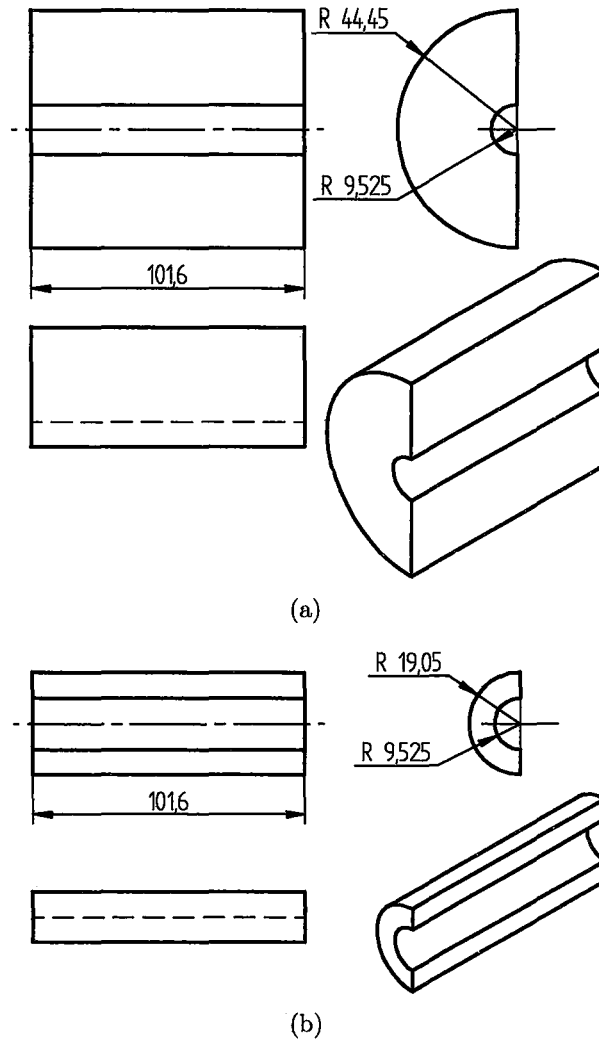
Figure 4.3: Different evaporator blocks used: (a) big block and (b) small block.

in the same board was used to control the SCR power controller to the specified signal type. A desktop computer was used to sample the data continuously at 60 Hz using a LabVIEW® program.

The heat pipes with the finned condenser were tested in a wind tunnel test facility (figure 4.4) that is described in detail by Grover (1977). Air is drawn through a polished birch plywood contraction, through the test section, then expanded gradually through a square-to-round diffuser until it reaches the vane-axial fan to exhaust as shown in figure 4.4. The contraction is from 1.45 m square at the inlet to 0.3048 m square at the test section (a contraction ratio of about 22:1) with a contraction length of 1.14 m. The contraction section upstream of the working test section considerably reduces the spatial variations in the velocity distribution and also results in a lower turbulence level at the working test section. The wall contours are designed so as to be free from adverse pressure gradients to avoid boundary layer separation. The velocity distribution at the test section is uniform to within 1% with average turbulence intensity of about 0.2% over the range of operating speeds as reported by Grover (1977).

The test section is 0.825 m long with an internal cross section that is 0.3048 m square, constructed of 19.05 mm thick clear acrylic as shown in figure 4.5. The wind tunnel fan is driven by a 10 hp D.C. motor than can be controlled to within ± 1 rpm using a speed controller. The maximum air flow is 3.8 m^3/s of air at 0.038 mm H_2O static pressure corresponding to 40 m/s in the test section. The flow velocity in the test section was measured by using a pitot-static probe and a Dwyer MFG inclined U-Tube manometer. The tests were performed over a velocity range from 2.9 to 32 m/s.

The reading of the surface thermocouples from the heat pipes and the output from the power transducer were recorded. The details of the heat pipe instrumentation used in the water jacket tests and the finned condenser heat pipes are described in the next section.
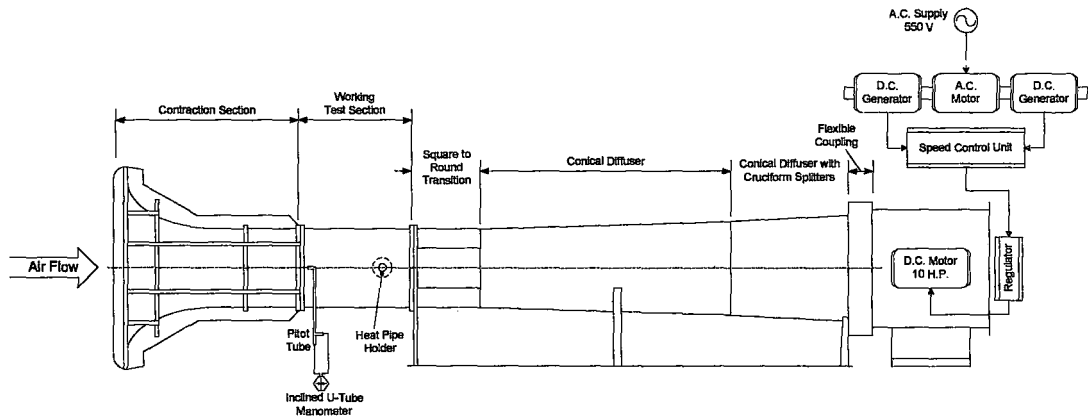
Figure 4.4: Wind Tunnel test facility, *adapted from Grover (1977)*.
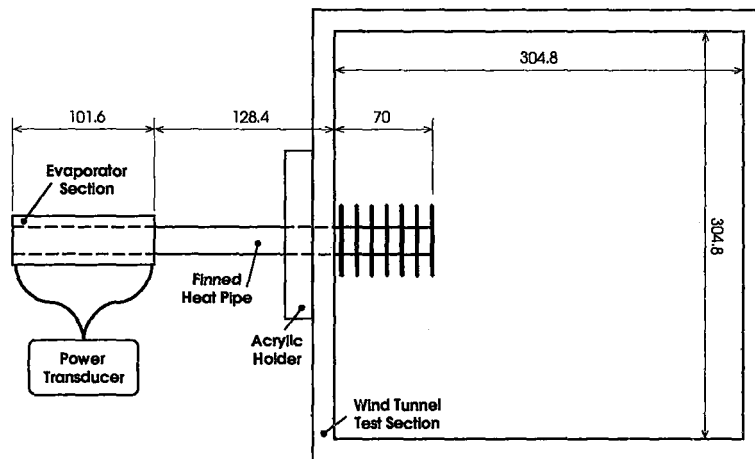
Figure 4.5: A cross-section in the wind tunnel test facility showing the position of the finned heat pipe.

4.2   Heat Pipe Instrumentation

Two sets of heat pipes were used in this study; one set for the tests with the cooling water jacket and the other for the tests with the finned condenser in the wind tunnel. Different methods of instrumentation were used for each of these sets as will be discussed in this section.

The wick structure in the heat pipes was made from a woven copper wire screen mesh. The screen mesh had a wire diameter of $0.109mm$ and consisted of 3937 strands per meter (100 strands/inch). The heat pipes used in this study had 2, 3 and 4 layers of the copper screen mesh as shown in figure 4.6. The porosity of the wick structure was 0.645, computed using the model suggested by Marcus (1972). It was assumed that the degree of intermeshing in the wick was negligible so that the porosity of the wick was independent of the number of mesh layers in the wick. The volume of fluid required to saturate the wick was estimated by multiplying the porosity of the wire screen mesh by the bulk volume of the wick structure.

The tests with cooling water jacket were performed using copper-water heat pipes as shown schematically in figure 4.7 and with 3 and 4 wick layers. The heat pipes had an outer diameter of 19.05 mm, wall thickness of 1.65 mm, and length of 355.6 mm. Each heat pipe was charged with the amount of fluid required to fully saturate the wick and the amount of fluid loading corresponding to each heat pipe
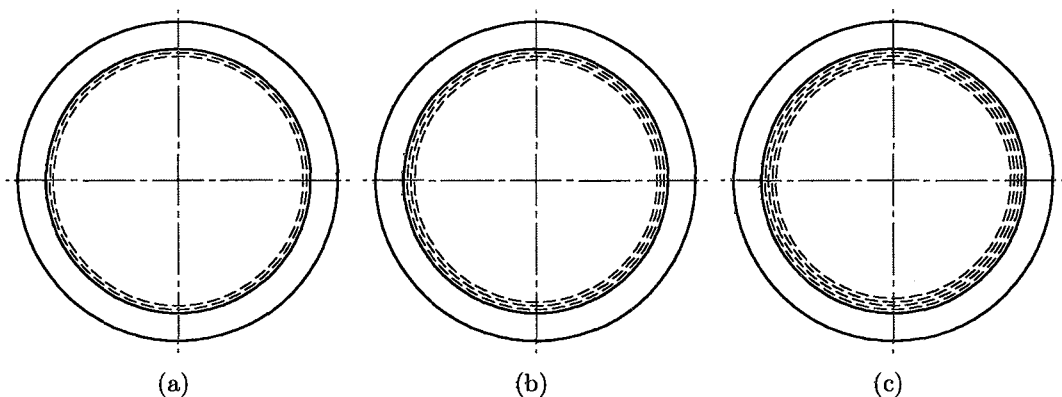
Figure 4.6: Heat pipe configurations used: (a) 2 wick layers, (b) 3 wick layers and (c) 4 wick layers.

Table 4.1: Fluid loading values for different heat pipes.

Heat Pipe	Number of Wick Layers	Fluid Loading (grams of water)
1	2	4.82
2	3	7.13
3	4	9.37
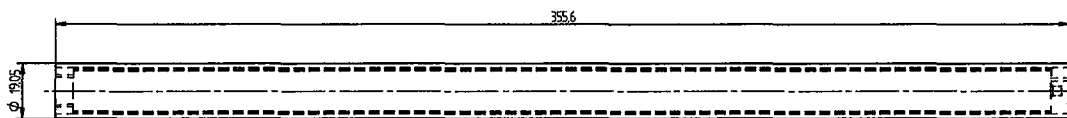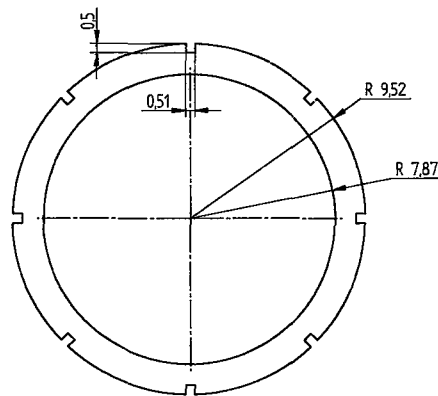
Figure 4.7: Schematic of (a) heat pipe and (b) cross-section showing the grooves for the surface thermocouples.
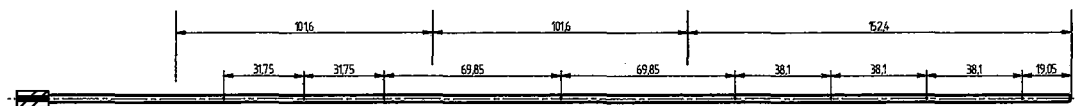
Figure 4.8: Schematic of the vapour temperature measurement probe with 8 embedded thermocouples.

50

is given in table 4.1. The heat pipes were closed with brass end caps. The thickness of the end caps was 6.35 mm, and were silver-soldered to the copper heat pipe. The assembly of the heat pipe was done by Acrolab Ltd., a heat pipe manufacturer in Windsor, Ontario. For the 4 wick-layer heat pipe, the vapour temperature in the heat pipe core was measured at 8 axial locations using a specially designed probe instrumented with T-type thermocouples. The probe consists of a 0.254 mm thick stainless steel tube with an outer diameter of 3.175 mm with thermocouples spaced along the probe as indicated in figure 4.8. An additional eight 0.508 mm T-type thermocouples were used to measure the wall temperature at the same axial locations as the vapour temperature measurements (three thermocouples were used to measure the wall temperature in the evaporator section, one thermocouple in the adiabatic section and four thermocouples in the condenser section). These thermocouples were mounted along 0.508 mm wide and 0.508 mm deep grooves along the surface of the heat pipe as shown in figure 4.7(b). The thermocouples leads ran directly off the evaporator end of the heat pipe. The thermocouples were soldered in place using Kester 50/50 Pb/Sn solder and the grooves filled with General Electric RTV 108 Silicone Rubber Adhesive Sealant to ensure that no cooling water escaped through the grooves at the condenser.

For the 3 wick-layer heat pipe, the vapour temperature in the heat pipe was measured at 4 axial locations using K-type thermocouples as described in Kempers et al. (2005). In this case, the thermocouples were inserted through holes drilled through the heat pipe wall and wick prior to charging. The thermocouple junctions were positioned at the center of the vapour core and silver soldered in place. They were spaced at distances of 50.8, 127, 228.6 and 304.8 mm from the evaporator end of the heat pipe. An additional 11 T-type thermocouples were used to measure the heat pipe wall temperature at axial locations of 12.7, 38.1, 63.5, 88.9, 127, 177.8, 215.9, 247.65, 279.4, 311.15 and 342.9 mm from the evaporator end (four thermocouples were used to measure the wall temperature in the evaporator section, two thermocouples in the adiabatic section and five thermocouples in the condenser section).

For the tests with the finned condenser, four heat pipes were manufactured with

Table 4.2: Fin number and spacing for different heat pipes.

Heat Pipe	Number of Fins	Fins Spacing (mm)
1a	0	--
1b	5	15
1c	7	10
1d	12	5

2 wick layers with fluid loading as shown in table 4.1. These heat pipes were 300 mm long with an outer diameter of 19.05 mm and wall thickness of 0.81 mm. Three heat pipes had different number of circular 0.81 mm thick copper fins with outer diameter of 50 mm while one heat pipe was left bare for comparison as shown in figure 4.9. The number of fins and fin spacing are summarized in table 4.2. The heat pipes were heated at one end over a length of 101.6 mm and cooled inside the wind tunnel at the other end over a length of 70 mm as shown schematically in figure 4.5. The surface temperature of these heat pipes were measured at 8 axial locations as illustrated in figure 4.9. Two thermocouples were used to measure the wall temperature in the evaporator section, one thermocouple in the adiabatic section and five thermocouples in the condenser section. The thermocouples used were 0.254mm T-type OMEGA self-adhesive thermocouples where the junction is secured between two pads of a high temperature fiberglass cloth and a high temperature electrically insulating polyimide film; and each pad is 19.05 mm wide, 25.4 mm long and 0.3 mm thick.
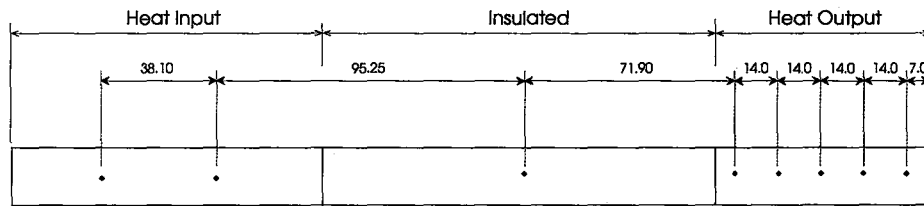
(a)
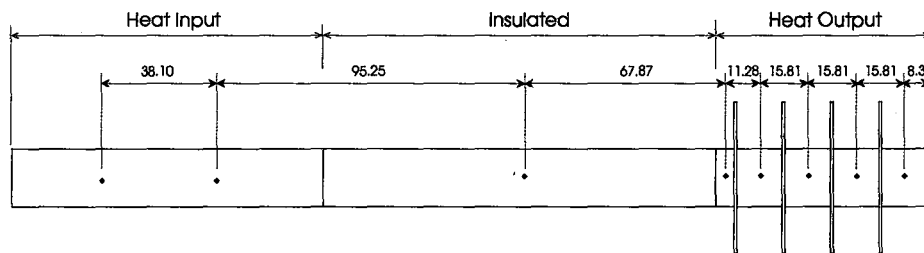
(b)
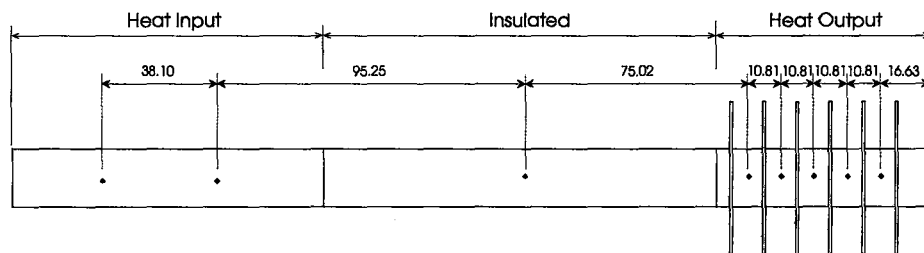
(c)
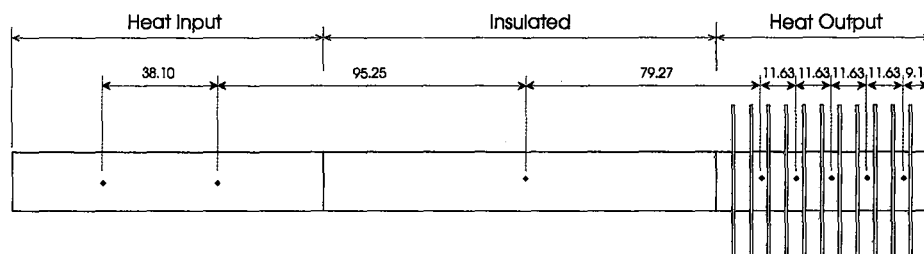
(d)

Figure 4.9: The locations of the surface thermocouples used for (a) bare heat pipe, (b) 5 fins, (c) 7 fins and (d) 12 fins.

4.3   Methodology and Data Reduction

All experiments were performed with the heat pipes in the horizontal direction to minimize the effect of gravity. The experimental procedure for the steady-state and transient tests are discussed in detail in this section. Also, the data analysis and the energy balance for the tests with the cooling water jacket are discussed here.

The tests with the cooling water jacket were performed at a constant condenser water flow rate of 5 L/min with a constant chiller water temperature set-point (sink temperature). The heat pipe was first allowed to reach steady-state with no heat input in the evaporator section. The heat input into the heaters (evaporator section) was increased in steps of 20 $Watts$ and the heat pipe was allowed to reach steady-state at each heat input level. Steady-state was defined such that the variation of the internal vapour temperatures was less than ± 0.1 $^\circ C$ over 100 seconds. The external and internal measurements were recorded at a sampling frequency of 60 Hz in a log file. The steady-state values were extracted from the log file by averaging the steady-state values over the last 60 seconds. The heat input was increased in incremental steps until a dry-out was observed in the heat pipe (where one thermocouple in the evaporator surface reads much higher values than the other thermocouples) or the maximum heat input for the rope heater (200 $Watts$) was reached.

The transient tests were performed at a constant condenser water flow rate of 5 L/min and constant chiller temperature set-point of 20 $^\circ C$. The heat pipe was allowed to reach steady-state with no heat input in the evaporator section. Then, the heater in the evaporator section was turned on using a specified function and to a specified value for every transient test. For the step function input, the heat input was maintained until the heat pipe reached steady-state and then the heat input was set to zero to capture the transient performance of the cool-down phase as well. Throughout the whole transient test, all the external and internal measurements were recorded at a sampling frequency of 60 Hz in a log file.

For the wind tunnel tests with the finned condenser, the air velocity in the test section was set to the desired level and the heat pipe was allowed to reach steady-state with no heat input in the evaporator section. The heat input into the heaters

(evaporator section) was increased in steps of 15 *Watts* and the surface temperatures were recorded once steady-state was reached. The heat input was then increased in incremental steps until a dry-out was observed in the heat pipe or the maximum heat input for the rope heater was reached. Steady-state in this case was defined such that the variation of the external surface condenser temperatures was less than ± 0.1 °C over 100 seconds.

The heat transferred to the heat pipe can be measured directly using the power transducer as shown in figure 4.1. Also, it can be measured through the heat transfer rate to the water loop in the condenser section in the tests with the cooling water jacket,

$$Q_{cond} = \dot{m}_w \, c_{p,w} \, (T_B - T_A) \tag{4.1}$$

where $\dot{m}_w$ is the water mass flow rate, $c_{p,w}$ is the water specific heat capacity, T_A and T_B are the inlet and outlet water temperature of the condenser. Corrections for the ambient heating to the water lines from the chiller to the condenser section and the viscous heating were made for the heat transfer in the condenser, which can be important at high water flow rates and low chiller temperature set-points. The effect of heat gained from the ambient and the viscous heating was estimated by operating the condenser without the heat pipe and measuring the condenser water temperature difference at different water flow rates and chiller set-points. In this case, an acrylic cylinder of 19.05 *mm* outer diameter and 177.8 *mm* long was used inside the water jacket to mimic the heat pipe.

The ambient heating is plotted against the temperature difference between the ambient and sink temperatures in figure 4.10. These measurements were obtained at minimum possible water flow rate of 2.6 *L/min* to minimize the effect of viscous heating. It is clear that there is some ambient heating, which varies linearly with the difference between the chiller set-point and the ambient temperature. A curve was fitted to the data to obtain a correlation between the ambient heat transfer rate and the temperature difference between the chiller and the ambient as follows,

$$Q_{amb} = 0.87136(T_{amb} - T_{chiller}) \tag{4.2}$$
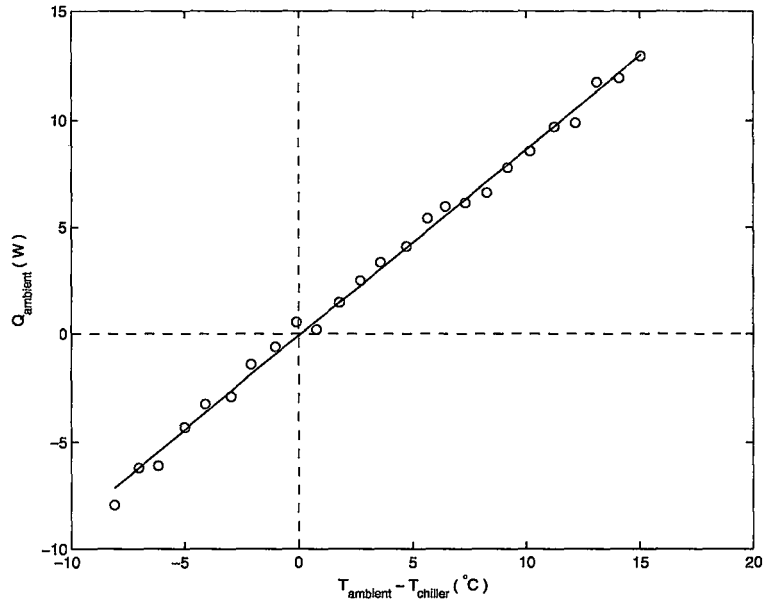
Figure 4.10: Variation of ambient heat transfer to the condenser water loop with temperature difference at flow rate of 2.6 L/min.
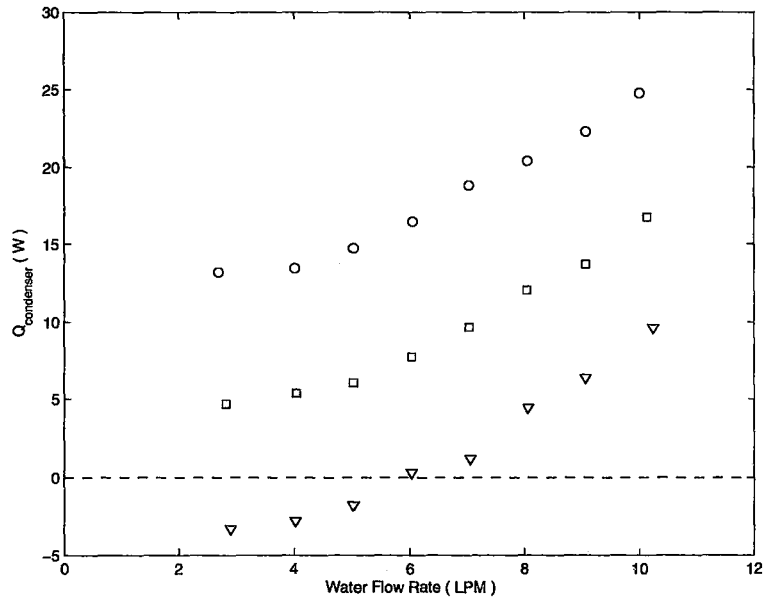
Figure 4.11: Variation of heat transfer to the condenser with water flow rate at chiller set-point of $\bigcirc$ $10°C$, $\square$ $20°C$ and $\triangledown$ $30°C$.

This correlation was used to estimate the ambient heating in the experiments performed for this study.

The effect of the water flow rate on the condenser heat transfer rate at different chiller set-points is shown in figure 4.11. The variation of the heat input with water flow rate has the same trend for different chiller set-points but with different offsets due to the ambient heating, indicating that the increase in power input at higher flow rates was not due to an increased heat transfer coefficient inside the tubing but viscous heating. This was verified by installing a Validyne differential pressure transducer with a 137.9 kPa diaphragm, across the cooling loop. The pressure drop across the system was measured for a number of different flow rates as shown in Kempers (2004). The viscous heating was estimated by subtracting the ambient heating from the data in figure 4.11 and shown in figure 4.12. There is reasonable collapse of the data for different cooling water temperatures. A curve was fitted to the data to obtain a correlation for the viscous heating as follows,

$$Q_{vis} = 0.16343(LPM)^2 - 0.41322(LPM) - 0.14334 \qquad (4.3)$$

This equation is valid for water flow rate in the range between 2.6 L/min and 10.4 L/min, and was used to estimate the viscous heating.

The heat transfer rate to the condenser can now be corrected to the ambient and viscous heating as,

$$Q_{out} = Q_{cond} - Q_{amb} - Q_{vis} \qquad (4.4)$$

where the values for $Q_{condenser}$, $Q_{ambient}$, and $Q_{viscous}$ can be calculated using equations 4.1, 4.2, and 4.3 respectively.

A heat balance between the input heat to the heat pipe and the corrected output heat transfer rate for a typical steady-state experiment at a condenser water flow rate of 5 L/min, a chiller water temperature set-point of 20 $°C$ and different heat inputs is shown in figure 4.13. It is clear that both the input and output heat transfer rates agreed within $\pm 5\%$. The uncertainty bars used in this figures are explained in detail in the following section.
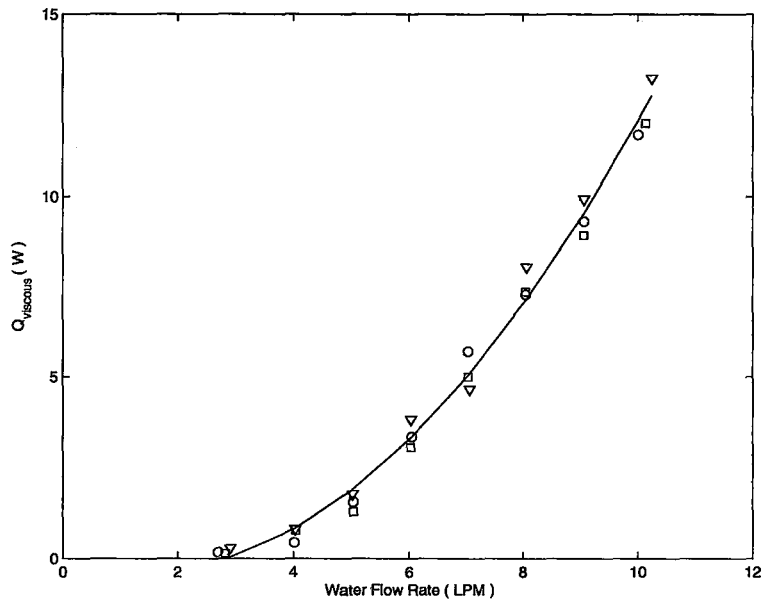
Figure 4.12: Corrected heat transfer to the condenser with water flow rate at chiller set-point of ◯ $10°C$, ☐ $20°C$ and ▽ $30°C$.
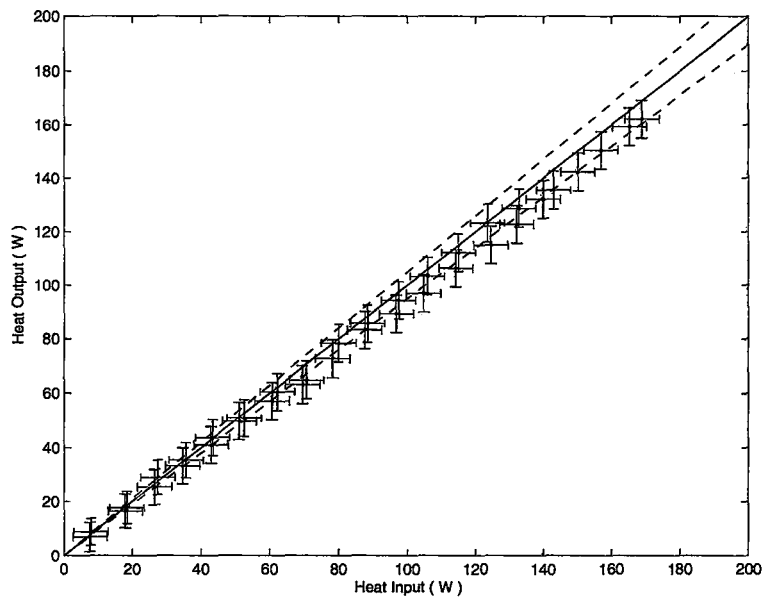
Figure 4.13: Corrected energy balance for heat pipe test facility.

4.4   Uncertainty Analysis

The source of uncertainties associated with the results in this study can be the uncertainty of the measured parameter due to the measuring device used or the uncertainty of the calculated parameter due to the error propagation from the measured parameters. A summary of the uncertainties associated with the measured parameters in the experiments for this study along with the measuring device used is given in Table 4.3.

The uncertainties associated with the calculated parameters were analyzed using the approach proposed by Kline and McClintock (1953). For a calculated variable Z that is dependent on a combination of n independent parameters A_i with known absolute uncertainties δA_i,

$$Z = f(A_1, A_2, A_3, \ldots, A_n) \tag{4.5}$$

the overall absolute uncertainty δZ of the calculated parameter Z can be computed using the error propagation equation as follow;

$$\delta Z = \left[\left(\frac{\partial Z}{\partial A_1} \delta A_1 \right)^2 + \left(\frac{\partial Z}{\partial A_2} \delta A_2 \right)^2 + \left(\frac{\partial Z}{\partial A_3} \delta A_3 \right)^2 + \cdots + \left(\frac{\partial Z}{\partial A_n} \delta A_n \right)^2 \right]^{1/2} \tag{4.6}$$

For example, assuming no uncertainty in the specific heat, the uncertainty of the condenser power output,

$$Q_{cond} = \dot{m}_w \, c_{p,w} \, \Delta T_w \tag{4.7}$$

can be calculated as,

$$\delta Q_{cond} = \left[(c_{p,w} \, \Delta T_w \, \delta \dot{m}_w)^2 + (\dot{m}_w \, c_{p,w} \, \delta \Delta T_w)^2 \right]^{1/2} \tag{4.8}$$

Table 4.3: Uncertainties associated with the measured parameters.

Parameter	Device Name	Uncertainty
Evaporator Power Input (Q_{in})	Ohio Semitronics PC5-011D AC Watt Transducer	$\pm 0.5\%$ of F.S.
Condenser Water Temperature (T_A, T_B)	4-Wire Platinum RTD & Omega DP251 Precision Thermometer	$\pm 0.014°$C
Condenser Water Flow Rate $(\dot{m}_w)$	Exact Flow Dual Rotor Turbine Flowmeter & Omron K3NR Rate Meter	$\pm 0.1\%$
External and Internal Temperatures (T_i)	Omega T-Type Thermocouple	$\pm 0.5°$C or 0.4%
Internal Temperatures (for the 3 wick layers heat pipe only)	Omega K-Type Thermocouple	$\pm 1.1°$C or 0.4%
Air pressure for the wind tunnel (P_A, P_B)	Dwyer MFG Inclined U-Tube Manometer	± 0.01 inch H_2O

or by dividing both sides by Q_{cond},

$$\frac{\delta Q_{cond}}{Q_{cond}} = \left[\left(\frac{\delta \dot{m}_w}{\dot{m}_w} \right)^2 + \left(\frac{\delta \Delta T_w}{\Delta T_w} \right)^2 \right]^{1/2} \qquad (4.9)$$

The relative uncertainty of the water mass flow rate was given by Exact Flow Dual Rotor Turbine Flowmeter and Omron K3NR Rate Meter to be $\pm 0.1\%$ while the absolute uncertainty of the temperature difference was calculated by a similar approach based on the measured absolute uncertainty of each RTD and was found to be $\pm 0.02 °C$ as shown in table 4.4. Substituting these values in the above equation, it is clear that the relative uncertainty of the condenser power output varies with ΔT_w. Using appropriate values, the relative uncertainty was calculated for different power outputs and it was found to be as high as $\pm 50\%$ for lower power range of $Q < 20W$ and about $\pm 5\%$ for higher power levels of $Q > 120W$ as shown in table 4.4.

Similar analysis were done for the other calculated quantities. A summary of the uncertainties associated with the calculations required in these experiments is given in Table 4.4.

Table 4.4: Uncertainties associated with the calculated parameters.

Parameter	Equation	Uncertainty
Condenser Water Temperature Difference	$\Delta T_w = T_B - T_A$	$\pm 0.02°$C
Condenser Power Output (Q_{cond})	$Q_{cond} = \dot{m}_w\, c_{p,w}\, \Delta T_w$	$\pm 50\%$ for $Q<20$W $\pm 20\%$ for $20<Q<70$W $\pm 10\%$ for $70<Q<120$W $\pm 5\%$ for $Q>120$W
Evaporator Average Surface Temperature (T_e)	$T_e = \left(\sum\limits_{i=1}^{3} T_i\right)/3$	$\pm 0.29°$C
Condenser Average Surface Temperature (T_c)	$T_c = \left(\sum\limits_{i=1}^{4} T_i\right)/4$	$\pm 0.25°$C
Overall Temperature Difference (ΔT)	$\Delta T = T_e - T_c$	$\pm 0.38°$C
Overall Thermal Resistance (R)	$R = \Delta T/Q_{in}$	$\pm 30\%$ for $Q<20$W $\pm 10\%$ for $20<Q<70$W $\pm 5\%$ for $Q>70$W
Pressure Drop (ΔP)	$\Delta P = P_B - P_A$	± 4.97 Pa
Air Velocity (v)	$v = \sqrt{2\Delta P/\rho_a}$	$\pm 15\%$ for $v<6$m/s $\pm 2\%$ for $6<v<14$m/s $\pm 0.5\%$ for $v>14$m/s

CHAPTER 5
RESULTS AND DISCUSSION

In this chapter, the experimental results are discussed and compared to the model simulations for the steady and transient performance of the heat pipes for the different condenser boundary conditions. The first section discusses how the amount of non-condensable gases were determined and the effect of theses gases on the steady and transient performance. The effect of axial conduction in the wall and wick is discussed in detail next, including the effect of the wick thickness on the heat pipe performance. The effect of the surrounding media on the transient performance of heat pipes are presented next. The last section details the performance of the finned condenser heat pipes from the wind tunnel experiments.

5.1 Effect of Non-Condensable Gases

The amount of non-condensable gases in the heat pipe was determined by a set of steady state experiments where the heat input was increased in steps of 20 *Watts* while maintaining a constant sink temperature. These experiments were performed with the water jacket condenser. The axial surface and vapour temperature distributions for the 3 wick-layer heat pipe for a sink temperature of $20°C$ is shown in figure 5.1. The surface temperature distribution shows that there is no sharp temperature demarcation between the different regions of the heat pipe (i.e. the evaporator, adiabatic and condenser sections). This indicates that axial conduction along the wall and wick may be important, which is discussed in detail in the next section.

The surface temperature distribution in the condenser section clearly shows the non-condensable gases present in the condenser. At low heat fluxes, a significant portion of the condenser is occupied by the non-condensable gases, as evident by the temperature being close to the sink temperature. As the heat flux is increased, the

63

Figure 5.1: Steady axial surface and vapour temperature distribution of 3 wick-layer heat pipe for $T_{c,inf} = 20°C$ and heat input of $+$ $20W$, $\circ$ $40W$, $\square$ $60W$, $\diamond$ $80W$, $\triangle$ $100W$, ∇ $120W$, $\triangleright$ $140W$ and $\triangleleft$ $160W$. (Solid lines represent the model predictions).

Figure 5.2: Change in heat transfer rate with temperature difference for 3 wick-layer heat pipe at sink temperature of $\triangleright$ $12°C$, $\circ$ $20°C$ and $\triangleleft$ $35°C$. (Solid lines represent the model predictions).

gases are compressed to the condenser end activating a larger part of the condenser and the temperature in this portion begins to increase, while the temperature towards the condenser end cap is still close to the sink temperature. This is more clearly seen in the internal vapour temperature distribution, where the temperature in parts of the condenser that is occupied by the non-condensable gases have lower values similar to the condenser surface temperature. At the higher heat transfer rates, a greater length of the condenser becomes active and the vapour temperature increases to that of the adiabatic section.

The presence of the non-condensable gases causes a non-linear performance of the heat pipe, where a higher temperature difference is required at low heat fluxes due to the non-condensable gases occupying a relatively large part of the condenser. As the heat flux increases, the gases are further compressed and the thermal resistance decreases. The heat transfer rate as a function of the total temperature difference between the average evaporator surface and the sink for three different sink temperatures are shown in figure 5.2. The performance of the heat pipe strongly depends on the sink temperature, where there is a non-linearity at low heat transfer rates as explained above, and similar to that reported by ?. As the sink temperature increases, the non-linearity in the heat pipe performance decreases since the operating temperature of the heat pipe is increased and the non-condensable gases are compressed more towards the condenser end cap.

The amount of non-condensable gas in the heat pipe was estimated by assuming it was air with a gas constant of 287 J/kgK. The mass was estimated from the vapour-gas front from the vapour temperature measurements in figure 5.1. The amount of non-condensable gases was varied in the model until the inactive condenser length matched the experimental vapour temperature measurements at the condenser. It was found that a non-condensable gas mass of 3.5×10^{-7} kg fit the experimental data for this case.

The experimental data for the steady state axial surface and vapour temperature distributions of the 3 wick-layer heat pipe are compared to the model predictions in figure 5.1, while the overall performance of the heat pipe at different sink temperatures

are compared to the model predictions in figure 5.2. There is good agreement between the experimental data and model predictions for the overall heat pipe performance at different sink temperatures, indicating that the mass of non-condensable gases estimated from the vapour measurement are fairly accurate. The sensitivity of the model predictions to a change in the mass of the non-condensable gas by $\pm 10\%$ is also shown in figure 5.2. An error of $\pm 10\%$ in estimating the amount of the non-condensable gases had only a very small effect on the predicted overall performance of the heat pipe, especially at high heat fluxes. For the same temperature difference, the error in estimating the mass of the non-condensable gases by $\pm 10\%$ would introduce an error of about $\pm 15\%$ and $\pm 2\%$ at lower and higher heat fluxes, respectively.

The same procedure was used to determine the amount of non-condensable gas for the 4 wick-layer heat pipe. In this case, the mass of non-condensable gas was 14.5×10^{-7} kg and a comparison between the model results and the experimental data are shown in figures 5.3 and 5.4. The difference in the mass of the non-condensable gas entrapped in the 3 and 4 wick-layer heat pipes can be attributed to the different internal instrumentation used in the heat pipes as discussed in the previous chapter. The 3 wick-layer heat pipe contained four internal thermocouples placed along the vapour core at different axial locations and soldered to the heat pipe wall, while the 4 wick-layer heat pipe contained a stainless steel thermocouple probe (containing eight thermocouples at different axial locations) that was embedded in the vapour core and connected to the evaporator end cap using a vacuum seal compression fitting. The compression fitting was believed to introduce a higher non-condensable gas content in the 4 wick-layer heat pipe. Also, the stainless steel sheath of the vapour probe could have caused some out-gasing over a period of time.

The increased number of thermocouples in the vapour core of the 4 wick-layer heat pipe, however, provides a more accurate estimate of the mass of the non-condensable gas as it allows a better comparison of the predicted inactive condenser portion to the vapour temperature measurements as illustrated in figure 5.3. The first thermocouple from the evaporator end reads higher values when compared to the other thermocouples in the vapour core, and is likely due to the conduction effects
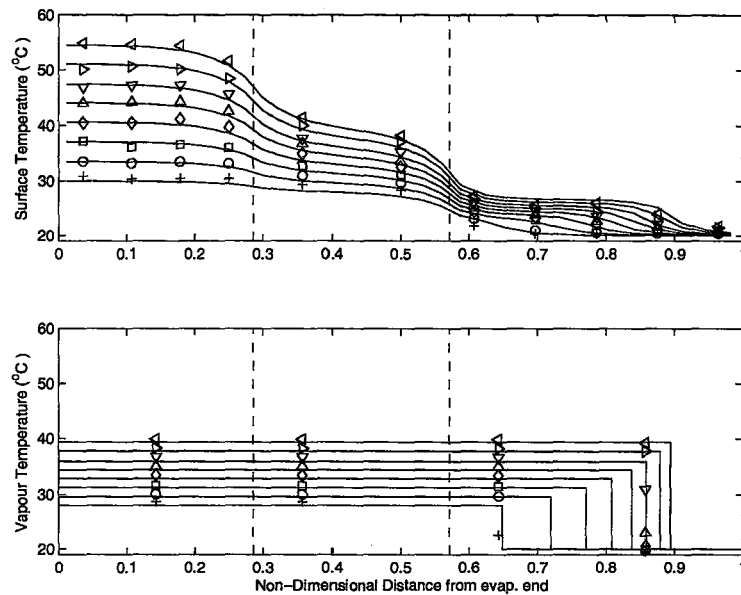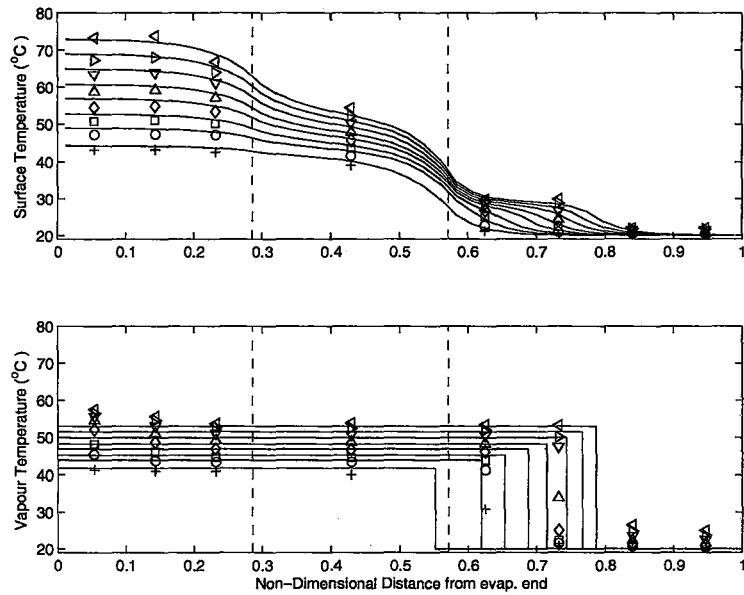
Figure 5.3: Steady axial surface and vapour temperature distribution of 4 wick-layer heat pipe for $T_{c,inf} = 20°C$ and heat input of $+$ 20W, $\bigcirc$ 40W, $\square$ 60W, $\lozenge$ 80W, $\triangle$ 100W, ∇ 120W, $\triangleright$ 140W and $\triangleleft$ 160W. (Solid lines represent the model predictions).
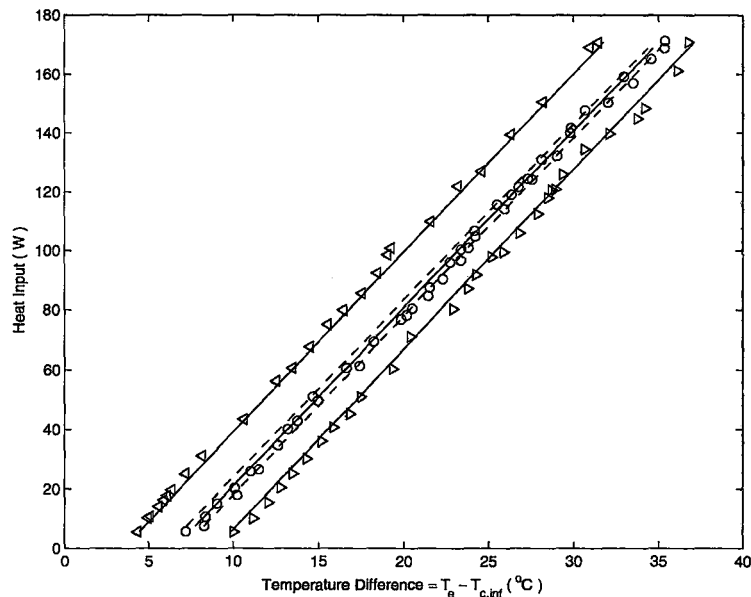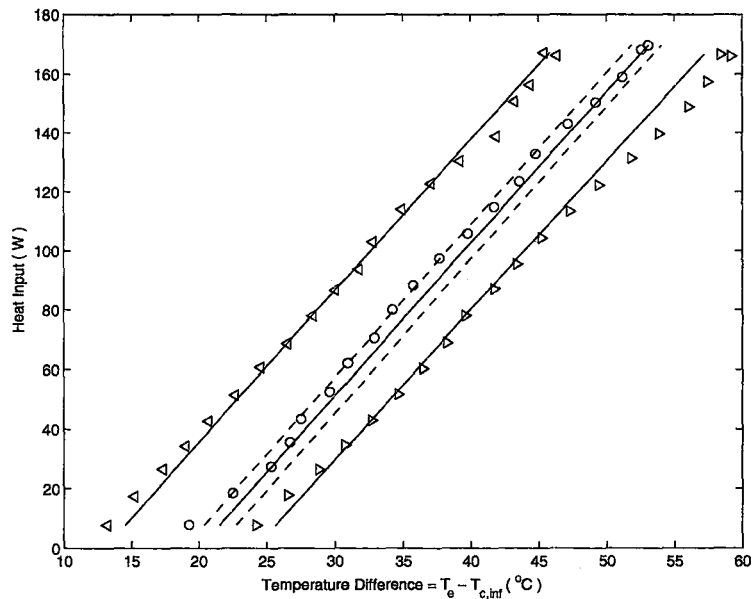

Figure 5.4: Change in heat transfer rate with temperature difference for 4 wick-layer heat pipe at sink temperature of $\triangleright$ 12°C, $\bigcirc$ 20°C and $\triangleleft$ 35°C. (Solid lines represent the model predictions).

67

in the stainless steel probe from the evaporator end cap. The thermocouples in the condenser section clearly shows that a part of the condenser is initially blocked where the thermocouples read lower values similar to the condenser surface temperature. At higher heat transfer rates, a greater length of the condenser becomes active and is reflected in the thermocouple readings where it approaches values comparable to the rest of the vapour core. The internal vapour temperature measurements indicate that the flat front model for the non-condensable gas is reasonable. However, some diffusion effects between the vapour and the gas can be noticed in the thermocouple readings before and after the vapour-gas interface as shown in figure 5.3.

To understand the effect of the non-condensable gases on the transient performance, experiments were performed using the 3 wick-layer heat pipe for a step uniform heat input of 100 W and constant sink temperature of 20 $°C$. The experimental axial temperature distributions with time are shown in figure 5.5. At small times (e.g. 100 seconds), the condenser is almost completely occupied by the non-condensable gases. As time passes, the heat pipe operating temperature increases and the gases are further compressed to the condenser end activating a larger portion of the condenser. The experimental results were compared to the model prediction for the same conditions along with an additional simulation where the non-condensable gases were excluded and are shown in figure 5.5. The axial temperature distributions at three different times are compared to the simulation results in figure 5.5. The transient of the average temperatures of the evaporator, condenser and vapour are compared in figure 5.6, while the non-dimensional vapour temperature responses are compared in figure 5.7.

There is good agreement between the predicted and measured axial wall temperature distributions at different times during the heat-up phase, as seen in figure 5.5. The evaporator wall temperature is nearly uniform as expected while the condenser wall temperature drops off towards the end due to the presence of non-condensable gases at the far end of the condenser. As the vapour temperature increases with time, the condenser wall temperature becomes more uniform as the gases are compressed with an increase in the vapor pressure. However, the simulation result of the case
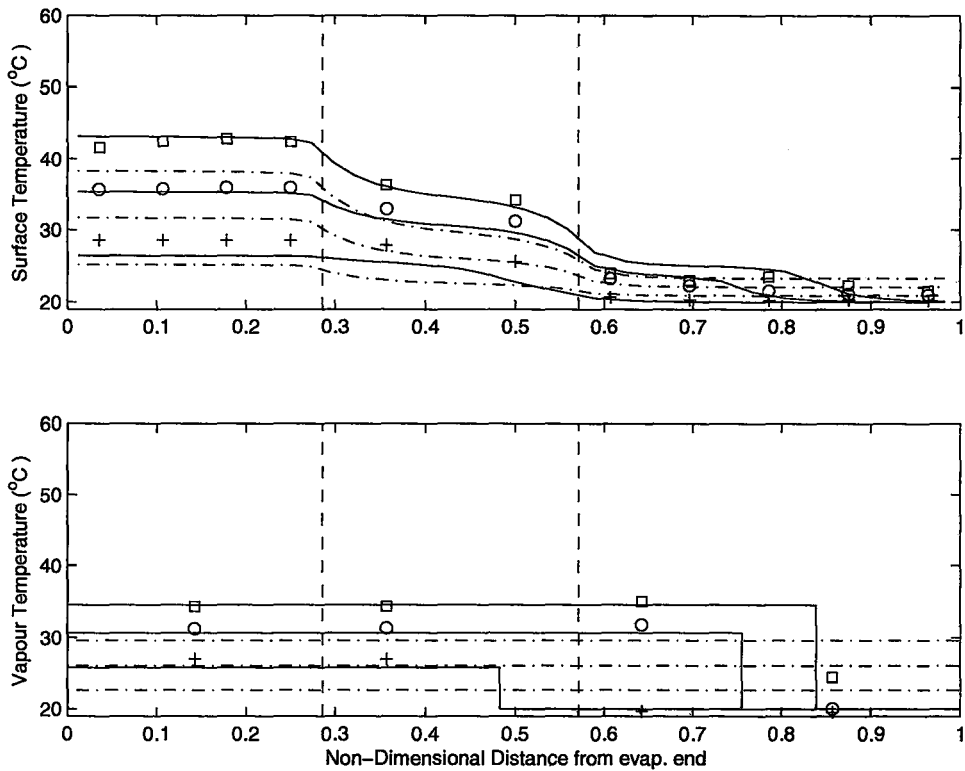
Figure 5.5: Transient axial surface and vapour temperature distribution of 3 wick-layer heat pipe for $T_{c,inf} = 20°C$ and heat input of $100W$ for the cases where —— the effects of both axial conduction and non-condensable gases are considered and – · – only the effect of axial conduction was considered but there was no non-condensable gases present, at times + $100s$, ○ $300s$ and □ $2000s$.
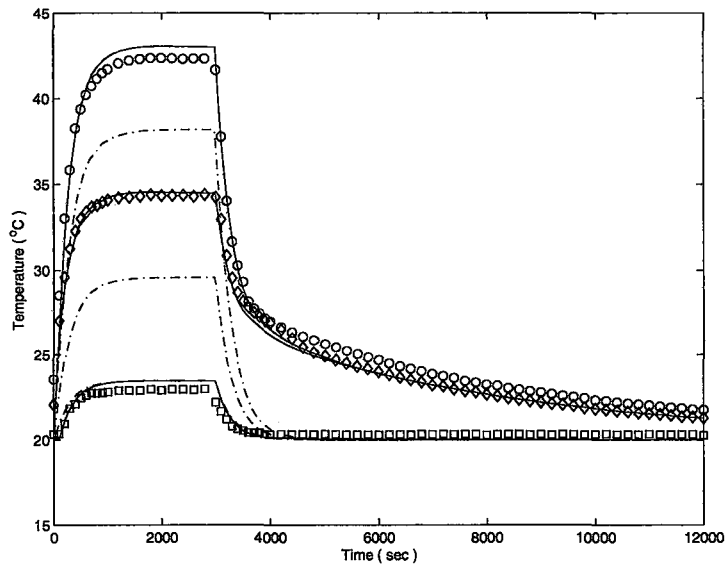
Figure 5.6: Transient average temperatures ($\bigcirc$ T_e, $\Diamond$ T_v and $\square$ T_c) of 3 wick-layer heat pipe for $T_{c,inf} = 20°C$ and heat input of $100W$ for the cases where —— the effects of both axial conduction and non-condensable gases are considered and $- \cdot -$ only the effect of axial conduction was considered but there was no non-condensable gases present.
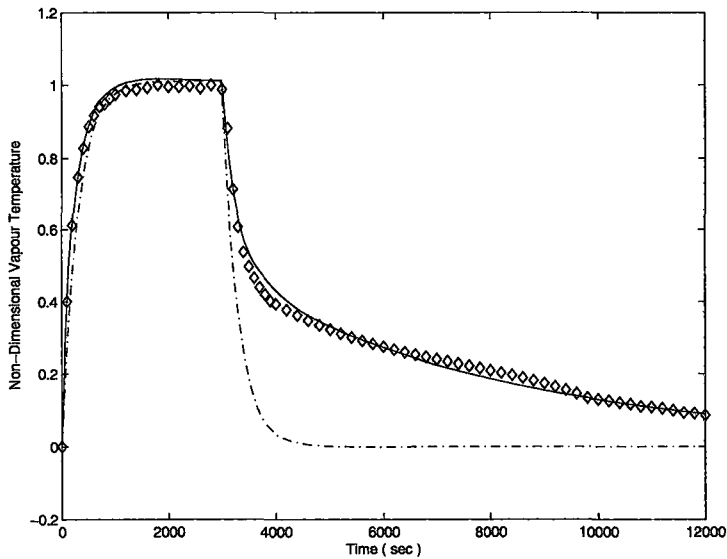
Figure 5.7: Transient non-dimensional vapour temperature of 3 wick-layer heat pipe for $T_{c,inf} = 20°C$ and heat input of $100W$ for the cases where —— the effects of both axial conduction and non-condensable gases are considered and $- \cdot -$ only the effect of axial conduction was considered but there was no non-condensable gases present.

70

where the non-condensable gases were excluded shows a uniform vapour and surface condenser temperature with time. The presence of even a very small amount of non-condensable gases increases the overall resistance of the heat pipe and consequently results in a higher temperature difference for a given heat flux as shown in figures 5.5 and 5.6.

The heat-up phase for the case that includes the non-condensable gases can be divided into two time domains; the first one (the first 200 seconds) is characterized by a rapid increase of the vapour temperature since the condenser is inactive and predominantly occupied by the non-condensable gases (figure 5.7). In this case the vapour heats up quickly because the heat transfer to the condenser by the vapour is very small. The second phase is marked by a lower rate of temperature increase as the condenser progressively becomes active and heat is transferred from the vapour to the condenser water jacket. For the case where the non-condensable gases are neglected, there is a slower increase in the vapour temperature of the heat pipe as the entire condenser is active at all times. The time constant from the experimental data (defined as the time required for the vapour temperature to reach 63.2% of the total rise) for this case was approximately 210 seconds, whereas the time constant from the model was 205 seconds. This difference could be due to the heaters and the insulation surrounding the evaporator and the adiabatic sections that were not included in the model. These have a time constant which would result in a slower transient response for the heat pipe.

The cool-down phase can also be divided into two time domains; the first one (the first 1000 seconds) is characterized by a high rate of temperature decrease where part of the condenser is still active, while the second one has a much lower rate of temperature decrease indicating that the condenser is fully occupied by the non-condensable gases and the heat is transferred mainly by axial conduction.

The heat-up time constant increased to 281 seconds from 210 seconds when the non-condensable gases were excluded from the simulation. For the cool-down phase, the non-condensable gases slows down the cooling rate of the heat pipe compared to the case with no non-condensable gases as shown in figure 5.7.

The variation in the ratio of the inactive to the total condenser length is plotted against the difference between the vapour and the sink temperature for a 3 wick-layer heat pipe with 3.5×10^{-7} kg of non-condensable gases at different sink temperatures in figure 5.8. For a given sink temperature, a greater portion of the condenser length becomes active as the difference between the vapour and the sink temperature increases. For the same temperature difference, the inactive region becomes very small at higher sink temperatures due to the higher operating temperature and hence the vapour pressure. Hence, it is important to note that the volume occupied by the non-condensable gases depends on both the temperature difference and the sink temperature. At high operating temperatures, the effect of the non-condensable gases is very small; however, the gases will affect the transient response as shown previously.

In order to estimate under what conditions the non-condensable gases will influence the performance of the heat pipe, the locus of points corresponding to a 90% active condenser length is plotted in figure 5.9. In this figure, the difference between the vapour and the sink temperature is plotted against the sink temperatures at which the blockage ratio is 10% for a 3 wick-layer heat pipe with 3.5×10^{-7} kg of non-condensable gases. The area above the curve represents the operating range where the non-condensable gases occupy less that 10% of the condenser length. The effect of the mass of the non-condensable gases on the operating range is shown in figure 5.10. As the mass of the non-condensable gases increases, the curve shifts upwards increasing the area under the curve where the effect of the non-condensable gases are significant. For example, at a sink temperature of $50°C$, if the amount of non-condensable gases is doubled, the minimum operating temperature difference between the vapour and the sink where the the condenser blockage ratio is less than or equal 10% would increase from $15°C$ to $25°C$. This decreases as the sink temperature increases and the non-condensable gases become less important.
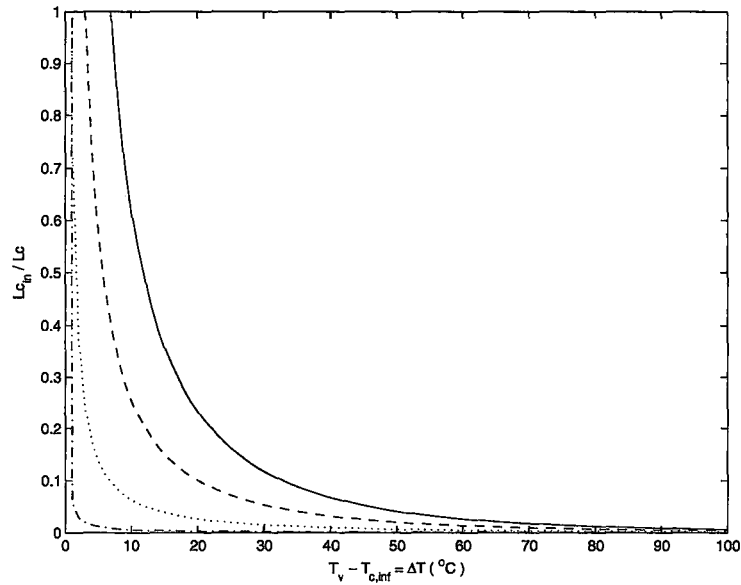
Figure 5.8: Change of the ratio of the inactive condenser length to the total condenser length with the difference between the vapour and the sink temperature for 3.5×10^{-7} kg of non-condensable gases at sink temperature of —— $20°C$, – – – $40°C$, $\cdots\cdots$ $80°C$ and – $\cdot$ – $200°C$.
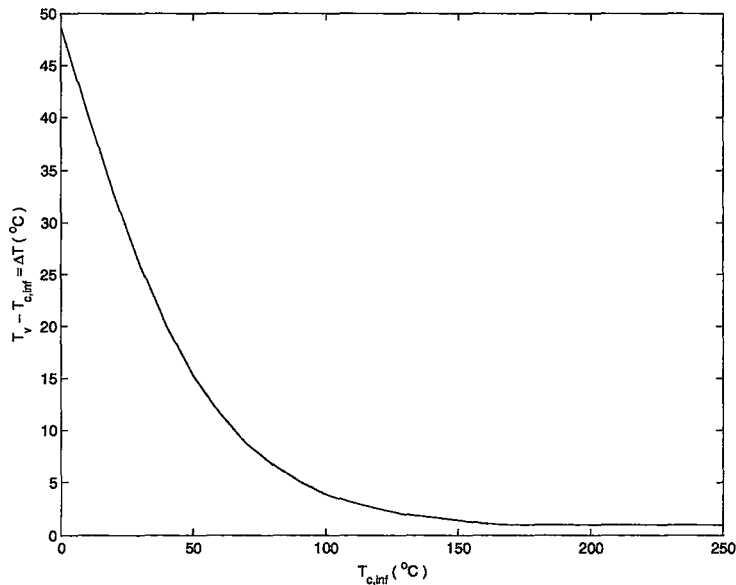
Figure 5.9: The effect of sink temperature on the difference between the vapour and the sink temperature at which 90% of the condenser length is active for 3.5×10^{-7} kg of non-condensable gases.
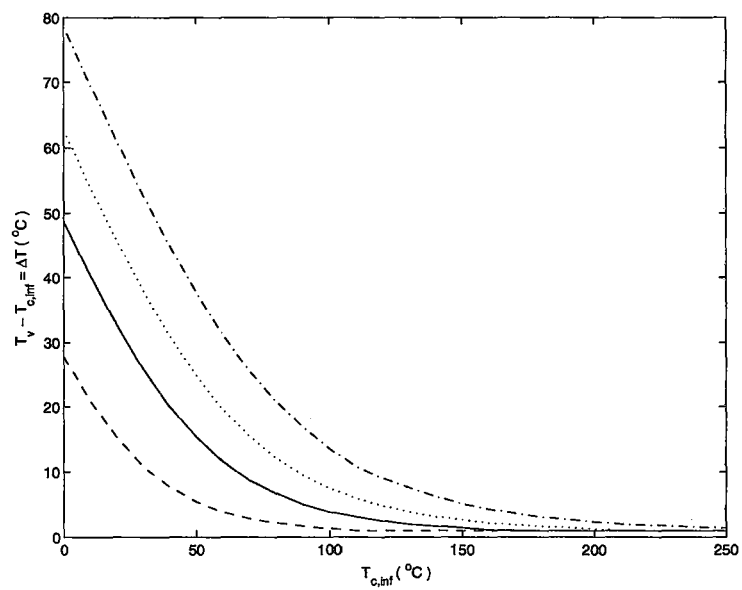
Figure 5.10: The effect of sink temperature on the difference between the vapour and the sink temperature at which 90% of the condenser length is active for − − − 1.0×10^{-7} kg, —— 3.5×10^{-7} kg, $\cdots\cdots$ 7.0×10^{-7} kg and − · − 14.0×10^{-7} kg of non-condensable gases.

5.2   Effect of Axial Heat Conduction

Previous network models for heat pipes usually neglect the axial conduction in the heat pipe wall and wick. In this section, the importance of axial heat conduction is evaluated from the experimental and numerical results. The experimental axial variation of temperature with time for the 3 wick-layer heat pipe is compared to the model predictions considering the axial conduction in the wall and wick, for the case of a step uniform heat input of 100 W and constant sink temperature of 20 $^{\circ}C$ in figure 5.11. The experimental results clearly show that there is no step change in the temperature distribution at the different heat pipe sections (i.e. evaporator, adiabatic and condenser). It is also clear that the temperature distribution is not uniform in the adiabatic section and there is some temperature degradation indicating an axial heat conduction process. The surface and vapour temperature distributions suggest that the effective lengths of the evaporator and condenser sections are longer than the actual heated and cooled lengths due to the axial heat conduction in the wall and wick structure. There is good agreement between the predicted and measured axial wall temperature distributions at different times during the heat-up phase, as seen in figure 5.11.

The corresponding transient average temperatures of the evaporator, condenser and vapour are shown in figure 5.12. For the case where the non-condensable gases occupy a significant portion of the condenser, the axial heat conduction becomes more important as this becomes the primary mode of heat transfer to the condenser. To further understand the effect of axial conduction, an additional simulation was performed where the axial conduction was neglected while retaining the non-condensable gases. The axial surface temperature distribution at different times for this case is compared to the full simulation in figure 5.11. Neglecting axial heat conduction results in sudden changes in the surface temperature between the different regions of the heat pipe as expected.

The transient of the average temperatures are compared in figure 5.12, while the non-dimensional vapour temperatures are compared in figure 5.13. The axial heat conduction has only a small effect on the response in the heat-up phase; however,

75

Figure 5.11: Transient axial surface and vapour temperature distribution of 3 wick-layer heat pipe for $T_{c,inf} = 20°C$ and heat input of $100W$ for the cases where —— the effects of both axial conduction and non-condensable gases are considered and – – – non-condensable gases were included but the effect of axial conduction neglected, at times + $100s$, O $300s$ and □ $2000s$.
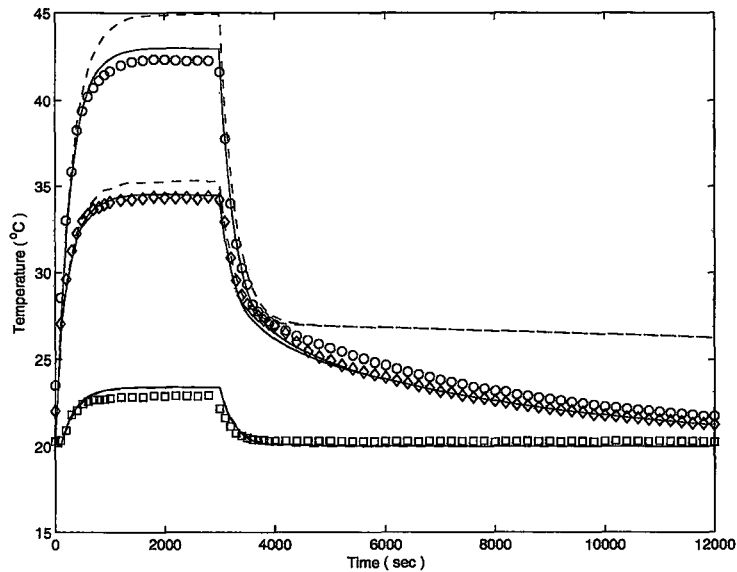
Figure 5.12: Transient average temperatures ($\circ$ T_e, $\diamond$ T_v and $\square$ T_c) of 3 wick-layer heat pipe for $T_{c,inf} = 20°C$ and heat input of $100W$ for the cases where ——— the effects of both axial conduction and non-condensable gases are considered and – – – non-condensable gases were included but the effect of axial conduction neglected.
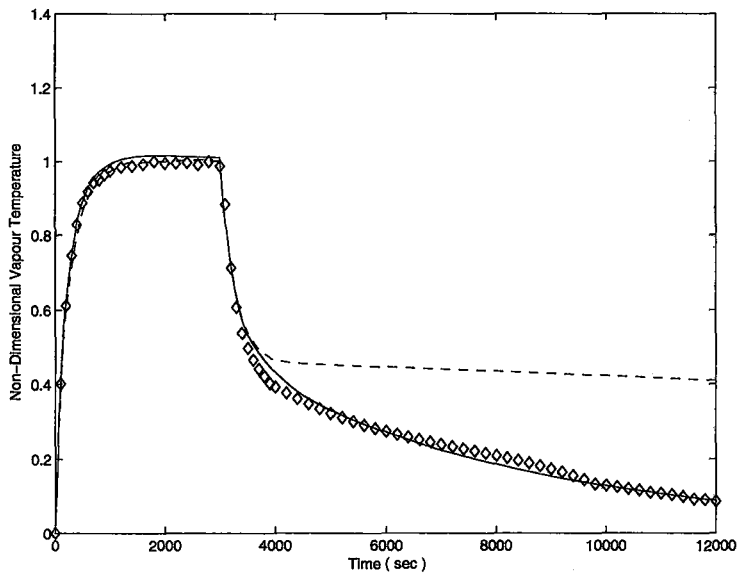
Figure 5.13: Transient non-dimensional vapour temperature of 3 wick-layer heat pipe for $T_{c,inf} = 20°C$ and heat input of $100W$ for the cases where ——— the effects of both axial conduction and non-condensable gases are considered and – – – non-condensable gases were included but the effect of axial conduction neglected.

at steady-state the evaporator temperature is lower when axial heat conduction is considered indicating a lower total resistance. For the cool-down phase, the axial heat conduction results in a much faster response, especially after about 1000 seconds from the start of the cool-down. This is when the condenser is almost occupied by the non-condensable gases and the axial conduction allow heat transfer to the condenser. For the other case with no axial heat conduction, there is almost no cooling after the non-condensable gases occupy the condenser.

Neglecting the axial conduction through the pipe wall and the wick structure increases the overall thermal resistance of the heat pipe, and causes a higher temperature difference for the same heat input. For example, the evaporator surface temperature reached $43°C$ when axial conduction was considered, while it reached $45°C$ with no axial conduction, resulting in an increase of about 10% for the total heat pipe thermal resistance. The axial conduction does not have a great influence on the time response during the heat-up phase, where the heat-up time constant was slightly increased to 226 seconds from 210 seconds. During the cool-down phase, however, the axial conduction has a significant effect as shown in figure 5.13, particulary when the condenser is inactive due to the accumulation of the non-condensable gases. In this case, the heat transfer due to the axial conduction allows a cooling down mechanism for the condenser.

Since the wick structure is the dominant thermal resistance in the heat pipe, it is useful to determine how this affects the overall transient performance. Transient experiments were performed using the 3 and 4 wick-layer heat pipes under the same boundary conditions of a step uniform heat input of 100 W and constant sink temperature of 20 $°C$. The axial surface and vapour temperature distributions at different times in the heat-up phase are compared to the model predictions using the amount of non-condensable gases specified for these heat pipes in figures 5.14 and 5.15. It is clear that the larger amount of non-condensable gases in the 4 wick-layer heat pipe blocks the condenser length over the first 400 seconds as the condenser surface temperature is clearly very close to the sink temperature over this period as shown in figure 5.14. This causes a slightly faster response in the heat-up phase and

slower response in the cool-down phase as shown in the previous section.

The transient average evaporator surface, active vapour and condenser surface temperatures for the two heat pipes are shown in figure 5.16. The transient vapour temperature non-dimensionalized by its steady state value is shown in figure 5.17 for the two heat pipes to allow a better comparison of the time constants. The time constant for the 4 wick-layer heat pipe is 292 seconds from the experiments and 282 seconds from the model predictions, while for the 3 wick-layer heat pipe is 210 seconds from the experiments and 205 seconds from the model predictions. Noting that the wick resistance of the 4 wick layers heat pipe is 40% more than that of the 3 wick layers heat pipe, the response of the 4 wick-layer heat pipe is still slower than the 3 wick-layer one as shown in figures 5.16 and 5.17.

It is clear that using a larger number of wick layers increases the overall resistance of the heat pipe, and consequently increases the temperature difference between the evaporator and condenser ends at steady state. At the same time, it causes a slower response for both heating and cooling due to an increase in the capacitance and resistance of the wick structure inside the heat pipe.

While the wick structure is the dominant thermal resistance in the steady-state operation of the heat pipe, the current results shows that it is also the most dominant component in the heat pipe that influence the transient performance. As noted before, the vapour flow has a faster transient response than the pipe wall and the wick structure. The wick structure has a much higher resistance (the wall resistance is about 0.6% of the wick resistance) and a slightly lower capacitance (the wick capacitance is about 60% of the wall capacitance) compared to a thick heat pipe wall (the wick thickness of the 3 wick-layer heat pipe is about 40% of the wall thickness used, while the wick thickness of the 4 wick-layer heat pipe is about 53% of the wall thickness used). The wick structure has a greater influence on the transient performance than the amount of non-condensable gases entrapped in the heat pipe, especially at higher operating temperatures where the effect of non-condensable gases is negligible.

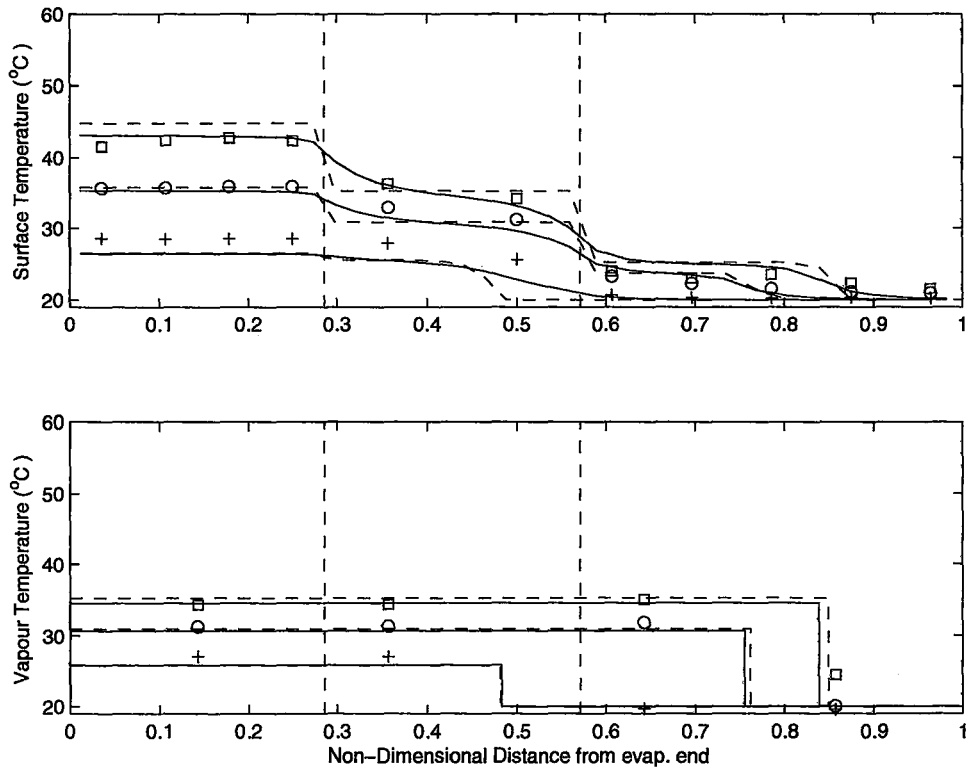Figure 5.14: Comparison of the predicted and measured transient axial surface and vapour temperature distribution of 4 wick-layer heat pipe for $T_{c,inf} = 20°C$ and heat input of $100W$ at times $+$ $200s$, $\circ$ $400s$ and $\square$ $1000s$.

Figure 5.15: Comparison of the predicted and measured transient axial surface and vapour temperature distribution of 3 wick-layer heat pipe for $T_{c,inf} = 20°C$ and heat input of $100W$ at times $+$ $200s$, $\circ$ $400s$ and $\square$ $1000s$.

Figure 5.16: Comparison of the transient average temperatures for $T_{c,inf} = 20°C$ and heat input of $100W$ of 4 wick-layer heat pipe ($\circ$ T_e, $\diamond$ T_v and $\square$ T_c) and 3 wick-layer heat pipe ($+$ T_e, $*$ T_v and $\times$ T_c). (Solid lines represent the model predictions).

Figure 5.17: Comparison of the non-dimensional vapour temperature for $T_{c,inf} = 20°C$ and heat input of $100W$ of $\diamond$ 4 wick-layer heat pipe and $*$ 3 wick-layer heat pipe. (Solid lines represent the model predictions).

5.3   Effect of Surrounding Media

The relatively long time constant for the present geometry can be attributed to the evaporator heating block. The effect of the evaporator block was evaluated through three transient experiments where the heat was applied to the heat pipe through a big block (figure 4.3(a)), a small block (figure 4.3(b)), and directly to the heat pipe. These tests were performed for the 4 wick-layer heat pipe for a step uniform heat input of 100 W and constant sink temperature of 20 $°C$.

The axial surface and vapour temperature distributions at different times in the heat-up phase are shown in figures 5.18, 5.19 and 5.20 for the three cases along with the model predictions. The amount of non-condensable gases previously determined for this heat pipe was used in these simulations. These gases take a longer time to activate a part of the condenser for the big block case compared to the small block and no block cases. The diffusion effects at the vapour-gas interface is more clear in the vapour temperature distributions in these figures. The variation in the temperature can be partially attributed to the conduction in the vapour probe that was used in this heat pipe.

The transient average evaporator surface, active vapour core and condenser surface temperatures for the three cases are compared in figure 5.21. The transient non-dimensionalized vapour temperature is shown in figure 5.22 for the three cases to allow a better comparison of the time constants. The time constant with the big block, small block and no block are 292, 34 and 20 seconds from the experiments while the model predictions are 282, 25 and 15 seconds. The difference between the predicted and measured time constant is likely due to the heaters and the insulation layers surrounding the evaporator and the adiabatic sections that were not included in the model. These have a time constant which would result in a slower transient response for the heat pipe, especially for the case where no evaporator block was used.

Noting that the total capacitance of the heat pipe is 8% and 56% of the capacitance of the big and small blocks respectively, the results show that the time response of the heat pipe itself is small and the block acts a a limiting factor on the heat transfer from the heater source to the heat pipe surface. These results clearly
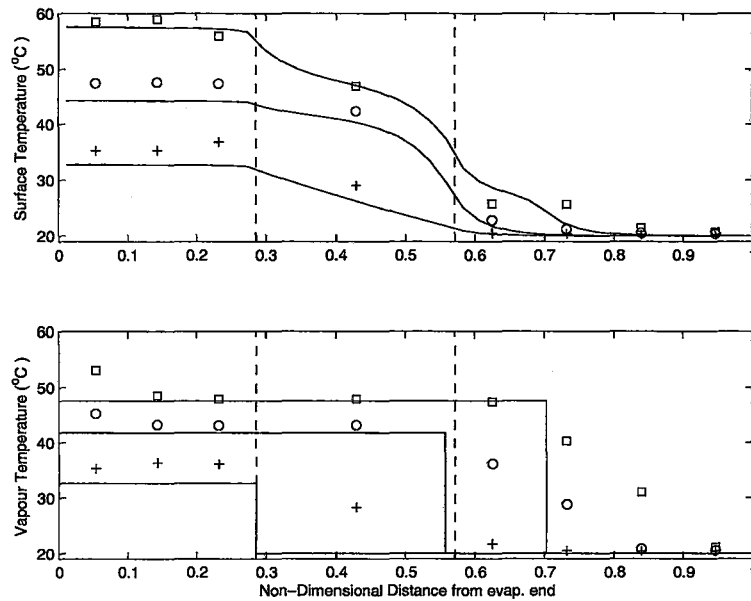
Figure 5.18: Comparison of the predicted and measured transient axial surface and vapour temperature distribution of 4 wick-layer heat pipe using the big block for $T_{c,inf} = 20°C$ and heat input of $100W$ at times $+$ $200s$, O $400s$ and □ $1000s$.
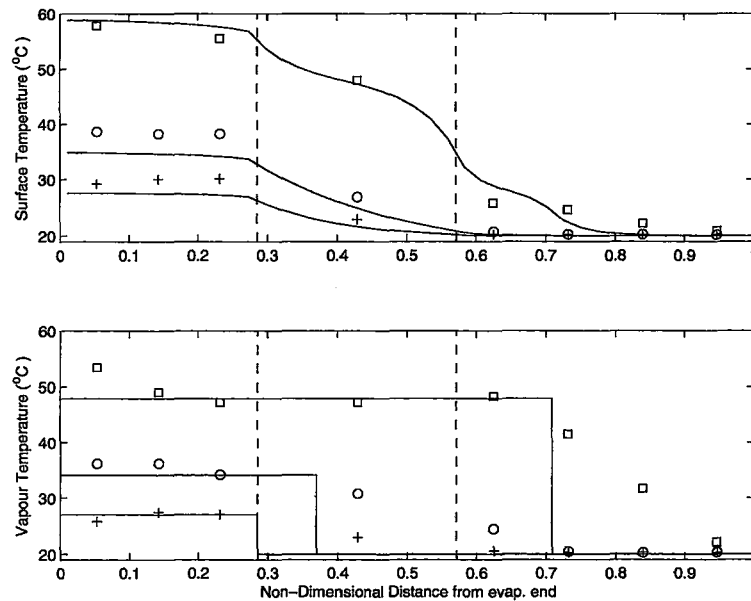
Figure 5.19: Comparison of the predicted and measured transient axial surface and vapour temperature distribution of 4 wick-layer heat pipe using the small block for $T_{c,inf} = 20°C$ and heat input of $100W$ at times $+$ $20s$, O $40s$ and □ $200s$.
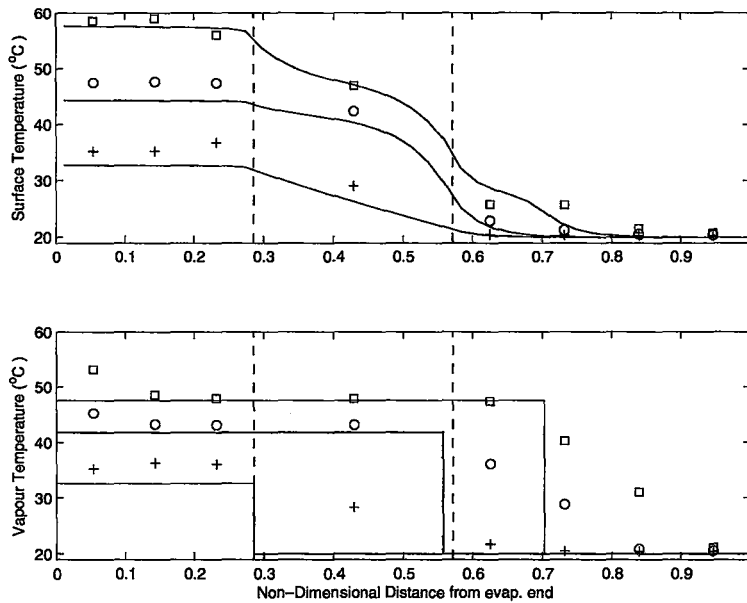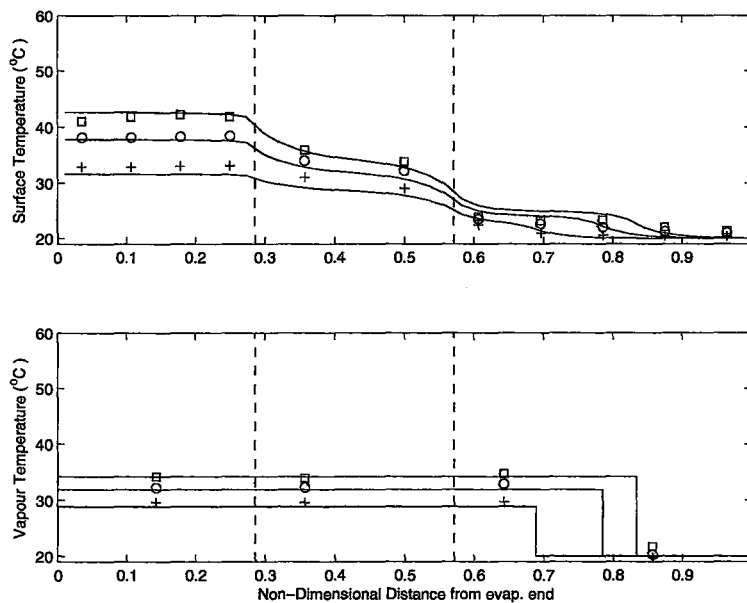
Figure 5.20: Comparison of the predicted and measured transient axial surface and vapour temperature distribution of 4 wick-layer heat pipe with no block for $T_{c,inf} = 20°C$ and heat input of $100W$ at times $+$ $20s$, $\bigcirc$ $40s$ and $\square$ $200s$.
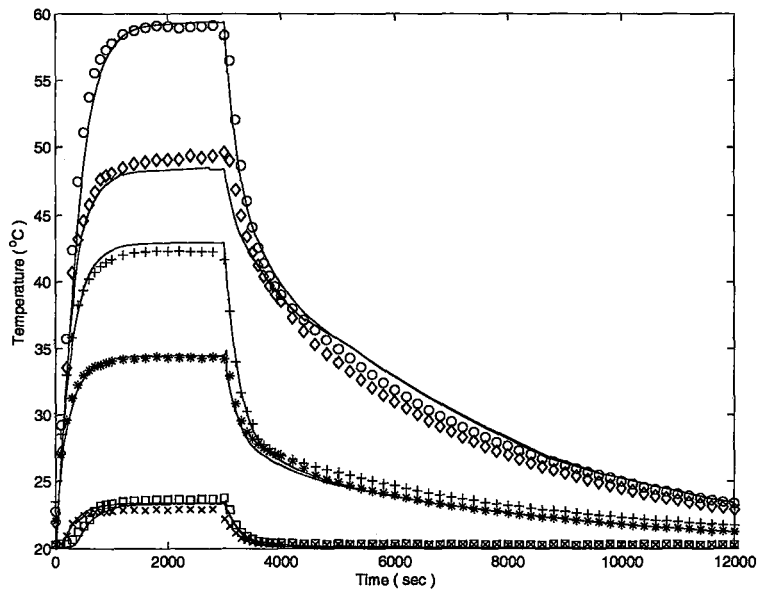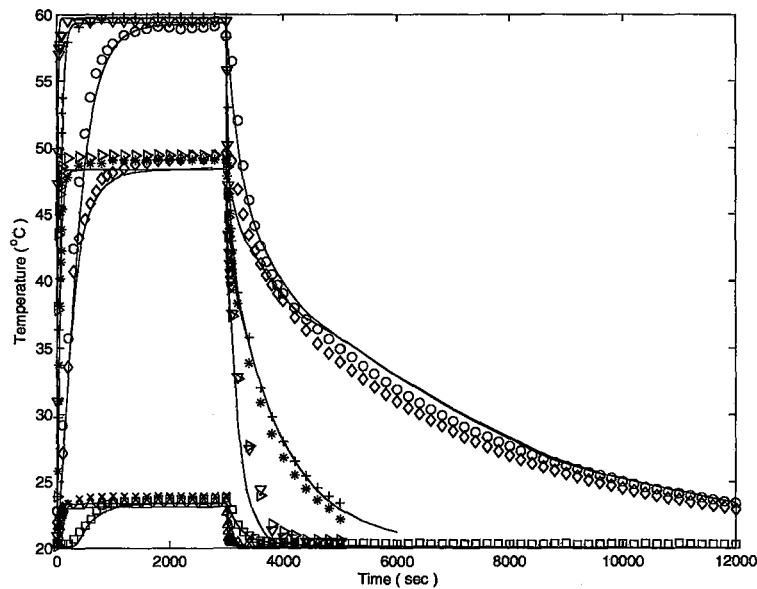

Figure 5.21: Comparison of the transient average temperatures for $T_{c,inf} = 20°C$ and heat input of $100W$ of 4 wick-layer heat pipe using the big block ($\bigcirc$ T_e, $\Diamond$ T_v and $\square$ T_c), the small block ($+$ T_e, $*$ T_v and $\times$ T_c) and no block (∇ T_e, $\triangleright$ T_v and $\triangle$ T_c). (Solid lines represent the model predictions).
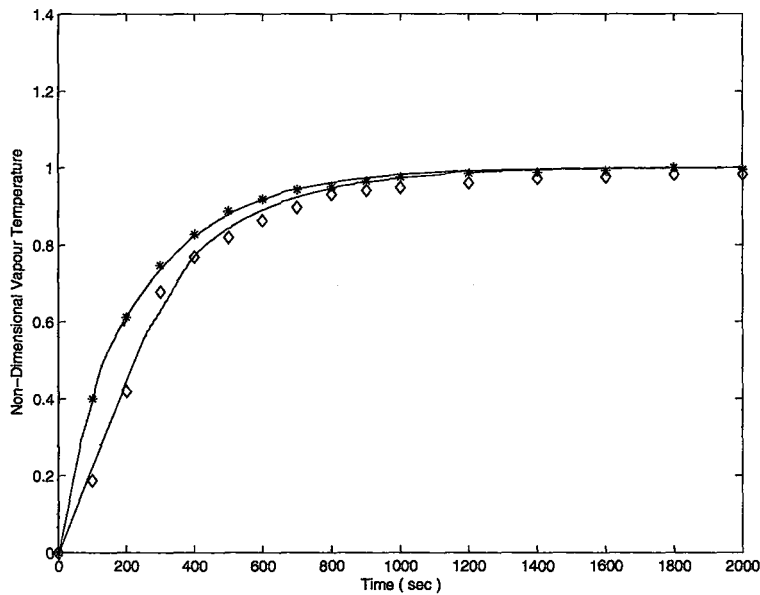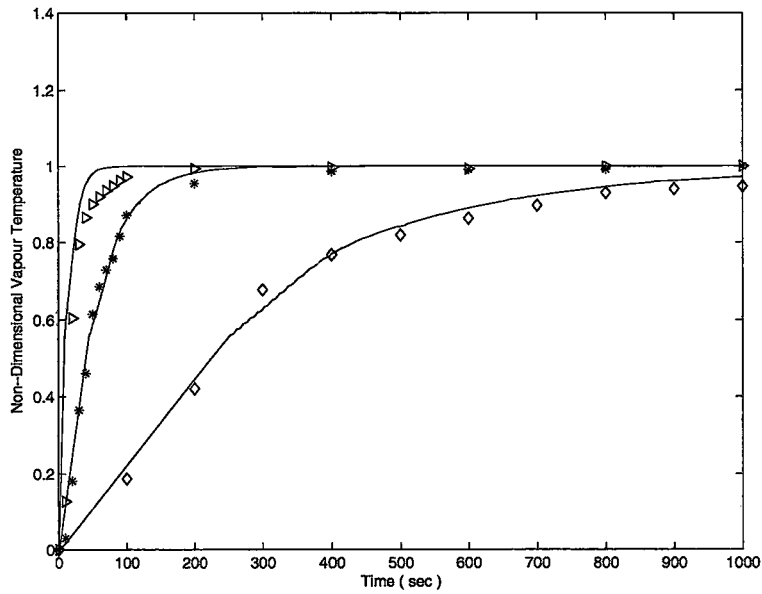
Figure 5.22: Comparison of the non-dimensional vapour temperature for $T_{c,inf} = 20°C$ and heat input of $100W$ of 4 wick-layer heat pipe using $\Diamond$ the big block, $*$ the small block and $\triangleright$ no block. (Solid lines represent the model predictions).

illustrate that the evaporator block is the dominant capacitance in the overall conjugate system, and must be considered in any analysis of thermal management systems using heat pipes.

5.4 Effect of Finned Condenser

The effect of non-uniform boundary conditions on the performance of heat pipes was evaluated by testing three heat pipes with different number of fins at the condenser end (figure 4.9). A bare heat pipe with no fins was also tested for comparison. The heat pipes had 2 wick layers and were tested in a wind tunnel at different air velocities and heat inputs. The tests were performed as steady state where the heater power was increased in steps of 15 $Watts$ while the sink temperature was kept constant at the ambient for all tests. These heat pipes were not internally instrumented, therefore no vapour temperature measurements were recorded. For the heat pipes tested here, the mass of non-condensable gases was evaluated to be 2.4×10^{-7} kg of air.

The steady state axial surface temperature distributions for the heat pipe with 5 fins at different heat inputs are shown in figure 5.23. The evaporator surface temperature distribution is almost unform while that of the condenser is not uniform especially near the end of the condenser due to the non-condensable gases. The surface thermocouples used for this set of heat pipes were OMEGA Self-Adhesive Thermocouples where the junction is secured between a high temperature fiberglass cloth and a high temperature electrically insulating polyimide film. The Polyimide Film has a thickness of 0.3 mm and introduces an additional resistance. Samuels and Mathis (2001) showed that the thermal conductivity of the polyimide film is orientation dependent and has a value between 0.2 to 0.3 $W/m.K$. Using these data, the resistance of the polyimide film was evaluated and the surface temperature measurements were corrected. Although the resistance of the polyimide film is typically small, the small internal resistance of a heat pipe makes the error in the measurements more apparent.

The corrected surface temperature measurements are presented in figure 5.24
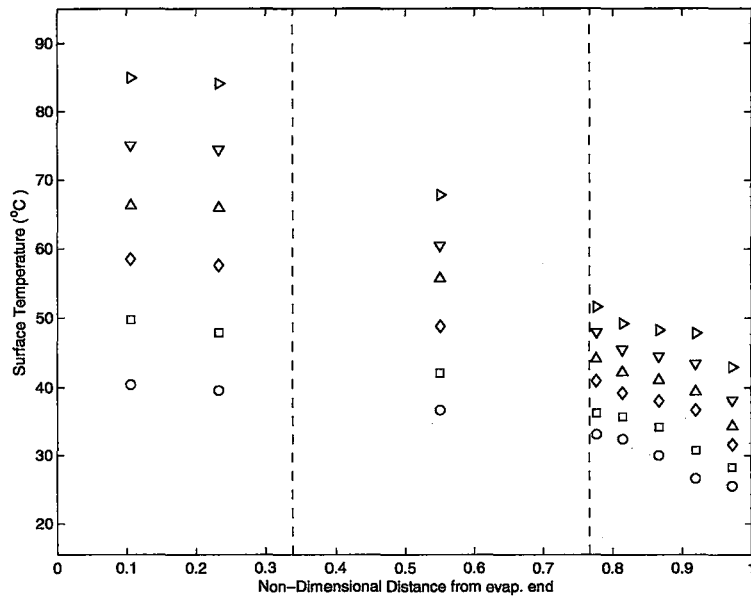
Figure 5.23: Steady axial surface temperature distribution of 5 fin heat pipe at air velocity of 32 m/s for heat input of $\bigcirc$ $15W$, $\square$ $30W$, $\Diamond$ $45W$, $\triangle$ $60W$, ∇ $75W$ and $\triangleright$ $90W$.
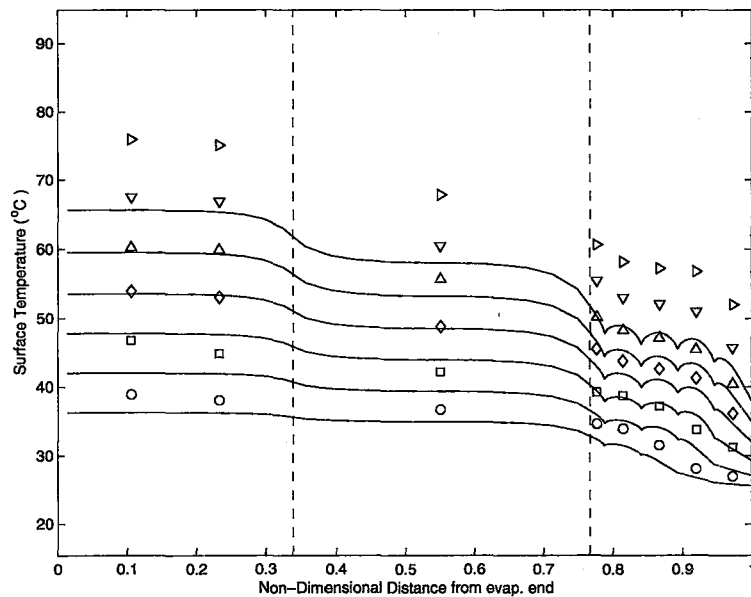
Figure 5.24: Corrected steady axial surface temperature distribution of 5 fin heat pipe at air velocity of 32 m/s for heat input of $\bigcirc$ $15W$, $\square$ $30W$, $\Diamond$ $45W$, $\triangle$ $60W$, ∇ $75W$ and $\triangleright$ $90W$. (Solid lines represent the model predictions).

along with the model predictions using the boundary conditions described in chapter three. The agreement between the experimental results is reasonable for low heat fluxes, while the model underpredicts the surface temperature distribution at higher heat fluxes. The effect of the fins on the condenser surface temperature distribution is more clear from the model results, where there is some non-uniformity in the condenser surface especially at the locations where the fins are attached. At these locations, the temperature is lower by about $2°C$ compared to the adjacent bare surface at high heat fluxes, which is expected due to the localized cooling effects of the fins. However, this non-uniformity did not propagate to the other parts of the heat pipe (i.e. the adiabatic and the evaporator sections). This is mainly due to the high conductive nature of the heat pipe and its ability to equalize the heat pipe surface temperature.

The corrected surface temperature measurements were used to evaluate the internal resistance of the heat pipe, defined by the difference between the average evaporator and condenser surface temperatures divided by the heat input. These results are plotted in figure 5.25 versus the heat input at different wind tunnel air velocities. For a given air velocity, as the heat input increases, the resistance decreases and reaches an asymptotic value at high heat fluxes. This is due to the non-condensable gases which affects the condenser at low heat fluxes. The gases are compressed to the condenser end as the heat flux is increased with a resultant decrease in the thermal resistance. As the air velocity increased, it was noted that the internal thermal resistance also increased. This is likely because an increase in the air velocity results in a decrease in the external resistance, with a consequent decrease in the operating temperature. This decreases the vapour pressure and results in the non-condensable gases occupying a greater portion of the condenser and hence increases the internal resistance. While the model underpredicts the surface temperature distribution at higher heat fluxes as shown earlier, the agreement between the model predictions and the experimental values for the internal resistances is generally good. This could be due to a systematic error in the thermocouples which is canceled when taking the temperature difference. There are still some differences between the model predic-

tions and experimental results at low heat fluxes which can be attributed to the high uncertainty associated with the resistance calculation at low heat fluxes as discussed in chapter four.

The external condenser resistance, defined by the difference between the average condenser surface and sink temperatures divided by the heat input, for the heat pipe with the 5 fins is plotted in figure 5.26 versus the heat input at different wind tunnel air velocities. The external resistance was evaluated using the measured temperature data as they reflect the actual temperature difference between the condenser surface and the ambient temperature. The resistance is nearly independent of the heat input, while it decreases with an increase in the air velocity as expected. The agreement between the model predictions and the experimental values indicates that the correlations used in the modeling of the condenser boundary condition are reasonable. Again, the agreement is not very good at low heat fluxes due to the uncertainty in the thermal resistance at these heat fluxes.

Comparing the values of the internal and external resistances from figures 5.25 and 5.26, it is clear that the external resistance is more dominant, especially at low air velocities and high heat fluxes. Also, the decrease in the external resistance is more significant than the increase in the internal resistance with an increase in the air velocity. The overall heat pipe performance is illustrated in figure 5.27 where the heat transfer rate is plotted as a function of the total temperature difference between the average evaporator surface temperature and the sink temperature for different air velocities. For the higher air velocities, the heat transfer increases more rapidly with the temperature difference due to the decrease in the external resistance with the air velocity. This indicates that the external resistance in this case has a higher impact than the internal resistance on the overall performance of the heat pipe.

The internal and external resistances for the 7 and 12 fin heat pipes along with the heat pipe with no fins are plotted as a function of the heat input at different wind tunnel air velocities in figures 5.28 to 5.33. The trends are similar to the heat pipe with 5 fins, where the internal resistance decreases with the heat input for a given velocity. This is again due to the non-condensable gases that are compressed to the
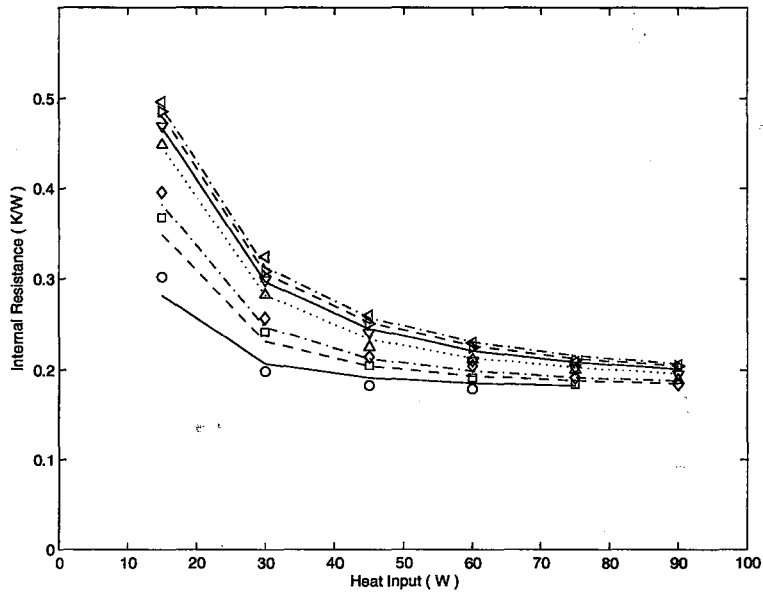
Figure 5.25: Change in internal resistance with heat transfer rate of 5 fin heat pipe for air velocity of —— O 2.9 m/s, – – – □ 5.5 m/s, – · – ◊ 7.5 m/s, · · · · · · △ 14.9 m/s, —— ∇ 20.9 m/s, – – – ▷ 26.6 m/s and – · – ◁ 32 m/s.
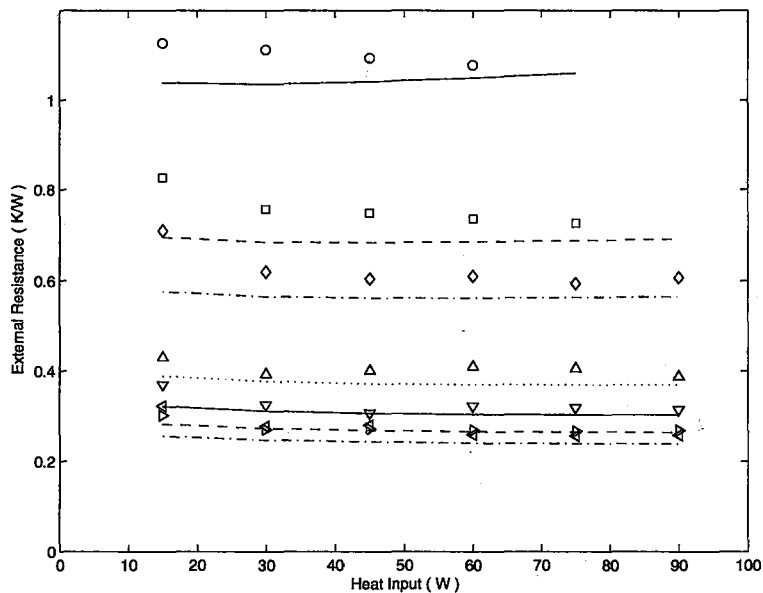
Figure 5.26: Change in external resistance with heat transfer rate of 5 fin heat pipe for air velocity of —— O 2.9 m/s, – – – □ 5.5 m/s, – · – ◊ 7.5 m/s, · · · · · · △ 14.9 m/s, —— ∇ 20.9 m/s, – – – ▷ 26.6 m/s and – · – ◁ 32 m/s.

Figure 5.27: Change in heat transfer rate with temperature difference of 5 fin heat pipe for air velocity of —— ○ 2.9 m/s, – – – □ 5.5 m/s, – · – ◇ 7.5 m/s, · · · · · △ 14.9 m/s, —— ▽ 20.9 m/s, – – – ▷ 26.6 m/s and – · – ◁ 32 m/s.
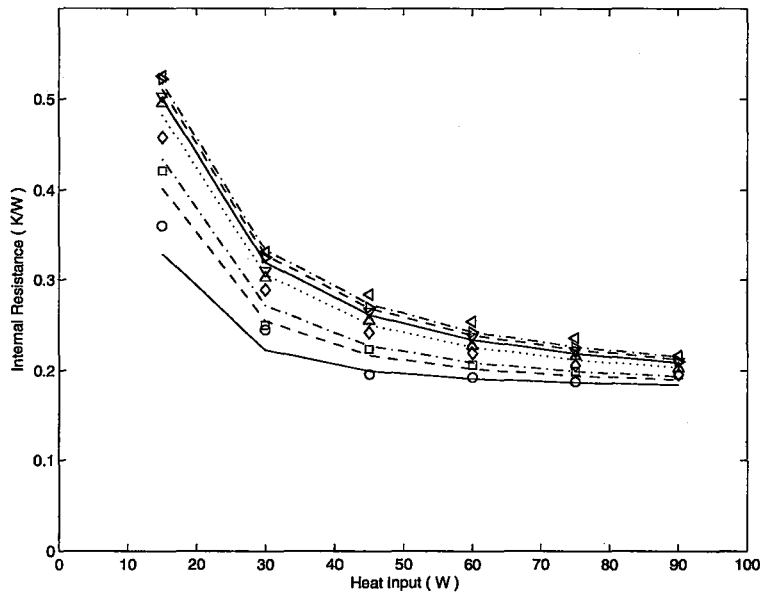
Figure 5.28: Change in internal resistance with heat transfer rate of 7 fin heat pipe for air velocity of ——— ○ 2.9 m/s, – – – □ 5.5 m/s, – · – ◇ 7.5 m/s, ······ △ 14.9 m/s, ——— ▽ 20.9 m/s, – – – ▷ 26.6 m/s and – · – ◁ 32 m/s.

condenser end as the heat flux is increased. Also, the internal resistance increases as the air velocity increases. The external resistance is almost independent of the heat input, while it decreases as the air velocity increases as expected from the forced convection correlations.

The overall heat transfer performance for these three heat pipes are illustrated in figures 5.34, 5.35 and 5.36 respectively, where the heat transfer rate is plotted as a function of the total temperature difference between the average evaporator surface temperature and the sink temperature for different air velocities. These results have similar trends to the heat pipe with 5 fins. Generally, the external resistance is much larger than the internal resistance, especially for the heat pipe with no fins. As the number of fins increases, the external resistance decreases until it becomes comparable to the internal resistance for the 12 fin heat pipe. At the highest air velocity and heat flux, the external resistance for that heat pipe is even smaller than the internal resistance. This causes the slope of the performance curve to be very steep for this case.
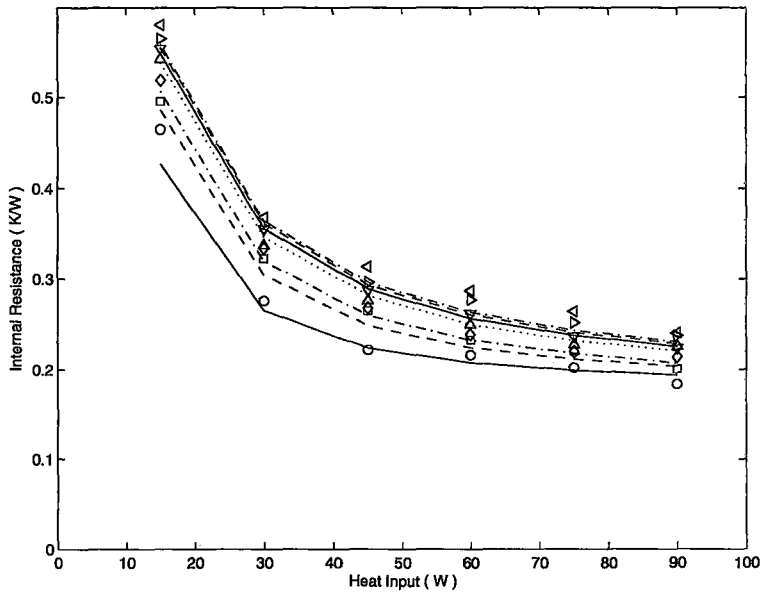
Figure 5.29: Change in internal resistance with heat transfer rate of 12 fin heat pipe for air velocity of —— ○ 2.9 m/s, – – –□ 5.5 m/s, – · – ◊ 7.5 m/s, · · · · · · △ 14.9 m/s, —— ∇ 20.9 m/s, – – –▷ 26.6 m/s and – · – ◁ 32 m/s.
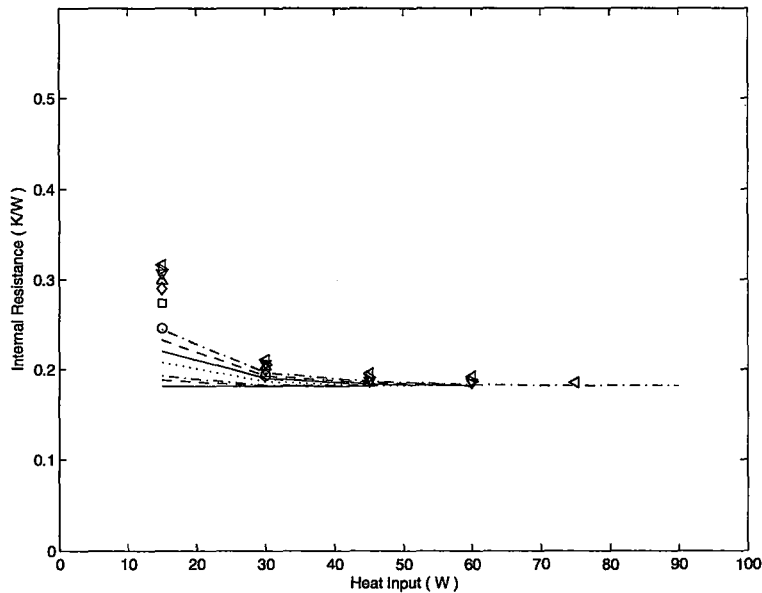
Figure 5.30: Change in internal resistance with heat transfer rate of bare heat pipe for air velocity of —— ○ 2.9 m/s, – – –□ 5.5 m/s, – · – ◊ 7.5 m/s, · · · · · · △ 14.9 m/s, —— ∇ 20.9 m/s, – – –▷ 26.6 m/s and – · – ◁ 32 m/s.
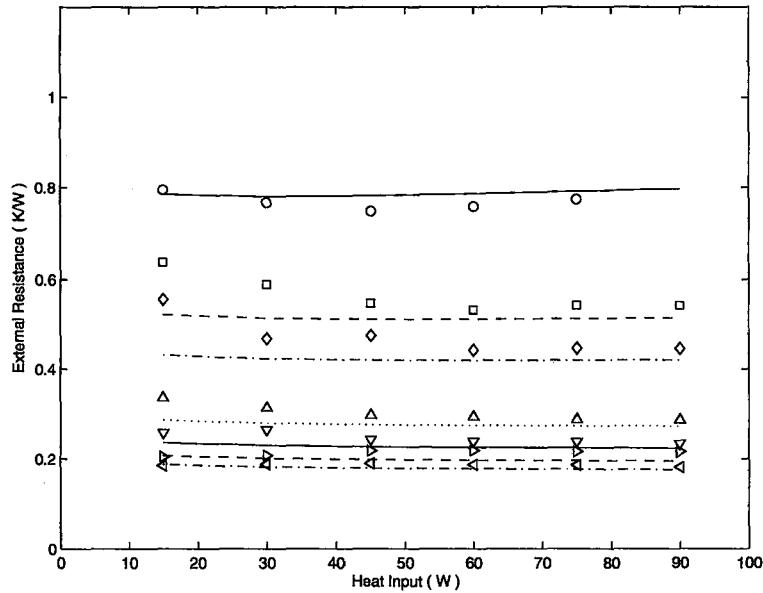
Figure 5.31: Change in external resistance with heat transfer rate of 7 fin heat pipe for air velocity of —— O 2.9 m/s, – – – □ 5.5 m/s, – · – ◇ 7.5 m/s, · · · · · · △ 14.9 m/s, —— ∇ 20.9 m/s, – – – ▷ 26.6 m/s and – · – ◁ 32 m/s.
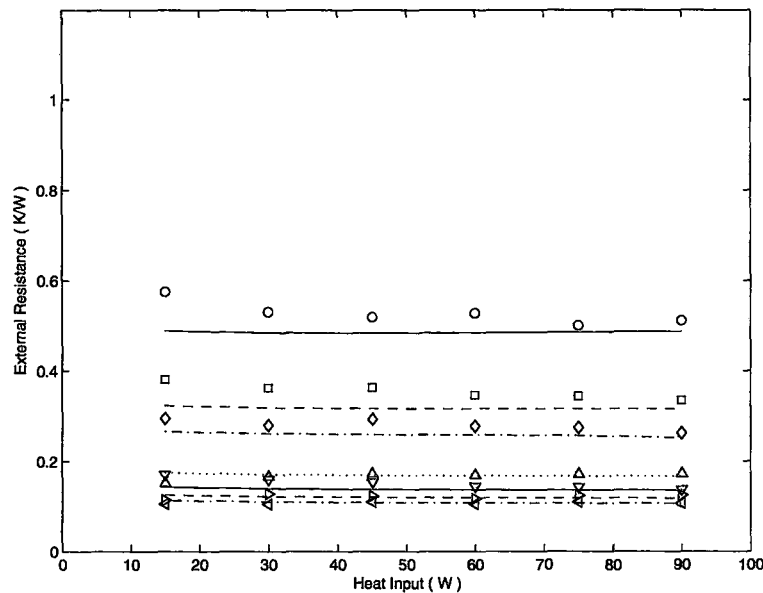
Figure 5.32: Change in external resistance with heat transfer rate of 12 fin heat pipe for air velocity of —— O 2.9 m/s, – – – □ 5.5 m/s, – · – ◇ 7.5 m/s, · · · · · · △ 14.9 m/s, —— ∇ 20.9 m/s, – – – ▷ 26.6 m/s and – · – ◁ 32 m/s.
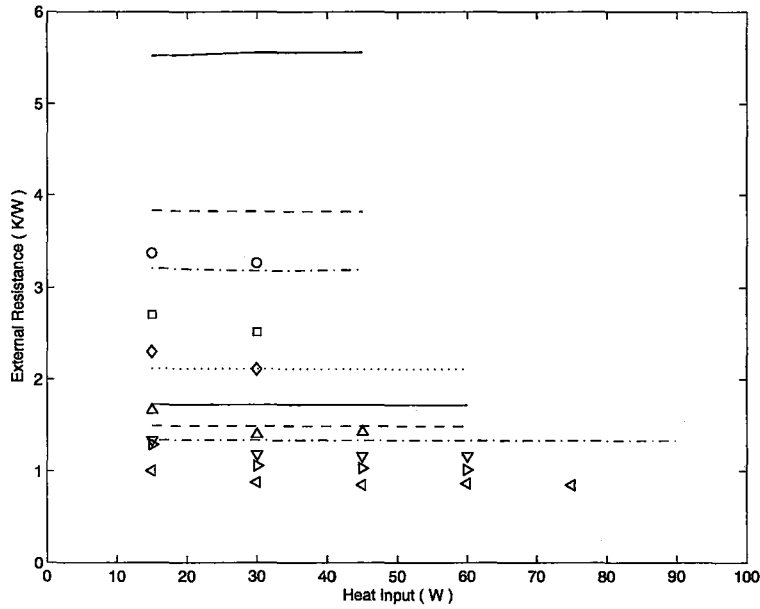
Figure 5.33: Change in external resistance with heat transfer rate of bare heat pipe for air velocity of —— ○ 2.9 m/s, – – – □ 5.5 m/s, – · – ◇ 7.5 m/s, · · · · · · △ 14.9 m/s, —— ▽ 20.9 m/s, – – – ▷ 26.6 m/s and – · – ◁ 32 m/s.
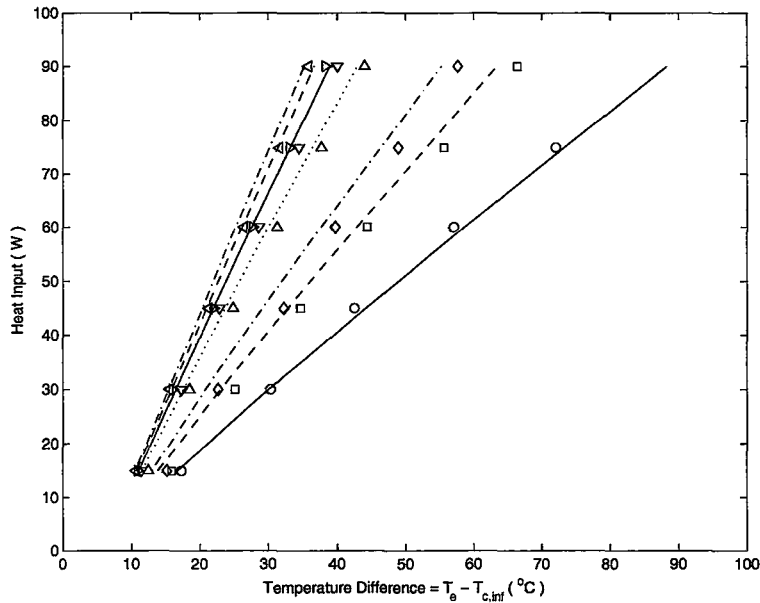
Figure 5.34: Change in heat transfer rate with temperature difference of 7 fin heat pipe for air velocity of —— ○ 2.9 m/s, – – – □ 5.5 m/s, – · – ◇ 7.5 m/s, · · · · · · △ 14.9 m/s, —— ▽ 20.9 m/s, – – – ▷ 26.6 m/s and – · – ◁ 32 m/s.
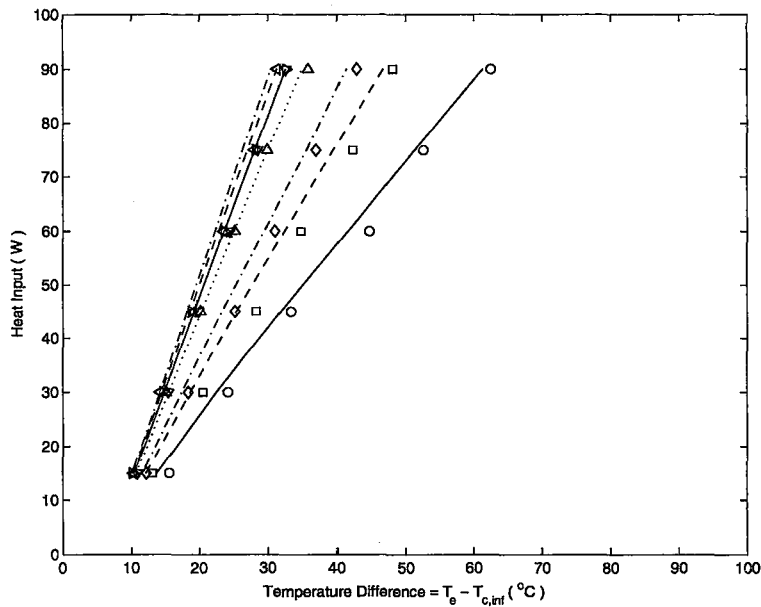
Figure 5.35: Change in heat transfer rate with temperature difference of 12 fin heat pipe for air velocity of —— O 2.9 m/s, – – – □ 5.5 m/s, – · – ◊ 7.5 m/s, · · · · · · △ 14.9 m/s, —— ∇ 20.9 m/s, – – – ▷ 26.6 m/s and – · – ◁ 32 m/s.

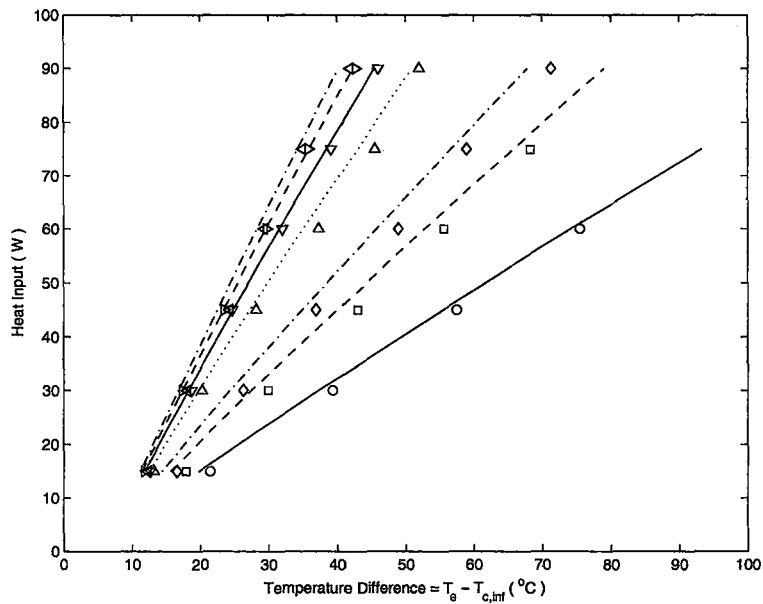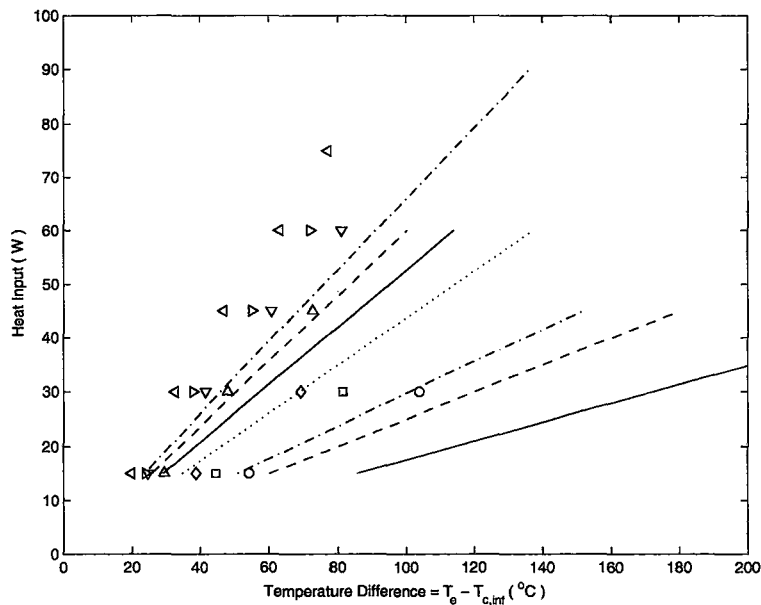Figure 5.36: Change in heat transfer rate with temperature difference of bare heat pipe for air velocity of —— O 2.9 m/s, – – – □ 5.5 m/s, – · – ◊ 7.5 m/s, · · · · · · △ 14.9 m/s, —— ∇ 20.9 m/s, – – – ▷ 26.6 m/s and – · – ◁ 32 m/s.

There is fairly good agreement for the external resistance, internal resistance and overall performance between the model predictions and the experimental results for the 5 fin, 7 fin, and 12 fin heat pipes. For the bare heat pipe, the internal resistances agree well with the model predictions except at low heat fluxes. However, the prediction of the external resistance is higher by about 60% at low air velocities and about 25% at higher air velocities, which also affects the overall performance. This was expected since the forced convection correlation used for the bare heat pipe is for a two-dimensional flow over a long cylinder with no end effects. However, the experimental case is basically a three dimensional flow over a shorter cylinder with length to diameter ratio of about 3.5. The end effects in this case would be significant with an enhanced heat transfer due to the flow separation over the free cylinder end. These effects are not that significant for the finned heat pipes as the extended surface of the fins reduces the end effects substantially.

The change in the internal resistance with fin density is compared to the model predictions in figure 5.37. The results are presented at an air velocity of 32 m/s and at different heat input levels. As the heat input increases, the internal resistance of the heat pipe decreases since a greater portion of the condenser is active due to the compression of the non-condensable gases to a smaller volume. For a given fin density, the internal resistance would be independent of the heat flux if there were no non-condensable gases in the heat pipe. The internal resistance increases slightly with the fin density. As the fin density increases, the external resistance decreases and the temperature difference between the operating and sink temperatures decreases too, and consequently the non-condensable gases expand deactivating a larger portion of the condenser and increasing the internal resistance. This is more clear at low heat fluxes, while at higher heat fluxes the increase of the internal resistance with the fin density is very limited. For example, the increase is less than 10% at high heat flux compared to 85% increase at the low heat flux.

The change in the external resistance with fin density is compared to the model predictions at air velocity of 32 m/s for different heat inputs in figure 5.38. It is clear that the external resistance is almost constant at every fin density regardless of the
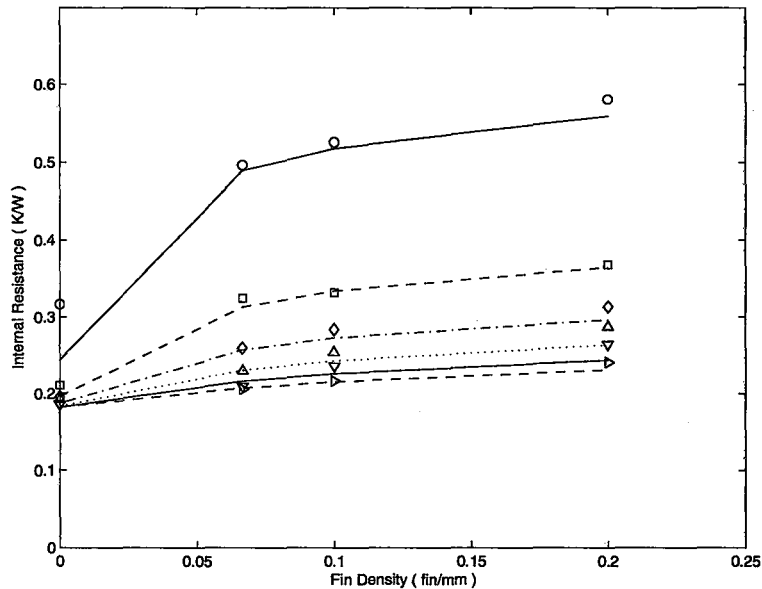
Figure 5.37: Change in internal resistance with fin density at air velocity of 32 m/s for heat input of —— O $15W$, – – – □ $30W$, – · – ◇ $45W$, · · · · · · △ $60W$, —— ∇ $75W$ and – – – ▷ $90W$.

heat input.

The change in the internal resistance with fin density is compared to the model predictions for different air velocities in figure 5.39. The internal resistance is nearly constant with fin density at low air velocities, while at the higher air velocities the internal resistance increases by about 35% at the highest fin density compared to the bare heat pipe. At the highest fin density and highest air velocity, the external resistance would be a minimum and therefore the non-condensable gases would occupy a larger volume, thereby increasing the internal resistance. It is important to note that this comparison is made at a heat input level of 60 *Watts* as the maximum heat input level 90 *Watts* could not be achieved for some of the heat pipes due to the evaporator surface temperature exceeding the maximum allowable temperature (140°C) for the type of thermocouples used in the experiments.

The change in the external resistance with fin density is compared to the model predictions for different air velocities in figure 5.40. These results were compared again at a heat input level of 60 *Watts*. As the air velocity increases, the external
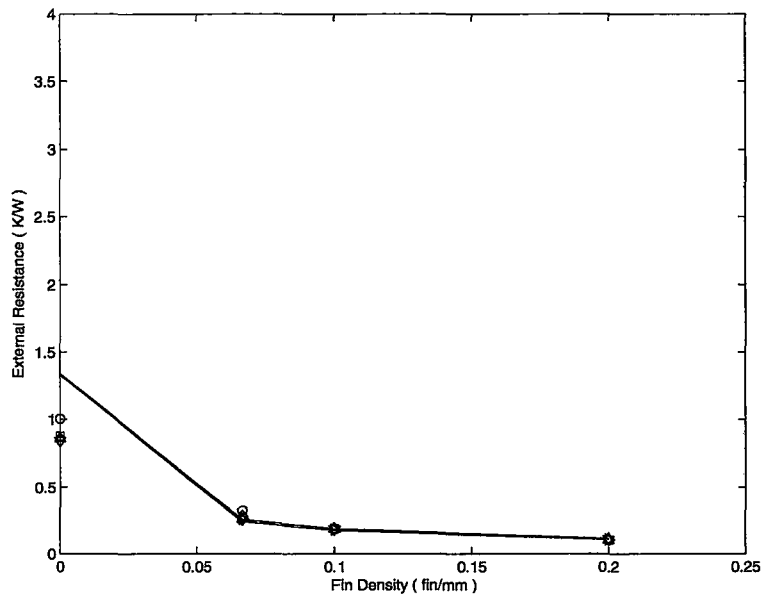
Figure 5.38: Change in external resistance with fin density at air velocity of 32 m/s for heat input of —— ○ $15W$, $---$ □ $30W$, $-\cdot-$ ◊ $45W$, $\cdots\cdots$ △ $60W$, —— ▽ $75W$ and $---$ ▷ $90W$.
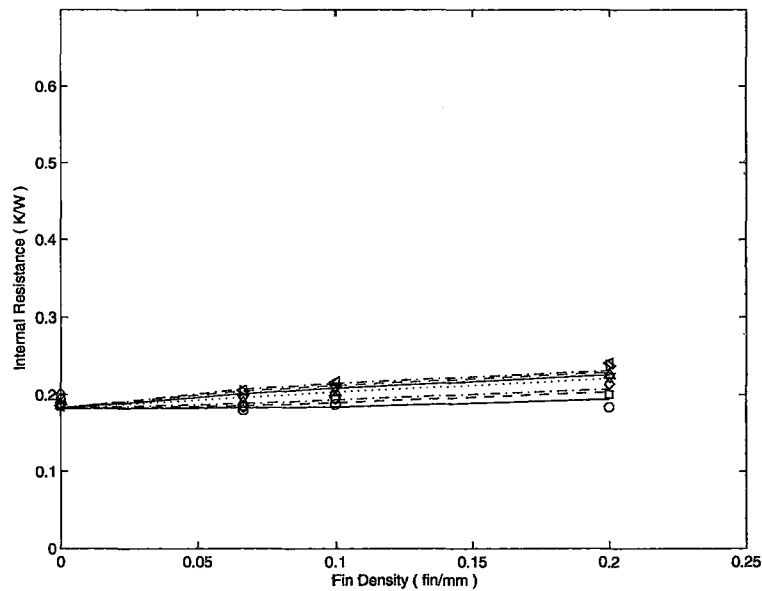
Figure 5.39: Change in internal resistance with fin density at heat input of $60W$ for air velocity of —— ○ 2.9 m/s, $---$ □ 5.5 m/s, $-\cdot-$ ◊ 7.5 m/s, $\cdots\cdots$ △ 14.9 m/s, —— ▽ 20.9 m/s, $---$ ▷ 26.6 m/s and $-\cdot-$ ◁ 32 m/s.
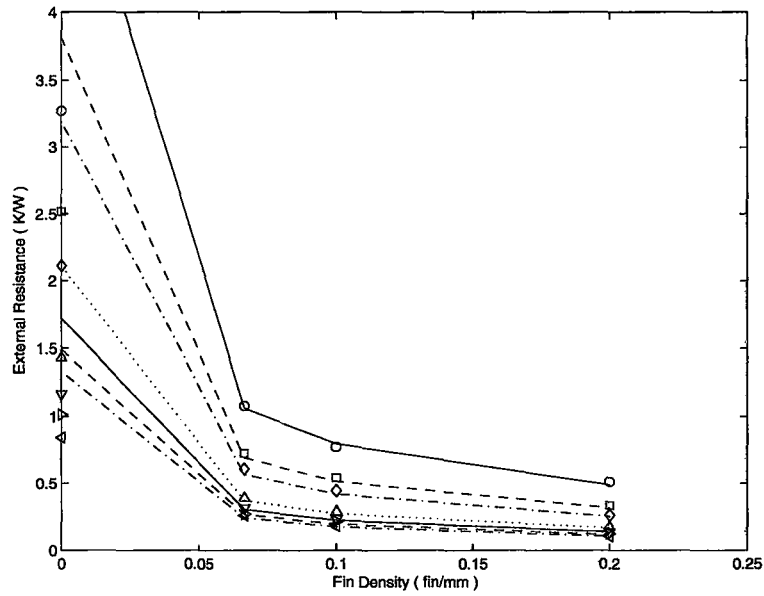
Figure 5.40: Change in external resistance with fin density at heat input of $60W$ for air velocity of —— O 2.9 m/s, – – – □ 5.5 m/s, – · – ◇ 7.5 m/s, · · · · · · △ 14.9 m/s, —— ▽ 20.9 m/s, – – – ▷ 26.6 m/s and – · – ◁ 32 m/s.

resistance decreases as expected. Also, the external resistance decreases with an increase in fin density as expected due to the increase of the extended surface area with a higher fin density. The model predictions are in good agreement with the experimental results except for the bare heat pipe as discussed earlier in terms of the end effects for this case.

CHAPTER 6
CONCLUSIONS AND
RECOMMENDATIONS

6.1 Conclusions

An existing transient wicked heat pipe network model was expanded to include the effect of the surrounding media, axial wall and wick conduction, and non-condensable gases. The thermal resistance of the different components of the heat pipe was divided into a large number of resistances in both axial and radial directions to incorporate the axial heat conduction in the heat pipe wall and wick and to handle non-uniform boundary conditions. A simple flat-front model for the non-condensable gases was also incorporated in the model. Two sets of experiments were performed on copper-water wicked heat pipes. The first set of experiments tested the heat pipes using a cooling water jacket at the condenser. Steady and transient tests were performed to investigate the effect of non-condensable gases, axial heat conduction, wick thickness and surrounding media using different evaporator block sizes. The second set of experiments tested the effect of a finned condenser on the overall steady-state performance of a heat pipe. These tests were performed in a wind tunnel where the finned condenser was placed in the cross flow of the air. The model predictions of the steady and transient response of the vapour and wall temperatures were in good agreement with the experimental results.

The presence of even a very small amount of non-condensable gases inside the heat pipe increased the overall thermal resistance of the heat pipe. The performance of the heat pipe in this case is dependent on the operating temperature, as the length of the inactive portion of the condenser occupied by the non-condensable gases is dependent on the vapour pressure. The presence of non-condensable gases did not significantly affect the transient response in the heat-up phase. For the cool-down

phase, however, the non-condensable gases significantly slows down the cooling rate of the heat pipe as it occupies a greater portion of the condenser as the temperature progressively decreases.

The axial heat conduction in the heat pipe wall and wick can be important in the performance of the heat pipes. Neglecting the axial conduction through the pipe wall and the wick structure increased the predicted overall thermal resistance of the heat pipe model. The axial conduction did not have a great influence on the time response during the heat-up phase, but changed the steady-state values. During the cool-down phase, however, the axial conduction has a significant effect, particulary when the condenser is completely blocked by the non-condensable gases. In this case, the axial heat conduction becomes the primary mode of heat transfer from the hot end to the colder end.

The wick structure is the dominant thermal resistance in both the steady-state and the transient performance of the heat pipe. It has a much higher thermal resistance and a slightly lower thermal capacitance compared to the heat pipe wall. The wick structure has a greater influence on the transient performance than the amount of non-condensable gases entrapped in the heat pipe, especially at higher operating temperatures when the effect of non-condensable gases is small.

From the experimental results using different evaporator block sizes, the heat pipe that was directly heated had the fastest transient response during both the heat-up and cool-down phases. The results show that the block, even if small, causes a slower response. This becomes more significant as the size of the block increases. These results clearly illustrate that the evaporator block is the dominant capacitance in the overall conjugate system, and must be considered in any analysis of thermal management systems using heat pipes.

The experimental results from the finned condenser heat pipe study showed that the variation in the condenser surface temperature was small even with the localized cooling effects due to the presence of the fins. The heat pipe tends to equalize any temperature differences on its surface and therefore these temperature variations did not propagate to the other sections of the heat pipe. The internal resistance increased

slightly with the fin density. As the fin density increased, the external resistance decreased and the operating temperature difference between the vapour and the sink decreased. This results in an expansion of the non-condensable gases, deactivating a larger portion of the condenser and increasing the internal resistance.

6.2   Recommendations

The improved network model developed in this thesis considered the heat conduction in both the radial and axial directions in the heat pipe wall and wick. The current model can take into account non-uniform boundary conditions along the axial direction. It is recommended that the model be expanded to include variations in the circumferential direction. This will allow further investigation of the heat pipe performance in a wider range of applications, such as the iso-platens where the heat is applied to only part of the circumferential heat pipe surface area.

A flat-front model for the non-condensable gases was used in this study. The experimental results showed that the vapour-gas interface is not as sharp as expected. Therefore, a more sophisticated mass diffusion model between the gas and the vapour needs to be incorporated in the existing model and the results compared with the existing experimental data to evaluate the importance of such diffusion effects on the heat pipe performance.

It was noted that the amount of non-condensable gases entrapped in the heat pipes was different and was generally large and dependent on the instrumentation method used for the internal vapour core temperature measurements. The built up of non-condensable gases can also occur over a period of time. It is recommended that a method be developed to vacuum and charge the heat pipes before each test to better control the amount of non-condensable gases in each heat pipe.

BIBLIOGRAPHY

Asselman, G. A. A., Green, D. B., 1973. Heat pipes: I. operation and characteristics. Philips Technical Review 33 (4), 104 – 113.

Bobco, R. P., 1987. Variable conductance heat pipes: A first-order model. Journal of Thermophysics and Heat Transfer 1 (1), 35 – 42.

Bowman, W. J., Beran, P. S., 1994. Implicit heat pipe vapor model. Journal of Thermophysics and Heat Transfer 8 (1), 187 – 190.

Bowman, W. J., Hitchcock, J. E., 1988. Transient, compressible heat-pipe vapor dynamics. American Society of Mechanical Engineers, Heat Transfer Division, (Publication) HTD 96, 329 – 337.

Bowman, W. J., Winn, R. C., Martin, H. L., 1992. Transient heat-pipe modeling - a quasisteady, incompressible vapor model. Journal of Thermophysics and Heat Transfer 6 (3), 571–574.

Briggs, D. E., Young, E. H., 1963. Convection heat transfer and ressure drop of air flowing across triangular pitch banks of finned tubes. Chemical Engineering Progress Symposium Series 59 (41), 1 – 10.

Cao, Y., Faghri, A., 1990. Transient two-dimensional compressible analysis for high-temperature heat pipes with pulsed heat input. Numerical Heat Transfer; Part A: Applications 18 (4), 483 – 502.

Chang, W. S., 1990. Porosity and effective thermal conductivity of wire screens. Journal of Heat Transfer, Transactions ASME 112 (1), 5 – 9.

Chi, S. W., 1976. Heat Pipe Theory and Practice. McGraw-Hill, New York.

Chung, J. H., Edwards, D. K., 1996. Moving gas front effects on heat pipe transient behavior. Journal of Thermophysics and Heat Transfer 10 (1), 76 – 82.

Churchill, S. W., Bernstein, M., 1977. Correlating equation for forced convection from gases and liquids to a circular cylinder in crossflow. Journal of Heat Transfer, Transactions ASME 99 Ser C (2), 300 – 306.

Dormand, J. R., Prince, P. J., 1980. Family of embedded runge-kutta formulae. Journal of Computational and Applied Mathematics 6 (1), 19 – 26.

Dunn, P. D., Reay, D. A., 1978. Heat Pipes, 2nd Edition. Pergamon Press, Oxford, New York.

Edwards, D. K., Marcus, B. D., 1972. Heat and mass transfer in the vicinity of the vapor-gas front in a gas-loaded heat pipe. Journal of Heat Transfer, Transactions ASME 94 Ser C (2), 155 – 162.

El-Genk, M. S., Huang, L., 1993. Experimental investigation of the transient response of a water heat pipe. International Journal of Heat and Mass Transfer 36 (15), 3823 – 3830.

Eldridge, J. M., Petersen, K. E., 1983. Heat pipe vapor cooling etched silicon structure. IBM technical disclosure bulletin 25 (8), 4118–4119.

Faghri, A., 1995. Heat Pipe: Science and Technology. Taylor & Francis, Washington, DC.

Faghri, A., Buchko, M., 1990. Experimental and numerical analysis of low temperature heat pipes with multiple heat sources. American Society of Mechanical Engineers, Heat Transfer Division, (Publication) HTD 156, 51 – 58.

Faghri, A., Buchko, M., Cao, Y., 1991. Study of high temperature heat pipes with multiple heat sources and sinks part ii. analysis of continuum transient and steady state experimental data with numerical predictions. American Society of Mechanical Engineers (Paper), 1 – 9.

Faghri, A., Harley, C., 1994. Transient lumped heat pipe analysis. Heat Recovery Systems & CHP 14 (4), 351 – 363.

Faghri, A., Reynolds, D. B., Najafi, P., 1987. Innovative method for hand protection from extreme cold using heat pipe technology. American Society of Mechanical Engineers, Bioengineering Division, (Publication) BED 5, 91–97.

Gaugler, R. S., 1944. Heat transfer device. U.S. Patent 2,350,348.

Grover, G. M., Cotter, T. P., Erickson, G. F., 1964. Structures of very high thermal conductance. Journal of Applied Physics 35 (6), 1990 – 1991.

Grover, L. K., 1977. Cross flow induced vibrations deep inside a closely-packed tube-bank. Ph.D. thesis, McMaster University (Mechanical Engineering), Hamilton, Ontario, Canada.

Hashizume, K., Matsue, T., Sueoka, Y., 2003. Effects of fins on forced convection heat transfer around a tube. Heat Transfer - Asian Research 32 (5), 445 – 454.

Howard, A. H., Peterson, G. P., 1995. Investigation of a heat pipe array for convective cooling. Journal of Electronic Packaging, Transactions of the ASME 117 (3), 208 – 214.

Incropera, F. P., DeWitt, D. P., 1996. Fundamentals of Heat and Mass Transfer, 4th Edition. John Wiley & Sons, New York.

Issacci, F., Catton, I., Ghoniem, N. M., 1991. Vapour dynamics of heat pipe start-up. Journal of Heat Transfer, Transactions ASME 113 (4), 985 – 994.

Ivanovskii, M. N., Sorokin, V. P., Yagodkin, I. V., 1982. The physical principles of heat pipes. Clarendon Press, Oxford, New York.

Jang, J. H., Faghri, A., Chang, W. S., 1991. Analysis of the one-dimensional transient compressible vapor flow in heat pipes. International Journal of Heat and Mass Transfer 34 (8), 2029 – 2037.

Kempers, R. S., 2004. The effect of wick thickness and fluid loading on the performance of wicked heat pipes. Master's thesis, McMaster University (Mechanical Engineering), Hamilton, Ontario, Canada.

Kempers, R. S., Ching, C. Y., Ewing, D., 2005. Measurement of evaporator and condenser thermal resistance in wicked heat pipes. Tech. Rep. TMRL-TR106-2005, Thermal Management Research Laboratory, McMaster University.

Kimura, H., Itagaki, H., Sakurai, Y., 1981. Transient performance of gas-loaded, variable conductance heat pipes with a hot reservoir. In: Proceedings of the 4th International Heat Pipe Conference. London, England, pp. 589 – 600.

Kline, S. J., McClintock, F. A., 1953. Describing uncertainties in single-sample experiments. Mechanical Engineering 75 (1), 3 – 8.

Marcus, B. D., 1972. Theory and design of variable conductance heat pipes. Tech. Rep. CR-2018, NASA.

Marcus, B. D., Fleischman, G. L., 1970. Steady-state and transient performance of hot reservoir gas-controlled heat pipes. American Society of Mechanical Engineers (Paper) (70-HT/SpT-11), 1 – 8.

North, M. T., Avedisian, C. T., 1993. Heat pipes for cooling high flux/high power semiconductor chips. Journal of Electronic Packaging, Transactions of the ASME 115 (1), 112 – 117.

Peterson, G. P., 1994. An Introduction to Heat Pipes: Modeling, Testing, and Applications. John Wiley & Sons, New York.

Polasek, F., Stulc, P., Nassler, J., 1988. Using heat pipes in electrical engineering, i. properties and design of heat pipes from the point of view of cooling in electrical engineering. Elektrotechnicky obzor 77 (2), 91–100.

Ponnappan, R., 1989. Studies on the start-up transients and performance of a gas-loaded sodium heat pipe. Tech. Rep. WRDC-TR-89-2046, Wright-Patterson AFP, OH.

Ponnappan, R., Chang, W. S., 1994. Startup performance of a liquid-metal heat pipe in near-vacuum and gas-loaded modes. Journal of Thermophysics and Heat Transfer 8 (1), 164–171.

Rice, G., Azad, E., 1976. Dynamic characteristics of heat pipes. Advances in Environmental Science and Technology 1, 153 – 164.

Roache, P. J., 1997. Quantification of uncertainty in computational fluid dynamics. Annual Review of Fluid Mechanics 29, 123 – 160.

Roache, P. J., 1998. Verification and Validation in Computational Science and Engineering. Hermosa Publishers, Albuquerque, New Mexico.

Samuels, R. J., Mathis, N. E., 2001. Orientation specific thermal properties of polyimide film. Journal of Electronic Packaging, Transactions of the ASME 123 (3), 273 – 277.

Schmalhofer, J., Faghri, A., 1993a. A study of circumferentially-heated and block-heated heat pipes. i. experimental analysis and generalized analytical prediction of capillary limits. International Journal of Heat and Mass Transfer 36 (1), 201 – 212.

Schmalhofer, J., Faghri, A., 1993b. A study of circumferentially-heated and block-heated heat pipes. ii. three-dimensional numerical modeling as a conjugate problem. International Journal of Heat and Mass Transfer 36 (1), 213 – 226.

Shukla, K. N., 1981. Transient response of a gas-controlled heat pipe. AIAA Journal 19 (8), 1063 – 1070.

Sun, K. H., Tien, C. L., 1972. Simple conduction model for theoretical steady-state heat pipe performance. AIAA Journal 10 (8), 1051 – 1057.

Sun, K. H., Tien, C. L., 1975. Thermal performance characteristics of heat pipes. International Journal of Heat and Mass Transfer 18 (3), 363 – 380.

Tournier, J.-M., El-Genk, M. S., 1994. Heat pipe transient analysis model. International Journal of Heat and Mass Transfer 37 (5), 753 – 762.

Trefethen, L., 1962. On the surface tension pumping of liquids or a possible role of the candlewick in space exploration. Tech. Rep. SN 61-SD-114, General Electric Technical Information.

Wang, C.-Y., Groll, M., Roesler, S., Tu, C.-J., 1994. Porous medium model for two-phase flow in mini channels with applications to micro heat pipes. Heat Recovery Systems & CHP 14 (4), 377 – 389.

Zhao, Z., Avedisian, C. T., 1997. Enhancing forced air convection heat transfer from an array of parallel plate fins using a heat pipe. International Journal of Heat and Mass Transfer 40 (13), 3135 – 3147.

Zuo, Z. J., Faghri, A., 1997. Boundary element approach to transient heat pipe analysis. Numerical Heat Transfer; Part A: Applications 32 (3), 205 – 220.

Zuo, Z. J., Faghri, A., 1998. Network thermodynamic analysis of the heat pipe. International Journal of Heat and Mass Transfer 41 (11), 1473 – 1484.

APPENDIX A
MODEL SOURCE CODE

This appendix provides the source code of the model used in this study. Table A.1 gives a short description for each file. In the source code there are other functions not listed here that are used to account for the temperature-dependant properties of copper, aluminum, water and air.

Equation 3.21 is used for the axial and radial resistances for each component, while equation 3.22 is the governing equation for each component and solved using the ODE solver (listing A.2) with adaptive time steps.

Table A.1: Summary of source code listings.

Number	File Name	Description
Listing A.1	model.m	This is the main file for the simulation. It calls the input file and the ODE equations file specifying the optional arguments for the ODE solver.
Listing A.2	eqns.m	This is the file that defines the equations for the ODE solver (equation 3.22).
Listing A.3	in.m	This file contains all the input parameters for the simulation.
Listing A.4	heat.m	This file defines the heat input function to the evaporator section.

Listing A.1: Main File

```
1  % Main File for the Model

   clear
   clc
   tic
6
   [e a c m n k z mm nn zz all Tinf flow mg Rg T0 L Le Lc La Leff do di db dconv Ap Ac Ae N Nw d tw dv Av Aw por K rcap] = in\
   (cont.)(1);


   options = odeset('RelTol',1e−3,'AbsTol',1e−6);
   [t T] = ode45(@eqns,[0 12000],T0,options);
11
   i = [1:all];
   tmax= max(size(t));


   Qe = heat(t)';
16 Q = repmat(Qe/e,1,e);


   % Non−Condensable Gases Modelling Part !
   if (mg > 0) Lcin = mg*Rg*Tinf./((w_psat(T(:,nn+1))−w_psat(Tinf))*Av);
   else Lcin = 0.0*T(:,nn+1);
21 end
   Lcac = Lc + La − Lcin;
   j = find(Lcac < 0); Lcac(j) = 0.0;
   sumL_a = repmat([1:a]*La/a,tmax,1);
   sumL_c = repmat([1:c]*Lc/c + La,tmax,1);
26 for j = 1:tmax
       ia1 = find(sumL_a(j,:) <= Lcac(j)); ia2 = find(sumL_a(j,:) > Lcac(j));
       ic1 = find(sumL_c(j,:) <= Lcac(j)); ic2 = find(sumL_c(j,:) > Lcac(j));
       Lca_e = zeros(j,z+e);
       Lca_a(j,ia1) = La/a; Lca_a(j,ia2) = La/a−(sumL_a(j,ia2)−Lcac(j));
31     Lca_c(j,ic1) = Lc/c; Lca_c(j,ic2) = Lc/c−(sumL_c(j,ic2)−Lcac(j));
   end


   % calculating the length (Lall) and active length (Lalla) for each element !
   Lz1 = repmat([repmat(Le/e,1,e) repmat(La/a,1,a) repmat(Lc/c,1,c)],1,m+n);
36 Lz1a = repmat([repmat(Le/e,1,e) repmat(La/a,1,a) repmat(Lc/c,1,c)],1,m+n−1);
   Lz1b = repmat(Le/e,1,e); Lz2=zeros(1,zz−nn); Lz3=repmat(repmat(Le/e,1,e),1,k);
   Lall = repmat([Lz1 Lz2 Lz3],tmax,1);
   Lalla = [repmat(Lz1a,tmax,1) repmat(Lz1b,tmax,1) Lca_a Lca_c repmat(Lz2,tmax,1) repmat(Lz3,tmax,1)];
   j = find(Lalla < 0); Lalla(j) = 0.0;
41
   % calculating the outer and inner diameters for each element !
   dowa(1:z,1:m) = repmat(do−([1:m]−1).*(do−di)/m,z,1);
   diwa(1:z,1:m) = repmat(do−[1:m].*(do−di)/m,z,1);
   dowc(1:z,1:n) = repmat(di−([1:n]−1).*(di−dv)/n,z,1);
46 diwc(1:z,1:n) = repmat(di−[1:n].*(di−dv)/n,z,1);
   dobk(1:e,1:k) = repmat(do+[1:k].*(db−do)/k,e,1);
   dibk(1:e,1:k) = repmat(do+([1:k]−1).*(db−do)/k,e,1);
   do1(1:mm)=dowa(1:mm); do2(1:z*n)=dowc(1:z*n);
   do3=zeros(1,zz−nn); do4(1:e*k)=dobk(1:e*k);
51 di1(1:mm)=diwa(1:mm); di2(1:z*n)=diwc(1:z*n);
   di3=zeros(1,zz−nn); di4(1:e*k)=dibk(1:e*k);
   doall = repmat([do1 do2 do3 do4],tmax,1);
   diall = repmat([di1 di2 di3 di4],tmax,1);

56 % Calculating the volume of each element !
   V = Lall*pi.*((doall./2).^2−(diall./2).^2); % m3
   V(nn+1) = L*pi*(dv/2)^2;


   % Calculating the rho*cp for each element !
```

112

```
61  rc = zeros(tmax,all);
    rc(:,1:mm) = 8933*cu_cp(T(:,1:mm)); % J/m3.K
    rc(:,mm+1:nn) = por*wl_rho(T(:,mm+1:nn)).*wl_cp(T(:,mm+1:nn))+(1-por)*8933*cu_cp(T(:,mm+1:nn));
    rc(:,nn+1) = wv_rho(T(:,nn+1)).*wv_cp(T(:,nn+1));
    rc(:,zz+1:all) = 2702*al_cp(T(:,zz+1:all));
66
    % Calculating the axial Rz and radial resistance for each element !
    Rr = zeros(tmax,all+c); Rz = zeros(tmax,all+c);
    Rr(:,1:mm) = r_wall(diall(:,1:mm),doall(:,1:mm),Lalla(:,1:mm),T(:,1:mm)); % K/W
    Rr(:,mm+1:nn) = r_wick(diall(:,mm+1:nn),doall(:,mm+1:nn),Lalla(:,mm+1:nn),T(:,mm+1:nn),d,N);
71  Rr(:,zz+1:all)= r_block(diall(:,zz+1:all),doall(:,zz+1:all),Lalla(:,zz+1:all),T(:,zz+1:all));
    Rr(:,all+1:all+c) = r_conv(do,dconv,Lc/c,T(:,e+a+1:z),Tinf,flow);
    Rz(:,1:mm) = r_wall_ax(diall(:,1:mm),doall(:,1:mm),Lall(:,1:mm),T(:,1:mm));
    Rz(:,mm+1:nn) = r_wick_ax(diall(:,mm+1:nn),doall(:,mm+1:nn),Lall(:,mm+1:nn),T(:,mm+1:nn),d,N);
    Rz(:,nn+1) = r_vap(T(:,nn+1),Qe,dv,Av,Le,La,Lc);
76  Rz(:,zz+1:all)= r_block_ax(diall(:,zz+1:all),doall(:,zz+1:all),Lall(:,zz+1:all),T(:,zz+1:all));

    sTR(:,nn-z+1:nn) = T(:,nn-z+1:nn)./Rr(:,nn-z+1:nn);
    sR(:,nn-z+1:nn) = 1./Rr(:,nn-z+1:nn);
    sumTR(:,1) = sum(sTR(:,nn-z+1:nn-z+e),2);
81  sumR(:,1) = sum(sR(:,nn-z+1:nn-z+e),2);
    sumTR(:,2) = sum(sTR(:,nn-z+e+1:nn),2);
    sumR(:,2) = sum(sR(:,nn-z+e+1:nn),2);


    % Calculating the interface axial (Tza,Tzb) and radial (Trc,Trd) temp for each element !
86  Tza = zeros(tmax,all); Tzb = zeros(tmax,all); Trc = zeros(tmax,all); Trd = zeros(tmax,all);
    Tza(:,2:nn) = (T(:,1:nn-1)./Rz(:,1:nn-1)+T(:,2:nn)./Rz(:,2:nn))./(1./Rz(:,1:nn-1)+1./Rz(:,2:nn));
    Tzb(:,1:nn-1)=Tza(:,2:nn);
    ii = rem(i(1:nn),z);
    j=find(ii==1); Tza(:,j)=T(:,j);
91  j=find(ii==0); Tzb(:,j)=T(:,j);
    Tza(:,zz+2:all) = (T(:,zz+1:all-1)./Rz(:,zz+1:all-1)+T(:,zz+2:all)./Rz(:,zz+2:all))./(1./Rz(:,zz+1:all-1)+1./Rz(:,zz+2:all));
    Tzb(:,zz+1:all-1)=Tza(:,zz+2:all);
    ii = rem(i(zz+1:all)-zz,e);
    j=find(ii==1); Tza(:,j+zz)=T(:,j+zz);
96  j=find(ii==0); Tzb(:,j+zz)=T(:,j+zz);
    Trc(:,1:e) = (T(:,zz+1:zz+e)./Rr(:,zz+1:zz+e)+T(:,1:e)./Rr(:,1:e))./(1./Rr(:,zz+1:zz+e)+1./Rr(:,1:e));
    Trc(:,e+1:e+a) = T(:,e+1:e+a);
    Trc(:,e+a+1:z) = (T(:,e+a+1:z)./Rr(:,e+a+1:z)+Tinf./Rr(:,all+1:all+c)/2)./(1./Rr(:,e+a+1:z)+1./Rr(:,all+1:all+c)/2);
    Trc(:,z+1:nn) = (T(:,1:nn-z)./Rr(:,1:nn-z)+T(:,z+1:nn)./Rr(:,z+1:nn))./(1./Rr(:,1:nn-z)+1./Rr(:,z+1:nn));
101 Trd(:,1:nn-z) = Trc(:,z+1:nn);
    Tza(:,nn+1) = (sumTR(:,1)+T(:,nn+1)./Rz(:,nn+1))./(sumR(:,1)+1./Rz(:,nn+1));
    Tzb(:,nn+1) = (sumTR(:,2)+T(:,nn+1)./Rz(:,nn+1))./(sumR(:,2)+1./Rz(:,nn+1));
    Trd(:,nn-z+1:nn-z+e) = repmat(Tza(:,nn+1),1,e); Trd(:,nn-z+e+1:nn) = repmat(Tzb(:,nn+1),1,a+c);
    Trd(:,zz+1:zz+e) = Trc(:,1:e);
106 Trd(:,zz+e+1:all) = (T(:,zz+1:all-e)./Rr(:,zz+1:all-e)+T(:,zz+e+1:all)./Rr(:,zz+e+1:all))./(1./Rr(:,zz+1:all-e)+1./Rr(:,zz+e\
    (cont.)+1:all));
    Trc(:,zz+1:all-e) = Trd(:,zz+e+1:all);
    Trc(:,all-e+1:all) = (Q(:,1:e)./2+T(:,all-e+1:all)./Rr(:,all-e+1:all))./(1./Rr(:,all-e+1:all));


    time = toc
111
    name = ['w',num2str(Nw),'bsv6Q',num2str(max(Qe)),'C',num2str(Tinf-273,'%0.3d'),'e',num2str(e,'%0.2d'),'a',num2str(a,'\
    (cont.)%0.2d'),'c',num2str(c,'%0.2d'),'m',num2str(m,'%0.2d'),'n',num2str(n,'%0.2d'),'k',num2str(k,'%0.2d'),'mg',num2str(\
    (cont.)max(mg*1e8,0),'%3.0f'),'E08'];
    save (name)
```

113

Listing A.2: ODE File

```
% Equations for the ODE Solver.

function dT = eqns(t,T)

[e a c m n k z mm nn zz all Tinf flow mg Rg T0 L Le Lc La Leff do di db dconv Ap Ac Ae N Nw d tw dv Av Aw por K rcap] = in\
(cont.)(1);

i = [1:all]';

Qe = heat(t)';
Q = repmat(Qe/e,1,e);
Q = Q';

% Non-Condensable Gases Modelling Part !
if (mg > 0) Lcin = mg*Rg*Tinf./((w_psat(T(nn+1))-w_psat(Tinf))*Av);
else Lcin = 0.0*T(nn+1);
end
Lcac = min(Lc + La - Lcin,Lc + La);
j = find(Lcac < 0); Lcac(j) = 0.0;
sumL_a = [1:a]*La/a;
sumL_c = [1:c]*Lc/c + La;
ia1 = find(sumL_a <= Lcac); ia2 = find(sumL_a > Lcac);
ic1 = find(sumL_c <= Lcac); ic2 = find(sumL_c > Lcac);
Lca_a(ia1) = La/a; Lca_a(ia2) = La/a-(sumL_a(ia2)-Lcac);
Lca_c(ic1) = Lc/c; Lca_c(ic2) = Lc/c-(sumL_c(ic2)-Lcac);

% calculating the length (Lall) and active length (Lalla) for each element !
Lz1 = repmat([repmat(Le/e,1,e) repmat(La/a,1,a) repmat(Lc/c,1,c)],1,m+n);
Lz1a = repmat([repmat(Le/e,1,e) repmat(La/a,1,a) repmat(Lc/c,1,c)],1,m+n-1);
Lz1b = repmat(Le/e,1,e); Lz2=zeros(1,zz-nn); Lz3=repmat(repmat(Le/e,1,e),1,k);
Lall = [Lz1 Lz2 Lz3]'; Lalla = [Lz1a Lz1b Lca_a Lca_c Lz2 Lz3]';
j = find(Lalla < 0); Lalla(j) = 0.0;

% calculating the outer and inner diameters for each element !
dowa(1:z,1:m) = repmat(do-([1:m]-1).*(do-di)/m,z,1);
diwa(1:z,1:m) = repmat(do-[1:m].*(do-di)/m,z,1);
dowc(1:z,1:n) = repmat(di-([1:n]-1).*(di-dv)/n,z,1);
diwc(1:z,1:n) = repmat(di-[1:n].*(di-dv)/n,z,1);
dobk(1:e,1:k) = repmat(do+[1:k].*(db-do)/k,e,1);
dibk(1:e,1:k) = repmat(do+([1:k]-1).*(db-do)/k,e,1);
do1(1:mm)=dowa(1:mm); do2(1:z*n)=dowc(1:z*n);
do3=zeros(1,zz-nn); do4(1:e*k)=dobk(1:e*k);
di1(1:mm)=diwa(1:mm); di2(1:z*n)=diwc(1:z*n);
di3=zeros(1,zz-nn); di4(1:e*k)=dibk(1:e*k);
doall = [do1 do2 do3 do4]';
diall = [di1 di2 di3 di4]';

% Calculating the volume of each element !
V = Lall*pi.*((doall./2).^2-(diall./2).^2); % m3
V(nn+1) = L*pi*(dv/2)^2;

% Calculating the rho*cp for each element !
rc = zeros(all,1);
rc(1:mm) = 8933*cu_cp(T(1:mm)); % J/m3.K
rc(mm+1:nn) = por*wl_rho(T(mm+1:nn)).*wl_cp(T(mm+1:nn))+(1-por)*8933*cu_cp(T(mm+1:nn));
rc(nn+1) = wv_rho(T(nn+1))*wv_cp(T(nn+1));
rc(zz+1:all) = 2702*al_cp(T(zz+1:all));

% Calculating "2/(rho*cp*V)" for each element !
al = 2./rc./V;
```

```
   % Calculating the axial Rz and radial resistance for each element !
62 Rr = zeros(all+c,1); Rz = zeros(all+c,1);
   Rr(1:mm) = r_wall(diall(1:mm),doall(1:mm),Lalla(1:mm),T(1:mm)); % K/W
   Rr(mm+1:nn) = r_wick(diall(mm+1:nn),doall(mm+1:nn),Lalla(mm+1:nn),T(mm+1:nn),d,N);
   Rr(zz+1:all)= r_block(diall(zz+1:all),doall(zz+1:all),Lalla(zz+1:all),T(zz+1:all));
   Rr(all+1:all+c) = r_conv(do,dconv,Lc/c,T(e+a+1:z),Tinf,flow);
67 Rz(1:mm) = r_wall_ax(diall(1:mm),doall(1:mm),Lall(1:mm),T(1:mm));
   Rz(mm+1:nn) = r_wick_ax(diall(mm+1:nn),doall(mm+1:nn),Lall(mm+1:nn),T(mm+1:nn),d,N);
   Rz(nn+1) = r_vap(T(nn+1),Qe,dv,Av,Le,La,Lc);
   Rz(zz+1:all)= r_block_ax(diall(zz+1:all),doall(zz+1:all),Lall(zz+1:all),T(zz+1:all));

72 sTR(nn-z+1:nn) = T(nn-z+1:nn)./Rr(nn-z+1:nn);
   sR(nn-z+1:nn) = 1./Rr(nn-z+1:nn);
   sumTR(1) = sum(sTR(nn-z+1:nn-z+e));
   sumR(1) = sum(sR(nn-z+1:nn-z+e));
   sumTR(2) = sum(sTR(nn-z+e+1:nn));
77 sumR(2) = sum(sR(nn-z+e+1:nn));

   % Calculating the interface axial (Tza,Tzb) and radial (Trc,Trd) temp for each element !
   Tza = zeros(all,1); Tzb = zeros(all,1); Trc = zeros(all,1); Trd = zeros(all,1);
   Tza(2:nn) = (T(1:nn-1)./Rz(1:nn-1)+T(2:nn)./Rz(2:nn))./(1./Rz(1:nn-1)+1./Rz(2:nn));
82 Tzb(1:nn-1)=Tza(2:nn);
   ii = rem(i(1:nn),z);
   j=find(ii==1); Tza(j)=T(j);
   j=find(ii==0); Tzb(j)=T(j);
   Tza(zz+2:all) = (T(zz+1:all-1)./Rz(zz+1:all-1)+T(zz+2:all)./Rz(zz+2:all))./(1./Rz(zz+1:all-1)+1./Rz(zz+2:all));
87 Tzb(zz+1:all-1)=Tza(zz+2:all);
   ii = rem(i(zz+1:all)-zz,e);
   j=find(ii==1); Tza(j+zz)=T(j+zz);
   j=find(ii==0); Tzb(j+zz)=T(j+zz);
   Trc(1:e) = (T(zz+1:zz+e)./Rr(zz+1:zz+e)+T(1:e)./Rr(1:e))./(1./Rr(zz+1:zz+e)+1./Rr(1:e));
92 Trc(e+1:e+a) = T(e+1:e+a);
   Trc(e+a+1:z) = (T(e+a+1:z)./Rr(e+a+1:z)+Tinf./Rr(all+1:all+c)/2)./(1./Rr(e+a+1:z)+1./Rr(all+1:all+c)/2);
   Trc(z+1:nn) = (T(1:nn-z)./Rr(1:nn-z)+T(z+1:nn)./Rr(z+1:nn))./(1./Rr(1:nn-z)+1./Rr(z+1:nn));
   Trd(1:nn-z) = Trc(z+1:nn);
   Tza(nn+1) = (sumTR(1)+T(nn+1)/Rz(nn+1))/(sumR(1)+1/Rz(nn+1));
97 Tzb(nn+1) = (sumTR(2)+T(nn+1)/Rz(nn+1))/(sumR(2)+1/Rz(nn+1));
   Trd(nn-z+1:nn-z+e) = Tza(nn+1); Trd(nn-z+e+1:nn) = Tzb(nn+1);
   Trd(zz+1:zz+e) = Trc(1:e);
   Trd(zz+e+1:all) = (T(zz+1:all-e)./Rz(zz+1:all-e)+T(zz+e+1:all)./Rr(zz+e+1:all))./(1./Rr(zz+1:all-e)+1./Rr(zz+e+1:all));
   Trc(zz+1:all-e) = Trd(zz+e+1:all);
102 Trc(all-e+1:all) = (Q(1:e)./2+T(all-e+1:all)./Rr(all-e+1:all))./(1./Rr(all-e+1:all));

   dT = zeros(all,1); % a column vector

   dT(1:nn)=al(1:nn).*((Tza(1:nn)+Tzb(1:nn)-2*T(1:nn))./Rz(1:nn)+(Trc(1:nn)+Trd(1:nn)-2*T(1:nn))./Rr(1:nn));
107 dT(nn+1)=al(nn+1).*((Tza(nn+1)+Tzb(nn+1)-2*T(nn+1))./Rz(nn+1));
   dT(zz+1:all)=al(zz+1:all).*((Tza(zz+1:all)+Tzb(zz+1:all)-2*T(zz+1:all))./Rz(zz+1:all)+(Trc(zz+1:all)+Trd(zz+1:all)-2*T(zz
   (cont.)+1:all))./Rr(zz+1:all));
```

Listing A.3: Input File

```
%All Input Parameters

function [e a c m n k z mm nn zz all Tinf flow mg Rg T0 L Le Lc La Leff do di db dconv Ap Ac Ae N Nw d tw dv Av Aw por K \
(cont.)rcap] = in(t)


% Define number of nodes for each part
e = 24; %number of part of evaporator
a = 24; %number of part of adiabatic
c = 36; %number of part of condenser
m = 1; %number of radial layers in pipe wall
n = 1; %number of radial layers in wick structure
k = 4; %number of radial layers in evaporator block

z = e+a+c; %total number of parts for one row
mm = m*z; %total number of parts for the pipe wall
nn = mm+n*z; %total number of parts for wall and wick
zz = nn+1; %total number of parts for wall, wick, vapour
all = zz+k*e; %total number of parts for all heat pipe and evaporator block


% Define the boundary conditions and amount of non-condensables
Tinf = 273 + 20; % K
flow = 5; % water flow rate (litres per minute)
mg = 3.5e-07; % mass of Non-Condensible Gas, kg
Rg = 287; % Gas Constant for air, J/kgK


% Define the intial conditions
T0(1:all)=Tinf;

% Heat Pipe Geometries
L =(14)*0.0254; %Overall Length, m
Le=(4)*0.0254; %Evaporator Length, m
Lc=(6)*0.0254; %Condenser Length, m
La=L-Le-Lc; %Adiabatic Length, m
Leff=Le/2 + La + Lc/2; %Effective Length, m
do=(3/4)*0.0254; %Outer diameter, m
di=(0.62)*0.0254; %Inner diameter, m
db=(3.5)*0.0254; %Block diameter, m
dconv=1*0.0254; %Convective Water Jacket diameter, m
Ap=pi*(do/2)^2; %End cross-sectional area of whole pipe, m^2
Ac=pi*do*Lc; %Condenser area, m^2
Ae=pi*do*Le; %Evaporator area, m^2


% Mesh Parameters
N=100/0.0254; %Mesh Number, 1/m
Nw=3; %Number of wraps
d=(0.0043)*0.0254; %Wire diameter, m
tw=2*d*Nw; %Thickness of wick, m. Assumes a spacing of d between wall and first layer and a spacing of d between each layer.

dv=di-2*tw; %Diameter of vapour core, m
Av=pi*(dv/2)^2; %Cross-sectional area of vapour coure, m^2
Aw=pi*((di/2)^2-(dv/2)^2); %Cross-sectional area of wick, m^2

por=1-pi*1.05*N*d/4; %Porosity
K=d^2*por^3/(122*(1-por)^2); %Permiability, m^2
rcap=1/(2*N); %Effrective Capillary radius, m
```

116

Listing A.4: Heat File

```
1   %Pass time, Returns Heat Input function in time, W

    function z=heat(t)

    tmax= max(size(t));
6
    % Steady State Test
    tn = [0:300:15000];
    Q = [20:20:1600];
    z(1:tmax) = zeros;
11  tnx=max(size(tn));
    for i = 1:tnx−1
        indices = find(tn(i) < t & t <= tn(i+1));
        z(indices) = Q(i);
    end
16
    % % Step Input
    % t1 = 0;
    % t2 = 3000;
    % Q = 100;
21  % z(1:tmax) = zeros;
    % indices = find(t1 < t & t <= t2);
    % z(indices) = Q;

    % % Square Wave Input
26  % period = 2000;
    % amp = 100;
    % duty = 50; % bet. 0 − 100
    % z(1:tmax) = square(2*pi*t(1:tmax)/period,duty)*amp/2+amp/2;

31  % % Sawtooth Wave Input (Triangular)
    % period = 2000;
    % amp = 100;
    % width = 1.0; % bet. 0 − 1
    % z(1:tmax) = sawtooth(2*pi*t(1:tmax)/period,width)*amp/2+amp/2;
36
    % % Sinsoidal Wave Input
    % period = 2000;
    % amp = 100;
    % z(1:tmax) = sin(2*pi*(t(1:tmax)−period/4)/period)*amp/2+amp/2;
```

117